

Evaluating the Top-down Emission Rate Retrieval Algorithm
(TERRA) using Virtual Aircraft-based Sampling within the
GEM-MACH Model

SEPEHR FATHI

A THESIS SUBMITTED TO
THE FACULTY OF GRADUATE STUDIES
IN PARTIAL FULFILLMENT OF THE REQUIREMENTS
FOR THE DEGREE OF

MASTER OF SCIENCE

GRADUATE PROGRAM IN PHYSICS AND ASTRONOMY
YORK UNIVERSITY
TORONTO, ONTARIO

December 2017

© Sepehr Fathi, 2017

Abstract

Between August 13th and September 7th of 2013, aircraft-based measurements of air pollutants were collected in support of the Joint Canada-Alberta implementation plan for Oil Sands Monitoring (JOSM). The Top-down Emission Rate Retrieval Algorithm (TERRA) was developed by Environment and Climate Change Canada (ECCC) to estimate facility emission rates based on the aircraft measurements. Here, as part of a larger effort on TERRA improvement, ECCC's air quality model, Global Environmental Multiscale - Modelling Air-quality And CHemistry (GEM-MACH), was used as a surrogate source of concentration and meteorology data. The TERRA-calculated emission rates are compared with those input into GEM-MACH, for different TERRA configurations. This work evaluates the combination of TERRA and GEM-MACH as a proxy for testing the downward extrapolation schemes within TERRA and identifies possible avenues for GEM-MACH and/or TERRA improvements. Outcomes from this work can provide useful suggestions for future flight plans for top-down emission rate estimations.

Dedication

It is to my parents, Fariba and Masoud, who were my initial teachers that I dedicate this thesis.

Acknowledgments

I would first like to thank my thesis advisor Dr. Mark Gordon of the Earth & Space Science Department at York University, for providing me with the opportunity to work on a fascinating research project. The door to Prof. Gordon's office was always open whenever I ran into a trouble spot or had a question about my research or putting my ideas on paper. He consistently allowed this paper to be my own work, but steered me in the right direction whenever he thought I needed it.

I would also like to thank the experts from the Air Quality Research Dept., Environment and Climate Change Canada who were involved in this research project: Paul Makar, Ayodeji Akingunola, Junhua Zhang and Shao-Meng Li. Without their passionate collaboration and input, this project would have been impossible.

Thanks to Stefan Miller and Timothy Jiang for their support and friendship in the Air-Quality lab, York University.

Finally, I must express my very profound gratitude to my parents for providing me with unfailing support and continuous encouragement throughout my years of study and through the process of researching and writing this thesis. This accomplishment would not have been possible without them. Thank you.

Contents

Abstract	ii
Dedication	iii
Acknowledgments	iv
List of Tables	x
List of Figures	xxvi
List of Abbreviations	xxvii
1 Introduction	1
1.1 Related Work	3
1.2 TERRA	5
1.2.1 Emissions Algorithm	5
1.2.2 Near Surface Extrapolations	7
1.3 GEM-MACH Model	9
1.4 Investigating Emissions Estimates Using GEM-MACH With TERRA	10
2 Methods	15
2.1 Two Study Cases: Flights 8 and 18	15
2.2 Flying Within The Model	18
2.2.1 Along The Flight Tracks (AFT)	19
2.2.2 Vertical Profiles (VP)	21
2.3 Pressure, Wind and Air density profiles	26
2.3.1 Logarithmic Pressure Profiles	26
2.3.2 Temperature, Water Vapor Mixing Ratio and Air density	27

2.3.3	Easterly and Northerly Wind Screens	28
2.4	Surface Concentrations and Deposition	29
2.5	Utilizing TERRA	29
3	Implementation and Results	33
3.1	Estimated Emission Rates: AFT Method	33
3.1.1	Air Density	33
3.1.2	Wind	36
3.1.3	Air Flux	36
3.1.4	Compound Mixing Ratio	38
3.1.5	Advective Fluxes	38
3.1.6	Surface Deposition	40
3.1.7	Emissions	41
3.2	Estimated Emission Rates: VP Method	42
3.2.1	Air Density, Wind and Air Flux	43
3.2.2	Compound Mixing Ratio, Surface Deposition and Emission Rates	47
4	Discussions	65
4.1	Sub-flight-level Gaussian Interpolation (SGI)	65
4.2	AFT Krigged Screen and Surface Layer Extrapolation	69
4.3	Mass Balance Technique and Temporal Evolution of The System	75
4.4	Shift In Plume Location Relative to Aircraft's Motion	86
4.5	VP Method Overestimations	92
5	Conclusions	93
	Bibliography	97

List of Tables

2.1	Emissions inventory by Canadian Natural Resources Ltd., input in GEM-MACH for 20 August 2013 forecast (Flight 8) [6].	17
2.2	Emissions inventory by Syncrude Canada Ltd., input in GEM-MACH for 3 September 2013 forecast (Flight 18) [6].	17
3.1	Extracted meteorological and concentration profiles along the flight 8 tracks on 20 August 2013, were used to estimate SO ₂ emission rates. Four different extrapolation methods, for heights below the lowest flight level to the surface, were examined. . .	42
3.2	Extracted meteorological and concentration profiles along the flight 8 tracks on 20 August 2013, were used to estimate CO emission rates. Four different extrapolation methods, for heights below the lowest flight level to the surface, were examined. . .	42
3.3	Extracted meteorological and concentration profiles along the flight 18 tracks on 3 September 2013, were used to estimate SO ₂ emission rates. Four different extrapolation methods, for heights below the lowest flight level to the surface, were examined.	43
3.4	Extracted meteorological and concentration profiles along the flight 18 tracks on 3 September 2013, were used to estimate CO emission rates. Four different extrapolation methods, for heights below the lowest flight level to the surface, were examined.	43

3.5	Advective air fluxes through the lateral sides and the top of the box and the rate of air densification, were estimated for periods of ~ 10 min during flight 8. Estimations were made based on the vertical profiles extracted from the GEM-MACH model (section 2.2.2). The average net air flux through the lateral walls is into the box (negative) and the average net vertical flux is out of the box (positive).	47
3.6	Advective air fluxes through the lateral sides and the top of the box and the rate of air densification, were estimated for periods of ~ 15 min during flight 18. Estimations were made based on the vertical profiles extracted from the GEM-MACH model (section 2.2.2). The net air flux through the lateral sides remains positive (out of the box) but decreases, over time. The average net air flux through the lateral walls is positive and the average net vertical flux is negative.	52
3.7	SO ₂ emission rates were derived based on the vertical profiles extracted form the GEM-MACH model for flight 8, as described in section 2.2.2. Emission rates were estimated for periods of ~ 10 min.	61
3.8	CO emission rates were derived based on the vertical profiles extracted form the GEM-MACH model for flight 8, as described in section 2.2.2. Emission rates were estimated for periods of ~ 10 min.	62
3.9	SO ₂ emission rates were derived based on the vertical profiles extracted form the GEM-MACH model for flight 18, as described in section 2.2.2. Emission rates were estimated for periods of ~ 15 min.	63

3.10	CO emission rates were derived based on the vertical profiles extracted from the GEM-MACH model for flight 18, as described in section 2.2.2. Emission rates were estimated for periods of ~ 15 min.	63
3.11	Comparing the estimated emissions of SO ₂ and CO by Canadian Natural Resources Ltd. (CNRL) during flight 8 with the GEM-MACH model emissions inputs. Both Along The Flight Tracks (AFT) and Vertical Profiles (VP) methods overestimate the emissions. Only AFT Constant and Linear fit methods are compared here, as they have shown the best performance out of the five TERRA extrapolation methods. Percentage differences from the model inputs are shown for each method. . . .	64
3.12	Comparing the estimated emissions of SO ₂ and CO by Syn-crude during flight 18 with the GEM-MACH model emissions inputs. Both AFT and VP methods overestimate the emissions. Only AFT Constant and Linear fit methods are compared here, as they have shown the best performance out of the five TERRA extrapolation methods. Percentage differences from the model inputs are shown for each method. . . .	64
4.1	Comparing average SO ₂ and CO mixing ratios on AFT krigged screens extrapolated below the lowest flight level (Constant and Linear fit methods) to mean VP for each case. \uparrow indicates overestimation relative to mean VP.	73

4.2	Potential improvements in mean estimated emissions for each extra hour of flight time. Percentage improvements relative to model emissions inventory for flight 8 SO ₂ and CO and flight 18 CO emissions are shown. For flight 18 SO ₂ the result is negative, meaning that the estimates continue to deviate from the model emissions inventory and therefore no improvements are made by extending the flight time for this case.	84
4.3	Mean estimated emissions for the second hour of flights 8 and 18 are compared to model emissions inventory. Percentage differences show the estimated emissions during the second half of the flights agree better with inventory values. Flight 18 SO ₂ emissions for this period deviate more from model emissions and are not shown here.	84
4.4	Dependence of estimated emission rates on overestimation in SO ₂ concentrations for flight 8 VP method estimations, was examined. Results show that the changes are one to one, N % increase in total SO ₂ concentration results in almost N % increase in estimated emission rates.	87

List of Figures

1.1	Flight 8 SO ₂ concentration screens generated based on data extracted from GEM-MACH, extrapolated below the lowest flight level. Flight tracks superimposed on the screen (black dots). Four TERRA extrapolation methods, Zero to Constant, Constant, Linear fit and Exponential fit are shown.	9
1.2	GEM-MACH15 grid is a sub-grid of GEM15 with co-located grid points , covering North America [8].	11
1.3	Three-level nested grid of GEM-MACH used in ECCC Oil Sands simulations [18]. SO ₂ concentrations are plotted here. .	12
2.1	Flight paths from the Fort McMurray Airport to and around oil sands facilities CNRL and Syncrude on August 20 and September 3 of 2013 respectively. These two flight tracks were used to extract data from the GEM-MACH model for emissions estimation with TERRA.	16

2.2 A Box flight is realized by flying an aircraft in a rectangular path at several consecutive levels around a region of interest. In this illustration, such a box flight is shown around the CNRL facility during the flight 8. The flight tracks are shown with black circles, at 1 Hz. Also, the turning points along the aircraft’s horizontal path are marked with gray squares on the map of the region. A schematic representation of a plume from a stack within the facility is shown. The plume is incident on the eastern side of the box, were it is registered by the aircraft along the flight tracks. 18

2.3 The same box flight as in Figure 2.2. In this illustration cell structure of the GEM-MACH model is also shown in white grid lines. The grid squares are spanned by 2.5 km horizontally on each side and to the scale. The vertical grid spacing is not to the scale and is actually not monotonic in size as it is depicted here, but it increases progressively from 35 m high for the cells near the ground surface to about 200 m at the top of the ”box” at a height of about 1450 m above ground level (agl), highest flight level during flight 8. The flight tracks, represented by black circles, are overlaid with the model grid. The hypothetical aircraft (in red), travels through the model cells along the box flight path and extracts meteorological data and species (e.g. SO₂, CO) concentrations from each cell, mimicking aircraft-based measurements. The extracted data from the model cells (spaced 2.5 km horizontally) are then interpolated in time and space, down to 100 m spacing between each two point, to match the frequency of the aircraft measurements during the field campaign (every second). 19

2.4	The region of the CRNL facility, flight 8 tracks (black circles) and GEM-MACH model grid spacing (white) are illustrated. The model cell, highlighted in red, is representing aircraft's (also red) state parameters along the flight tracks within the model. The highlighted model cell is the sampling volume. Extracting meteorology and concentration data from each individual cell along the flight tracks, simulates aircraft-based measurements. The species concentration corresponding to the portion of the plume engulfed by the cell, adds to the overall concentration within the sampling cell volume.	22
2.5	Four steps of generating an SO ₂ concentration screen from the model extracted values along the flight tracks of flight 8, on 20 August 2013 around the CNRL facility. Flight 8 tracks are superimposed with black dots and the box lateral walls are labeled with geographical directions East, North, West and South.	23
2.6	The region of the CRNL facility, flight 8 tracks (black circles) and GEM-MACH model grid spacing (white) are illustrated. The sampling volume is highlighted as a red column, comprised of several model cells stacked on top of each other, with the same longitude and latitude as the aircraft (red) along the flight path. This column sweeps all the lateral sides of the Box as the aircraft travels around the facility at each level. Extracting meteorology and concentration data from this sampling volume, provides enough data to generate a screen for every flight level.	24

2.7	SO ₂ concentration screen, generated for the first 10 min of the flight 8; In two steps: 1) extracting vertical profiles and interpolating vertically between points and 2) Interpolating horizontally between the vertical profiles and filling the screen. The location and direction (to the left) of the aircraft along the first flight track is shown with white triangles. The green and red triangles mark the start and end point at this level. In this case, vertical profiles extracted along the flight track at the lowest level, were used to construct a screen for the first 10 min of flight 8.	25
2.8	Air pressure screen constructed for flight 8, using recorded values at the “AB FORT MCMURRAY A ALBERTA” weather station , at the elevation of $z = 369.10$ m [10], and utilizing Equation 2.1 [24]. Note the difference in surface topography for (a) and (b).	27
2.9	SO ₂ deposition rates estimated based on surface concentrations extracted from GEM-MACH model for each flight.	30
3.1	Pressure, temperature, water vapor mixing ratio and air density screens were constructed for 20 August 2013 around the CNRL facility, based on extracted values along the flight tracks (AFT) during flight 8 and profiles described by Equations 2.1 and 2.2. Flight 8 tracks are superimposed with black dots and the box lateral walls are labeled with geographical directions East, North, West and South.	34

3.2	Pressure, temperature, water vapor mixing ratio and air density screens were constructed for 3 September 2013 around the Syncrude facility, based on extracted values along the flight tracks (AFT) during flight 18 and profiles described by Equations 2.1 and 2.2. Flight 18 tracks are superimposed with black dots.	35
3.3	Screens constructed based on the AFT extracted air density values. Flights 8 and 18 tracks are superimposed with black dots and the box lateral walls are labeled with geographical directions East, North, West and South.	35
3.4	Easterly and northerly wind speed screens were created based on wind vectors extracted along the flight tracks (AFT) for flight 8 on August 20 2013. Flight 8 tracks are superimposed with black dots and the box lateral walls are labeled with geographical directions East, North, West and South.	36
3.5	Easterly and northerly wind speed screens were created based on wind vectors extracted along the flight tracks (AFT) for flight 18 on 3 September 2013. Flight 18 tracks are superimposed with black dots.	37

3.6 Horizontal advective air flux $E_{air,H}$ screen (positive out of the box), generated based on air density and wind speed screens. Flights 8 (a) and 18 (b) tracks are superimposed with black dots and the box lateral walls are labeled with geographical directions East, North, West and South. (a) the main air flux enters the box from the West wall and exits from the East wall. Therefore, the East wall is where the apparent plume on the screen from the emission source within the box, is expected to be found. (b) the main air flux enters the box from the west and south walls and exits from the east and north wall. East and north walls are where the apparent plume is expected to be found. 38

3.7 Mixing ratio screens constructed based on measurements along the flight 8 tracks on August 20 2013, extrapolated below the lowest flight level (extrapolations using the Linear fit method are shown as examples). Flight 8 tracks are superimposed with black dots and the box lateral walls are labeled with geographical directions East, North, West and South. In both cases the plume appears on the East wall. 39

3.8 Mixing ratio screens constructed based on measurements along the flight 18 tracks on 3 September 2013, extrapolated below the lowest flight level (extrapolations using the Linear fit method are shown as examples). Flight 18 tracks are superimposed with black dots and the box lateral walls are labeled with geographical directions East, North, West and South. In both cases the plume appears on the North wall. 39

3.9	Compound horizontal advective mass flux through lateral walls of the box. Screens were constructed based on compound mixing ratio measurements along the flight 8 tracks on 20 August 2013 and the estimated horizontal advective air flux. Flight 8 tracks are superimposed with black dots and the box lateral walls are labeled with geographical directions East, North, West and South.	40
3.10	Compound horizontal advective mass flux through lateral walls of the box. Screens were constructed based on compound mixing ratio measurements along the flight 18 tracks on 3 September 2013 and the estimated horizontal advective air flux. Flight 18 tracks are superimposed with black dots.	41
3.11	Four of the twelve horizontal advective air flux screens, generated for flight 8. The location and direction (to the left) of the aircraft along the flight tracks is shown with white triangles. The green triangle marks the starting point at each level. The path terminates at the red triangle. At each level, the aircraft travels around the facility, from the green triangle to the red, in about 10 min. Vertical profiles extracted along the flight track, were used to construct screens for each 10 min. Therefore, the temporal evolution of the system can be studied. Note how the horizontal advective air flux is changing with time (more visible on East and West walls).	45

3.12 Four of the eight horizontal advective air flux screens, generated for flight 18. The location and direction (to the right) of the aircraft along the flight tracks is shown with white triangles. The green triangle marks the starting point at each level. The path terminates at the red triangle. At each level, the aircraft travels around the facility, from the green triangle to the red, in about 15 min. Vertical profiles extracted along the flight track, comprise screens for each 15 min. Therefore, the temporal evolution of the system can be studied. 46

3.13 Four of the twelve SO₂ concentration screens, generated for flight 8. The location and direction (to the left) of the aircraft along the flight tracks is shown with white triangles. The green triangle marks the starting point at each level. The path terminates at the red triangle. At each level, the aircraft travels around the facility, from the green triangle to the red, in about 10 min. Vertical profiles extracted along the flight track, were used to construct screens for each 10 min. Therefore, the temporal evolution of the system can be studied, a rising and diluting plume center in this case. 48

- 3.14 Four of the twelve CO concentration screens, generated for flight 8. The location and direction (to the left) of the aircraft along the flight tracks is shown with white triangles. The green triangle marks the starting point at each level. The path terminates at the red triangle. At each level, the aircraft travels around the facility, from the green triangle to the red, in about 10 min. Vertical profiles extracted along the flight track, were used to construct screens for each 10 min. Therefore, the temporal evolution of the system can be studied, a rising and diluting plume center in this case. Note the weak plume developing on the South wall near the surface. A change in background levels of CO can also be seen. 49
- 3.15 Four of the eight SO₂ concentration screens, generated for flight 18. The location and direction (to the right) of the aircraft along the flight tracks is shown with white triangles. The green triangle marks the starting point at each level. The path terminates at the red triangle. At each level, the aircraft travels around the facility, from the green triangle to the red, in about 15 min. Vertical profiles extracted along the flight track, comprise screens for each 15 min. Therefore, the temporal evolution of the system can be studied. 50
- 3.16 Four of the eight CO concentration screens, generated for flight 18. The location and direction (to the right) of the aircraft along the flight tracks is shown with white triangles. The green triangle marks the starting point at each level. The path terminates at the red triangle. At each level, the aircraft travels around the facility, from the green triangle to the red, in about 15 min. Vertical profiles extracted along the flight track, comprise screens for each 15 min. Temporal variation in CO levels can be seen from the figure. 51

- 3.17 Four of the twelve SO₂ advective horizontal flux screens, generated for flight 8. The location and direction (to the left) of the aircraft along the flight tracks is shown with white triangles. The green triangle marks the starting point at each level. The path terminates at the red triangle. At each level, the aircraft travels around the facility, from the green triangle to the red, in about 10 min. The temporal evolution of the SO₂ flux can be seen from the figure, in this case the total flux is decreasing with time. 53
- 3.18 Four of the twelve CO advective horizontal flux screens, generated for flight 8. The location and direction (to the left) of the aircraft along the flight tracks is shown with white triangles. The green triangle marks the starting point at each level. The path terminates at the red triangle. At each level, the aircraft travels around the facility, from the green triangle to the red, in about 10 min. The temporal evolution of the CO flux can be seen from the figure, in this case fluxes through the East and West walls are decreasing with time, at different rates. . . . 54
- 3.19 Four of the eight SO₂ advective horizontal flux screens, generated for flight 18. The location and direction (to the right) of the aircraft along the flight tracks is shown with white triangles. The green triangle marks the starting point at each level. The path terminates at the red triangle. At each level, the aircraft travels around the facility, from the green triangle to the red, in about 15 min. 55

3.20 Four of the eight CO advective horizontal flux screens, generated for flight 18. The location and direction (to the right) of the aircraft along the flight tracks is shown with white triangles. The green triangle marks the starting point at each level. The path terminates at the red triangle. At each level, the aircraft travels around the facility, from the green triangle to the red, in about 15 min. 56

3.21 SO₂ emissions by sources within CNRL on 20 August 2013 (Flight 8) were estimated based on model extracted values in two different approaches: 1) AFT (section 2.2.1) estimation over ~2 hours and 2) VP (section 2.2.2) estimations over periods of ~ 10 min. The first approach requires extrapolations below the lowest flight level for SO₂ mixing ratio screens. Different extrapolation methods resulted in different estimates. Four of these methods are compared to each other (dashed lines). Emissions retrieved for each ~10 minute with VP method (no extrapolation needed) are also plotted for comparison. Note how emission rates fluctuate and decrease with time. Model emission inventory is also plotted for comparison. 57

3.22 CO emissions by sources within CNRL on 20 August 2013 (Flight 8) were estimated based on model extracted values in two different approaches: 1) AFT (section 2.2.1) estimation over ~ 2 hours and 2) VP (section 2.2.2) estimations over periods of ~ 10 min. The first approach requires extrapolations below the lowest flight level for CO mixing ratio screens. Different extrapolation methods resulted in different estimates. Four of these methods are compared to each other (dashed lines). Emissions retrieved for each ~ 10 minute with VP method (no extrapolation needed) are also plotted for comparison. Note how emission rates fluctuate and decrease with time. Model emission inventory is also plotted with lines and markers. 58

3.23 SO₂ emissions by sources within Syncrude on 3 September 2013 (during flight 18) were estimated based on model extracted values in two different approaches: 1) AFT (section 2.2.1) estimation over ~ 2 hours and 2) VP (section 2.2.2) estimation over ~ 15 min. The first approach requires extrapolations below the lowest flight level for SO₂ mixing ratio screens. Different extrapolation methods resulted in different estimates. Four of these methods are compared to each other (dashed lines). Emissions retrieved for each ~ 15 minute with VP method (no extrapolation needed) are also plotted for comparison. Note how emission rates fluctuate and increase by time. SO₂ model emission inventory is also plotted for this flight. 59

3.24 CO emissions by sources within Syncrude on 3 September 2013 (during flight 18) were estimated based on model extracted values in two different approaches: 1) AFT (section 2.2.1) estimation over ~ 2 hours and 2) VP (section 2.2.2) estimation over ~ 15 min. The first approach requires extrapolations below the lowest flight level for CO mixing ratio screens. Different extrapolation methods resulted in different estimates. Four of these methods are compared to each other (dashed lines). Emissions retrieved for each ~ 15 minute with VP method (no extrapolation needed) are also plotted for comparison. Note how emission rates fluctuate and increase by time. CO model emission inventory is plotted for comparison. 60

4.1 Flight 18 SO₂ centerlines at $s = 27.2$ km for different screens are compared. z on the vertical axis is height above mean sea level (amsl). Dashed green and red lines are vertical profiles at s during the 5th and 6th 15 min of the flight. Black circles are the AFT extracted data points and the dashed black line is the vertical profile reconstructed from the extracted data points by kriging interpolation. The cyan line (with arrows) represents 2D linear interpolation instead of kriging. Compared to the mean vertical distribution for these heights and the time period between flight at levels 3 and 4 (blue), the linear interpolation shows a better performance. 68

4.2 Comparing the AFT (a) and VP (b) screens shows that kriging misplaces the plume maximum. Sub-flight-level Gaussian Interpolation (SGI) correction improves the estimation (c). . . 69

4.3	Sub-flight-level Gaussian Interpolation (SGI): AFT and VP centerlines of the plume shown in Figure 4.2 are compared here. z on the vertical axis is height above mean sea level (amsl). Looking at the green vertical profile, the peak is located between levels 5 and 6. Kriging misplaces the maximum on the 6th level. SGI correction places the maximum at the right height and improves the estimation.	70
4.4	Flight 8 SO ₂ centerlines at $s = 5680$ m are compared. z on the vertical axis is height above mean sea level (amsl). The black line shows the krigged vertical profile with no values below the lowest flight level. Blue and green dashed lines show the extrapolated values below the lowest flight with Constant and Linear fit methods, respectively. The level 0 vertical profile extracted from the model is plotted as a reference profile. Level 11(highest) VP is also plotted for comparison.	72
4.5	Flight 18 SO ₂ and CO centerlines at $s = 27240$ m are compared to mean vertical profiles (cyan). z on the vertical axis is height above mean sea level (amsl). For each case, extrapolated profiles below the lowest flight level are shown with green and red dashed lines for Linear fit and Constant methods respectively. The agreement between the krigged profile (black line) and the mean VP for SO ₂ is better than CO, and the Constant method shows a better performance compared to the Linear fit. . . .	74
4.6	Advective air fluxes estimated based on VP extracted model data during flight 8. (a) Horizontal air flux ($E_{air,H}$) entering (red) and leaving (blue) through the lateral sides of the box. Horizontal fluxes decrease over time. (b) Vertical air flux ($E_{air,v}$) leaving through the top of the box. Air is horizontally entering the box through the lateral walls and vertically leaving through the top (Convergence).	77

4.7	<p>Advective air fluxes estimated based on VP extracted model data during flight 18. (a) Horizontal air flux ($E_{air,H}$) entering (red) and leaving (blue) through the lateral sides of the box. Horizontal fluxes increase over time. (b) Vertical air flux ($E_{air,V}$) entering (negative) through the top of the box. Air is entering the box vertically through the top and leaving horizontally through the lateral walls (divergence).</p>	78
4.8	<p>Temporal change in average SO₂ concentrations on the screen during flight 8. The outgoing horizontal advective air flux ($E_{air,H}$) is also plotted. Both the concentration and the air flux decrease over time. Consequently, estimated SO₂ emissions also decrease over time.</p>	79
4.9	<p>Wind direction screen, generated using the VP extracted model data during the 9th 10 min segment of flight 8. (a) The screen is distorted, since the model was updated into a new state while the data was being collected for screen generation. (b) Horizontal profiles of wind direction along the box walls at $z = 600$ m are shown for the 8th, 9th and 10th 10 min segments of the flight. The profile during the 9th 10 min segment is partially in the previous state (during the 8th 10 min) and partially in the next state (during the 10th 10 min). This resulted in a distorted wind direction screen and unbalanced air flux estimations.</p>	82
4.10	<p>Flight 8 estimated emissions (blue) follow a decreasing trend. Linear fits (red) of the estimated emissions, projected forward for the next two hours after the flight time reach the model emissions inventory (green) and continue decreasing.</p>	83

4.11	Estimated emissions for the second half (first hour of flight not shown here) of flights 8 and 18 are compared to model emissions inventory (a) flight 8 SO ₂ emissions (b) flight 8 CO emissions (estimation for the 9th 10 min segment is removed) and (c) flight 18 CO emissions. Estimated emissions during the second hour of the 2 hr flights agree better with inventory values. This was not true for flight 18 SO ₂ emissions, which are not shown here.	85
4.12	The SO ₂ screen (east wall only) for flight 8 is shown. SO ₂ plume and it's perimeter (white contour) during the first 10 min segment of the flight is shown and labeled 1st. Also, the location of the aircraft and the direction of the flight (to the left) during this time is shown with white triangles. The same is shown for the 5th (yellow) and the 10th (green) 10 min segments of flight time. By looking at the consecutive contours (plume perimeters), it can be seen that the SO ₂ on the east wall is shifting to the left (south) as it is rising in altitude over time.	88
4.13	Flight 8 SO ₂ mixing ratio AFT krigged screen (a) compared to the mean VP screen (b) for the same flight. Shift in plume location over time results in oversampling and the appearance of a secondary plume on the AFT krigged screen. Note the difference in color scales.	89
4.14	Temporal evolution of temperature, wind speed and direction at $s = 5680$ m and $z = 500$ m during flight 8. Temperature increases, wind speed decreases and the wind direction shifts from SW to W.	91

List of Abbreviations

AFT Along The Flight Tracks

agl above ground level

amsl above mean sea level

AQ Air Quality

CEMA Cumulative Environmental Management Association

CNRL Canadian Natural Resources Ltd.

ECCE Environment and Climate Change Canada

GEM-MACH Global Environmental Multiscale-Modeling Air-quality and CHemistry

JOSM Joint Canada-Alberta Implementation Plan on Oil Sands Monitoring

SGI Sub-flight-level Gaussian Interpolation

TERRA Top-down Emission Rate Retrieval Algorithm

UAVs Unmanned Air Vehicles

VP Vertical Profiles

Chapter 1

Introduction

Responsible development of natural resources makes the study of its long-term cumulative effects on the environment crucial. Therefore, the development and improvement of methods and techniques and in general the science for informing environmental policy and decision making is essential. Developing methods for estimating emissions from sources such as oil sands facilities, is among the active areas of environmental research. Using aircraft based measurements provides a method for top-down emissions estimation with applications ranging from area sources the size of an individual industrial complex [12] to entire cities [16].

Aircraft-based measurements of pollutants are utilized to obtain the total integrated emissions of point and area sources. This approach provides a method to verify the inventory based estimates provided by facilities, and is advantageous particularly in estimating emissions from large area sources. Assessing emissions based on inventories is difficult for sources spanning tens to hundreds of square kilometers, where emissions can be due to various sources within a facility or from a combination of sources in several facilities and industrial districts. Aircraft-based top down emissions estimation overcomes such difficulties by capturing the total integrated emissions; this can be accomplished by flying around the area emission source in various flight patterns. Different flight patterns lead to different relative uncertainties in emissions estimation. Examples of such flight patterns are 1) flying perpendicular

to the mean wind at a single height downwind of the source [17] [23] [26], investigating the changes in the horizontal species mixing ratio and assuming the vertical mixing ratio to be constant with height; 2) flying over a single horizontal path at different heights downwind of the source to capture both the horizontal and the vertical change in species mixing ratio [5] [19]; and 3) by expanding on these two patterns and flying in a box shaped path around the facility to include not only a two dimensional vertical screen downwind of the source but also screens upwind and around the source [3] [16]. The latter approximates a box around the area source that captures the horizontal advective fluxes through its lateral sides. The box pattern can resemble any prism shape that is uniform with height (e.g. cylindrical, rectangular cuboid) [12]. By approximating losses through the box top and surface depositions and the horizontal advective fluxes measured during a box flight and applying the mass balance technique, the source emissions can be estimated with lower uncertainty levels compared to the other top-down approaches [12] [22].

During a summer intensive field campaign in August and September of 2013, several such box flights were conducted around the Canadian Athabasca oil sands facilities in northern Alberta. This project took place as part of the Joint Canada-Alberta Implementation Plan on Oil Sands Monitoring (JOSM). In support of JOSM, the Top-down Emission Rate Retrieval Algorithm (TERRA) was developed by Environment and Climate Change Canada (ECCC) to estimate the total integrated emissions by Canadian oil sands facilities based on the aircraft measurements during box flights [12]. Moreover, ECCC's air quality forecast model, the Global Environmental Multiscale-Modeling Air-quality and CHemistry (GEM-MACH), was modified to create air quality forecasts for the months of August and September 2013 at the region of the Canadian oil sands facilities in Alberta, to direct the airborne field campaign [18].

1.1 Related Work

During the Augsburg field campaign (EVA), in southern Germany, in 1998, aircraft based measurements of air pollutants were made. Kalthoff et al., used the technique of mass balance to assess the emissions of the city of Augsburg [16]. The aim of their emissions estimates based on airborne measurements was to evaluate emissions derived from the emission model of Institut fuer Energiewirtschaft und Rationelle Energieanwendung (IER), University of Stuttgart [15]. Two aircraft were flown on several days in October 1998 to perform box flights around the city of Augsburg. Flights were conducted during early afternoons when constant meteorological conditions (for periods of 1 to 2 hour) were expected, which is necessary for the application of the mass balance technique. CO and NO_x mixing ratio and meteorological measurements were made. Measured data were interpolated on a grid of 25 m × 25 m resolution and extrapolations were made for areas outside of the sampling heights (surface layer below the lowest flight level). Uncertainties in their estimates were mostly from the interpolation methods and the extrapolation schemes (two algorithms) for the layers below the lowest flight path to the ground. Emission rates calculations by Kalthoff et al. were mainly based on their estimations of advective fluxes. Hence, two main assumptions were made: 1) negligible temporal variations of the emissions and the mixed layer height and 2) negligible chemical reactions [16].

Panitz et al., performed simulations with the KAMM/DRAIS model system [2] [4] that accompanied and completed the experimental analysis performed by Kalthoff [22]. One of the objectives of the study was to investigate what percentage of the emissions can be deduced from advective fluxes alone. Emissions were modeled for the region of the city of Augsburg (area of 50 km × 50 km) with the horizontal resolution of 1 km × 1 km. Integrations over a volume of 10 km × 10 km (resembling the area that was enclosed during box flight measurements) were made to calculate the mass budget of NO_x

and CO. These were compared to known model emission inputs and they were able to show that the advective fluxes can be used to calculate 85% of NO_x and 95% of CO total emissions within the control volume. Further, Panitz et al., applied the concept of mass balance by using the model data extracted along the flight tracks during the actual aircraft measurements [16] for calculating the advective fluxes and compared their results to the results of Kalthoff et al. They projected and interpolated model temporal mean distributions (along the flight tracks) on a grid of $25 \text{ m} \times 25 \text{ m}$ resolution (same grid as the one used for analyzing aircraft-based measurements by Kalthoff et al. [16]) and estimated emissions by calculating the advective fluxes and applying the mass balance technique. In their comparisons, aircraft-based measurements were also treated as temporal mean distributions along the flight tracks. Their results of these comparisons showed overestimations in emissions determined solely from advective fluxes compared to model input emissions.

Mölders et al., examined the feasibility of using Unmanned Air Vehicles (UAVs) for air-quality advisory [20] [21]. Their objective was to examine whether UAVs (airborne measurements) can provide reliable mean spatial distributions of air-quality relevant quantities. To achieve this, they simulated wildfire-smoke conditions over Alaska by running the WRF/Chem model [1] [13]. They referred to the modeled wildfire-smoke as the “grand truth”, and flew a virtual UAV at different speeds, altitudes and flight patterns within the model. The virtual UAV sampled model meteorology and concentration data. UAV flight times were 20 model hours for each flight design. To examine the sensitivity of temporal mean distributions on UAV’s flight patterns, altitudes and speeds, they compared the sampled data to the model mean distributions, the “grand truth”. Their results of comparing 20 hr means to the “grand truth” showed the impact of the diurnal cycles of sampled chemicals’ concentrations, which showed overestimations in regions of high concentration and underestimations in regions of low concentration.

They also showed the sensitivity of sampled distributions on flight patterns, speeds and altitudes during a frontal passage. Their results showed that different flight speeds result in different sampled distributions which can lead to under or overestimations.

1.2 TERRA

Top-down Emission Rate Retrieval Algorithm (TERRA) is an algorithm for estimating the total integrated emissions of pollutants (e.g. SO₂ and CO) by an area source (facility). “In this algorithm, the flight path around a facility at multiple heights is mapped to a two-dimensional vertical screen surrounding the facility” [12]. Interpolation between different flight levels is used to fill this screen, and the gap between the lowest flight path and the ground, ~150 m, is filled with extrapolation schemes chosen based on the known boundary-layer meteorological empirical approximations. TERRA estimates area emission rates by equating the change in mass within a control volume (the volume surrounded by the two dimensional screen around the facility as described above) with the integrated mass flux through the walls of the control volume (divergence theorem).

1.2.1 Emissions Algorithm

The mass balance for air within the control volume is,

$$E_{air,H} + E_{air,V} - E_{air,M} = 0 \quad (1.1)$$

Where $E_{air,H}$ is the horizontal advective flux through the lateral sides of the control volume (box) and $E_{air,V}$ is the vertical advective air flux through the top of the box. $E_{air,M}$ is change in air mass within the control volume. Advective fluxes are set to be positive for the outgoing flux and negative for the flux entering the box (e.g. $E_{air,H} = E_{air,H,out} - E_{air,H,in}$). The flux sign can be determined using the normal wind vector $U_{\perp}(s, z)$, which is also

positive outwards

$$U_{\perp}(s, z) = \frac{U_N \partial s(x, y) / \partial x - U_E \partial s(x, y) / \partial y}{\sqrt{(\partial s(x, y) / \partial x)^2 + (\partial s(x, y) / \partial y)^2}} \quad (1.2)$$

The screen path length $s(x, y)$ is a function of longitude, x , and latitude, y . U_E and U_N are easterly and northerly winds respectively. The integral form of the horizontal advective flux is given as follows,

$$E_{air,H} = \iint_{Sides} \rho_{air} U_{\perp} ds dz \quad (1.3)$$

where ρ_{air} is the air density and U_{\perp} is the wind normal to the box wall (Equation 1.2). $E_{air,M}$, which represents the change in air mass within the control volume, can be estimated as follows,

$$E_{air,M} = \iiint \frac{\partial \rho_{air}}{\partial t} dx dy dz = \frac{A}{\Delta t} \left(\frac{\Delta P}{P} - \frac{\Delta T}{T} \right) \int \rho_{air} dz \quad (1.4)$$

where P and T are average pressure and temperature, A is the area enclosed by the box (control volume), and ΔP and ΔT are change in pressure and temperature during the flight time Δt . $E_{air,M}$ is positive when air mass is added to the volume and negative when subtracted, resulted from change in air density. The remaining term in Equation 1.1, $E_{air,V}$, is calculated from determined values of $E_{air,H}$ and $E_{air,M}$.

The mass balance relation for the compound C in the control volume is described as follows

$$E_C = E_{C,H} + E_{C,HT} + E_{C,V} + E_{C,VT} + E_{C,VD} - E_{C,M} - E_{C,X} \quad (1.5)$$

where E_C is the total emissions rate, $E_{C,H}$ is the horizontal advective flux, $E_{C,HT}$ is the horizontal turbulent flux, $E_{C,V}$ is the advective flux through the box top, $E_{C,VT}$ is the turbulent flux through the box top, $E_{C,VD}$ is the deposition to the surface, $E_{C,M}$ is the increase in mass within the volume due to change in air density and $E_{C,X}$ is the increase in mass due to chemical

changes. The integral description of some of these terms are shown here

$$E_{C,H} = M_R \iint_{Sides} \chi_C \rho_{air} U_{\perp} dsdz \quad (1.6)$$

$$E_{C,VD} = M_R \iint_{Bottom} \chi_{surf,C} \rho_{air} V_D dx dy \quad (1.7)$$

$$E_{C,V} = M_R \iint_{Top} \chi_{top,C} \rho_{air} w dx dz \quad (1.8)$$

$$E_{C,M} = M_R \iiint \chi_C \frac{d\rho_{air}}{dt} dx dy dz = \frac{AM_R}{\Delta t} \left(\frac{\Delta P}{P} - \frac{\Delta T}{T} \right) \int \chi_C(z) \rho_{air} dz \quad (1.9)$$

where M_R is the ratio of the compound molar mass to the molar mass of air (64.07/28.97 for SO₂ and 28.01/28.97 for CO), χ_C is the species mixing ratio, $\chi_{surf,C}$ is the species mixing ratio at the surface and V_D is the deposition velocity. $\chi_{top,C}$ is the species mixing ratio at the box top and w is the vertical wind speed, positive upwards.

If $\chi_{top,C}$ is approximated to be constant over the box top and equal to the average mixing ratio of the compound at the top of the screen, $\bar{\chi}_{top,C}$, it can come out of the integral.

$$E_{C,V} = M_R \bar{\chi}_{top,C} \iint_{Top} \rho_{air} w dx dz$$

The remaining integral term, $\iint_{Top} \rho_{air} w dx dz$, is just the integrated vertical advective air flux, $E_{air,V}$. Then the above equation reduces to,

$$E_{C,V} = M_R \bar{\chi}_{top,C} E_{air,V} \quad (1.10)$$

1.2.2 Near Surface Extrapolations

TERRA has five different extrapolation methods available to fill the gap between the lowest flight level, $z_L(s)$, and the surface, $z_g(s)$, where there were no measurements [12]. Figure 1.1 shows SO₂ mixing ratio screens, generated using the data collected along the flight tracks (black dots) during flight 8.

Screens are extrapolated below the lowest flight level using methods available in TERRA. These methods are described as follows,

- **Zero:** assumes an elevated plume, completely located above the lowest flight level $z_L(s)$ and gives a mixing ratio of $\chi_C(s, z) = \text{background}$ (zero for compounds such as SO_2 with near zero background concentrations) for $z_g < z < z_L$
- **Zero to Constant:** assumes a zero (minimum) concentration at the surface, $\chi_C(s, z_g) = \chi_{min,C}$, and a linear interpolation between $\chi_C(s, z) = \chi_C(s, z_g)$ and $\chi_C(s, z) = \chi_C(s, z_L)$ for $z_g < z < z_L$ (Figure 1.1a)
- **Constant:** assumes an elevated plume with constant concentrations below the lowest flight level. This constant is taken such that $\chi_C(s, z) = \chi_C(s, z_L)$ for $z_g < z < z_L$ (Figure 1.1b)
- **Linear fit:** assumes a maximum concentration $\chi_C(s, z_g) = \chi_{C,max}$ at the surface and a concentration profile, decaying linearly with height between $\chi_C(s, z) = \chi_{C,max}$ and $\chi_C(s, z) = \chi_C(s, z_L)$: $\chi_C(s, z) = \chi_{C,max} + \alpha z$ for $z_g < z < z_L$. $\chi_{C,max}$ and α (negative) are determined from a least-square fit at each s (with a spacing of 40m), from the ground up to $z(s) = z_g + \acute{z}$ (with $\Delta z = 20m$). Where \acute{z} is an adjustable height parameter (250 - 500m). See Figure 1.1c.
- **Exponential fit:** assumes a half-Gaussian profile with a maximum concentration $\chi_C(s, z_g) = \chi_{C,max}$ at the surface, which is decaying with height between $\chi_C(s, z) = \chi_{C,max}$ and $\chi_C(s, z) = \chi_C(s, z_L)$ for $z_g < z < z_L$

$$\chi_C(s, z) = a_0 + a_1 e^{-\left(\frac{z-z_g}{a_2}\right)^2}$$

with constants a_0 , a_1 and a_2 determined from the fit (from the ground up to $z_g + \acute{z}$) at each s ($\Delta s = 40m$). See Figure 1.1d.

One or several of these methods, depending on the nature of the plume and the meteorological conditions, can be used to estimate the concentration pro-

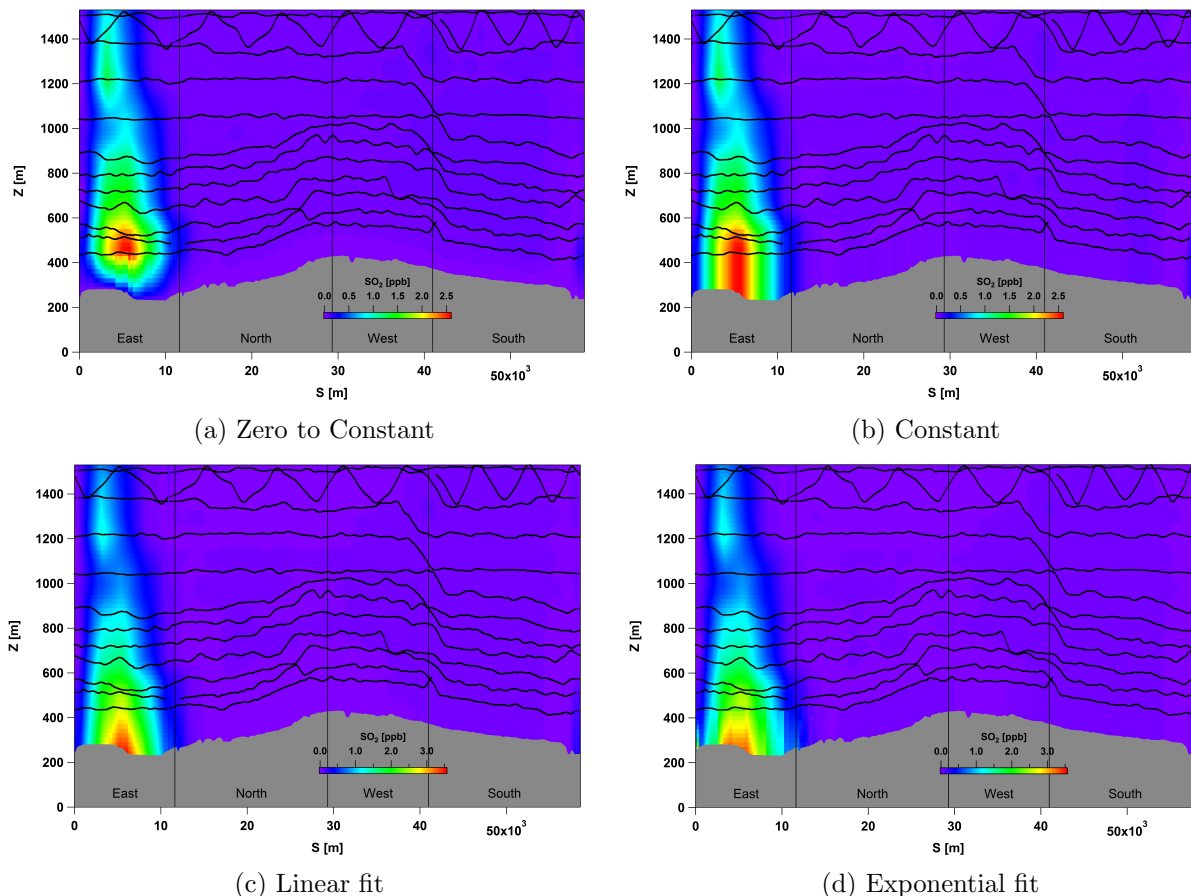


Figure 1.1: Flight 8 SO_2 concentration screens generated based on data extracted from GEM-MACH, extrapolated below the lowest flight level. Flight tracks superimposed on the screen (black dots). Four TERRA extrapolation methods, Zero to Constant, Constant, Linear fit and Exponential fit are shown.

files within the surface layer.

1.3 GEM-MACH Model

Global Environmental Multiscale-Modeling Air-quality and CHemistry (GEM-MACH) is ECCC's operational on-line Air Quality (AQ) forecast model embedded in the Canadian weather forecast model GEM [7]. In an on-line model the meteorology (GEM) and chemistry (MACH) models are coupled and run simultaneously, as opposed to an off-line model with a separate chemical transport model (CTM) and a meteorological model (MM). GEM offers a nested regional limited-area grid configuration in addition to two global con-

figurations. The regional configuration of GEM is GEM15, covering North America with a uniform resolution of 15 km [25]. GEM-MACH15 grid is a sub-grid of GEM15 with co-located grid points (Figure 1.2). Since 2009, GEM-MACH15 has been in use as ECCC’s operational AQ forecast model [8]. GEM-MACH15 uses a continental scale domain (rotated longitude and latitude grid) with 348×465 grid points with horizontal grid spacing of 15 km and with 58 vertical levels from the surface to 0.1 hPa (~ 30 km) [8] [25].

As part of JOSM, the GEM-MACH system was reconfigured to create nested forecasts of air quality at model grid resolutions down to 2.5 km, with the highest resolution domain including the Canadian provinces of Alberta and Saskatchewan [18]. Nesting was performed in three levels: 1) 10km/36hr continental forecast, feeding 2) 10km/30hr W. Canada/NW. USA forecast, feeding 3) the 2.5km/24hr Alberta/Saskatchewan domain (Figure 1.3). GEM-MACH uses both 2-bin and 12-bin sectional representation of aerosol size distribution [8]. There are two different types of emissions, gridded surface emissions and major point sources. Emission fields are prepared for months, days and hours. Emissions are set to be constant for 2 min chemistry (60 s meteorology) time steps subdividing each hour [25]. The Cumulative Environmental Management Association (CEMA) emissions inventory was used for the Alberta region of oil sands [6]. The air quality forecasts created by GEM-MACH were used to direct the summer intensive airborne field campaign during the months of August and September 2013 in Alberta. Model predictions were compared to both the airborne and the ground based monitoring network system.

1.4 Investigating Emissions Estimates Using GEM-MACH With TERRA

The main known source of uncertainty in estimating emissions using TERRA is the extrapolation schemes used to estimate species mixing ratios for the

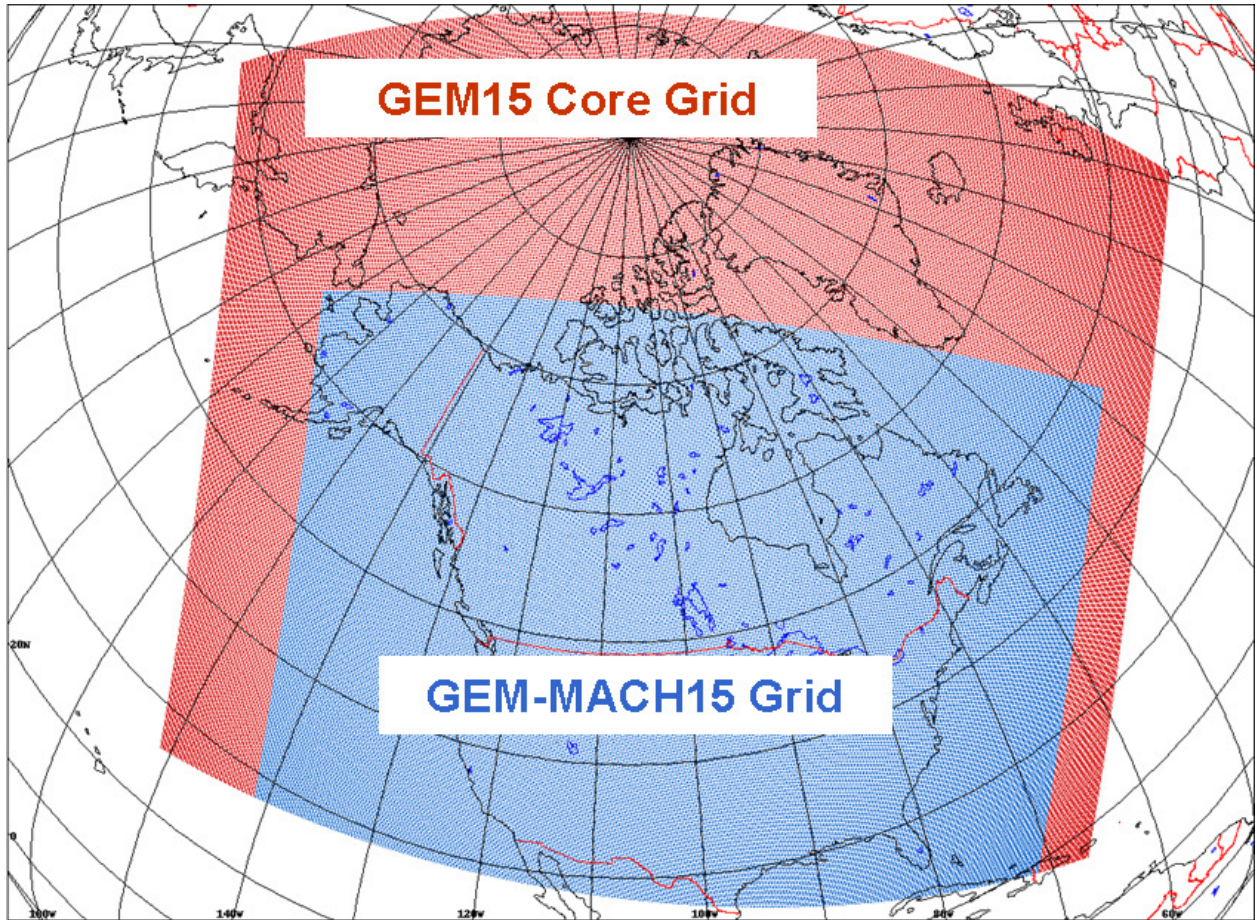
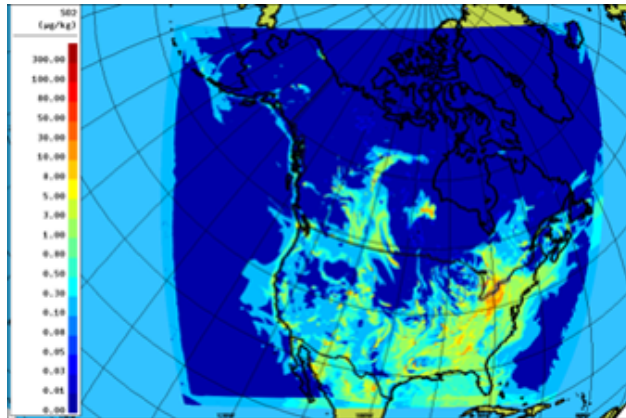
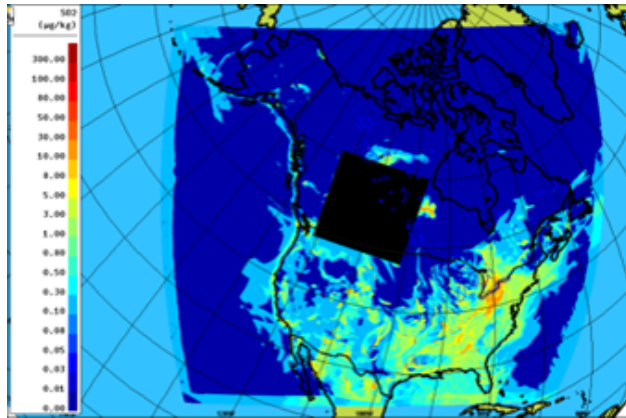


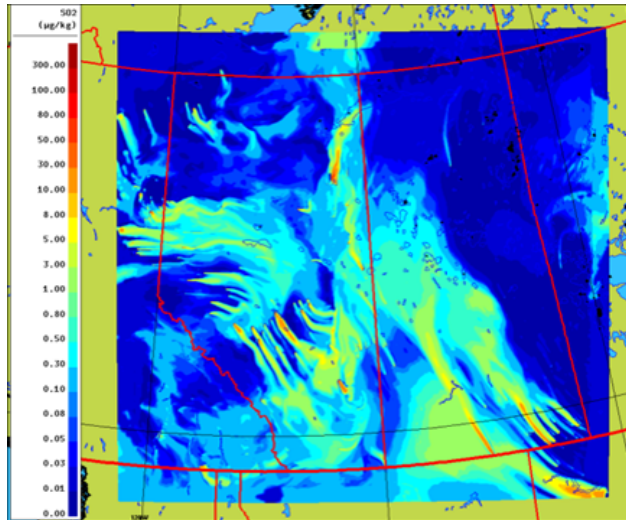
Figure 1.2: GEM-MACH15 grid is a sub-grid of GEM15 with co-located grid points , covering North America [8].



(a) 10km/36hr continental forecast



(b) 10km/30hr W. Canada/NW. USA forecast



(c) 2.5km/24hr Alberta/Saskatchewan domain

Figure 1.3: Three-level nested grid of GEM-MACH used in ECCC Oil Sands simulations [18]. SO_2 concentrations are plotted here.

heights below the lowest flight level (~ 150 m agl) to the ground where no measurements were made [12]. In addition, the temporal evolution of the emissions and the meteorological conditions during the approximately 2 hours flight time, add to the uncertainties. In an effort to investigate these uncertainties and suggest improvements in TERRA, model output from ECCC's air quality model was used as a surrogate source of concentration and meteorology data. Running TERRA against a known source offers an approach for evaluation of the algorithm's performance. This was accomplished by extracting the model concentration and wind vectors along the aircraft flight tracks from GEM-MACH for flights on August 20 and September 3 of 2013, around the CNRL and Syncrude facilities respectively, and using them as TERRA inputs for emissions estimations. For our analyses, SO_2 was chosen to represent emissions from a stack source with low background level, and CO was chosen to represent emissions from ground area sources with a relatively high background level. Gordon et al., in their analysis of the aircraft-based measurements during the 2013 campaign, estimated that the advective fluxes account for 99% of SO_2 total emissions [12]. Panitz et al., showed that 95% of CO emissions can be solely described by advective fluxes [22]. Hence, our analyses of CO and SO_2 emissions rate retrieval were focused mainly on advective processes. Results were compared to the known GEM-MACH model inputs for TERRA evaluations.

The aim of this work is to assess the uncertainties in and improve upon extrapolation schemes used with the mass balance technique in TERRA, test the assumption of meteorological steady state and constant rate emissions during the flight time (~ 2 hours) and also to evaluate the emissions derived from the GEM-MACH model. To accomplish this, data were extracted from the GEM-MACH model in two different methods; simulating aircraft-based measurements and extracting data along the flight tracks, and extracting vertical profiles from the model following the aircraft sampling time stamps during flights 8 and 18 on 20 Augusts and 3 September respectively. The

methods are described in Chapter 2. SO_2 and CO emission rates were estimated employing different methods for flights 8 and 18 around CNRL and Syncrude facilities and results are compared to model emission inventories in Chapter 3. Further, evaluating the performance of the aircraft-based emissions rate retrieval with regards to how the flights were conducted during the field campaign (flight patterns, flight time, etc.) can provide useful suggestions for future flight plans. Results and suggestions for improving aircraft-based methods are discussed in Chapter 4.

Chapter 2

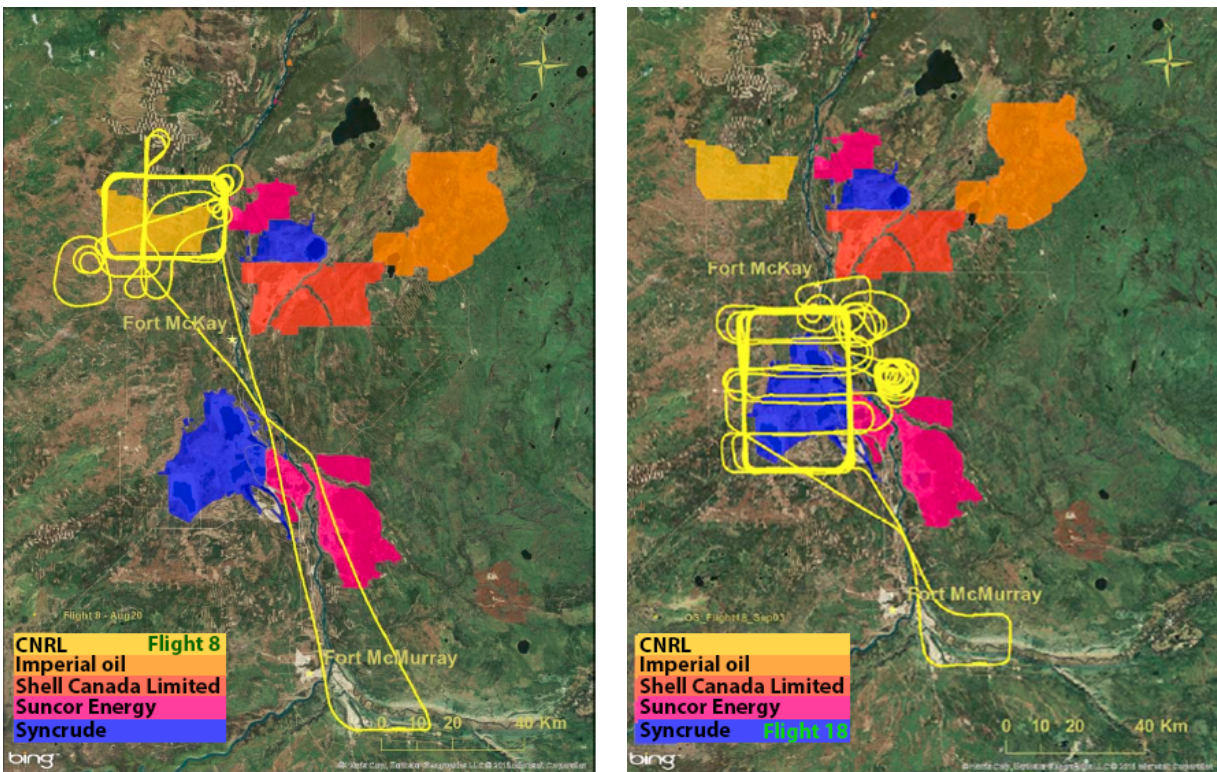
Methods

In order to mimic the airborne measurements, a virtual airplane was flown within the GEM-MACH model along the actual flight tracks from the 2013 field campaign. Wind and compound concentrations were extracted from the model. Following the schemes in TERRA, extrapolations to the surface were made and the mass balance technique was used for emissions estimates. The vertical profiles of the species concentration and the wind vectors were also extracted for the entire height of the test volume (including the heights below the lowest flight track to the surface) for every 10-15 minutes (flight time at each height level) of the box flight time from the GEM-MACH model, to both evaluate the uncertainties in extrapolation methods and to investigate the uncertainties in emissions estimates due to the temporal evolution of the system under the study. Finally, the emission rates retrieved using the above approaches are compared to the mass budget input in the GEM-MACH model to evaluate the 1) performance of the forecast model 2) investigate the sensitivity of the airborne emissions rate retrieval on the flight patterns and suggest improvements for the future flights.

2.1 Two Study Cases: Flights 8 and 18

In this study the focus is on two cases from 20 August and 3 September during the 2013 field campaign [12]. GEM-MACH created forecasts for each of these

days; the CO and SO₂ emissions inventory for facilities CNRL and Syncrude that was used in the model are presented in Tables 2.1 and 2.2 [6]. For our work, SO₂ was chosen to represent stack emissions with low background levels and CO was chosen to represent area source emissions with relatively high background levels (due to CO emissions from natural and anthropogenic sources). The sensitivity of the estimations and the level of uncertainties for each method is dependent on the nature of the emissions (e.g. low vs. high background). Choosing different sources helps investigating this dependence.



(a) Flight 8 on August 20, 2013 (CNRL)

(b) Flight 18 on September 3rd, 2013 (Syncrude)

Figure 2.1: Flight paths from the Fort McMurray Airport to and around oil sands facilities CNRL and Syncrude on August 20 and September 3 of 2013 respectively. These two flight tracks were used to extract data from the GEM-MACH model for emissions estimation with TERRA.

On 20 August the aircraft flew a rectangular path around the CNRL facility and on 3 September the aircraft flew another box flight around Syncrude (Figure 2.1). A “Box Flight” is comprised of several rectangular flight tracks at consecutive levels such that the resulting flight path approximates a rectangular prism that surrounds the region of a single facility (Figure 2.2). CNRL

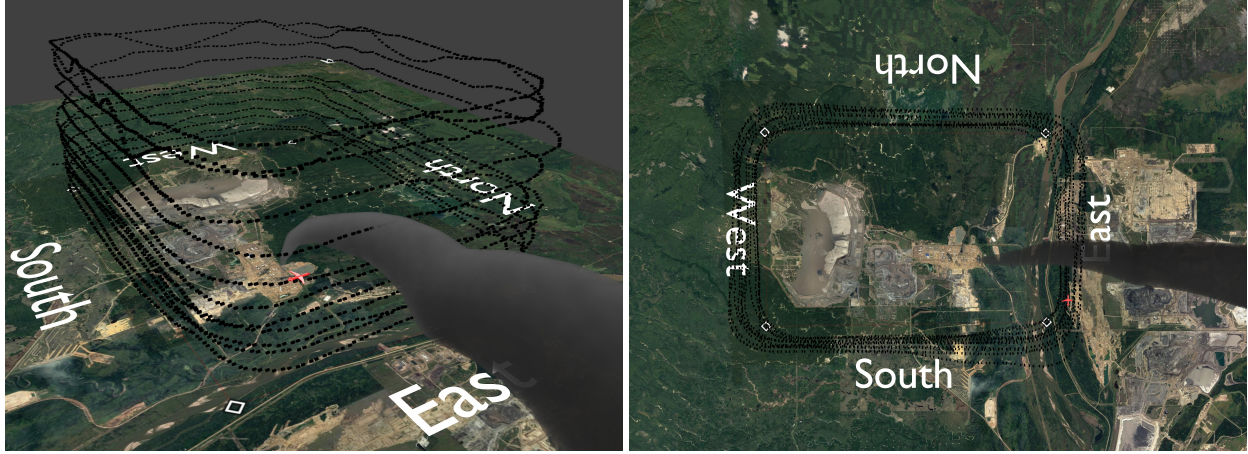
Table 2.1: Emissions inventory by Canadian Natural Resources Ltd., input in GEM-MACH for 20 August 2013 forecast (Flight 8) [6].

Source Type	Facility ID	Co. Name	Facility Name	SO ₂ Total	CO Total
Point Stack Emission	48905	CNRL	Horizon Project	505.52 [kg/hr]	170.81 [kg/hr]
Off-road Mine Fleet	48905	CNRL	Horizon Project	8.21 [kg/hr]	75.19 [kg/hr]
Average Total				513.73 [kg/hr]	246 [kg/hr]

Table 2.2: Emissions inventory by Syncrude Canada Ltd., input in GEM-MACH for 3 September 2013 forecast (Flight 18) [6].

Source Type	Facility ID	Co. Name	Facility Name	SO ₂ Total	CO Total
Point Stack Emission	48902	Syncrude	Mildred Lake	9030.54 [kg/hr]	739.31 [kg/hr]
Point Stack Emission	48904	Syncrude	Aurora North	0.00 [kg/hr]	36.87 [kg/hr]
Off-road Mine Fleet	48902	Syncrude	Mildred Lake	51.12 [kg/hr]	270.40 [kg/hr]
Off-road Mine Fleet	48904	Syncrude	Aurora North	12.70 [kg/hr]	145.85 [kg/hr]
Average Total				9094.36 [kg/hr]	1192.43 [kg/hr]

and Syncrude are the two facilities on the far west side (at different latitudes) of the Athabasca oil sands region with no nearby industrial sites on their west; all the other facilities are located east of these two (Figure 2.1). Winds were westerly during both flights 8 and 18, thus minimum concentrations from emissions by nearby facilities were picked up by the aircraft along the lateral walls of the control volume (Figure 2.2). Therefore, these two flights were chosen, out of the total of 22 flights during the 2013 field campaign, to minimize the uncertainties in emissions estimations due to the background emissions (from sources located outside of the control volume/box flight). The aircraft state parameters (Lon., Lat., Alt.) during each flight were reported at 1 Hz. These parameters were then used to determine the flight path within the GEM-MACH model. To simulate the aircraft based measurements, a virtual aircraft was flown within the model along the predetermined flight paths and meteorology and concentration data were extracted from the model.



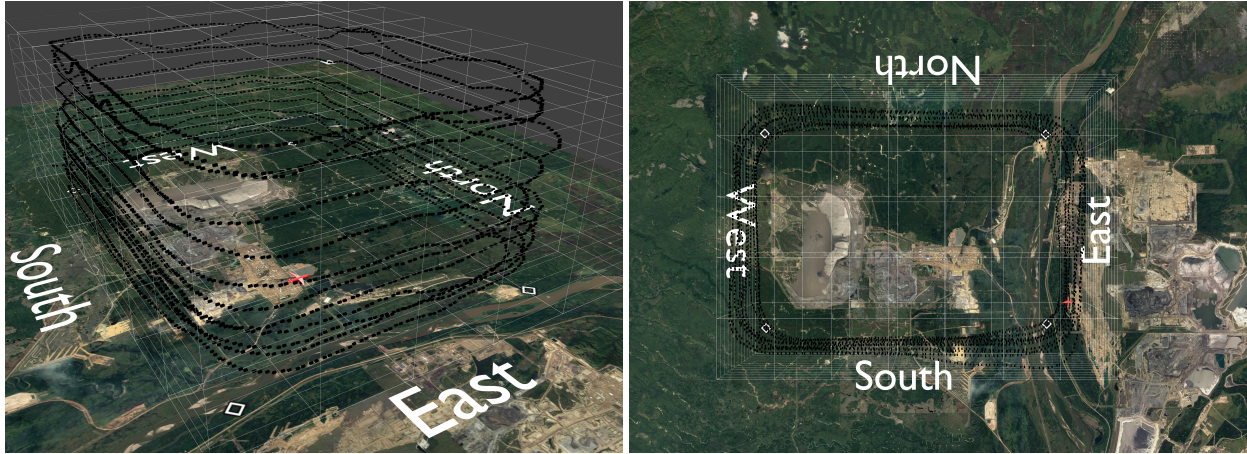
(a) Flight 8, viewed from east

(b) Flight 8, viewed from top

Figure 2.2: A Box flight is realized by flying an aircraft in a rectangular path at several consecutive levels around a region of interest. In this illustration, such a box flight is shown around the CNRL facility during the flight 8. The flight tracks are shown with black circles, at 1 Hz. Also, the turning points along the aircraft’s horizontal path are marked with gray squares on the map of the region. A schematic representation of a plume from a stack within the facility is shown. The plume is incident on the eastern side of the box, were it is registered by the aircraft along the flight tracks.

2.2 Flying Within The Model

Mimicking aircraft-based measurements, the virtual airplane was flown along the predetermined flight tracks within the GEM-MACH model. The model has a 2.5 km horizontal grid size and 32 vertical levels with vertical grid sizes varying from 35 m (near the ground) to 425 m (at ~ 7 km agl); the vertical grid spacing was approximated from GEM-MACH’s 30 vertical pressure levels. Figure 2.3 shows an illustration of the CNRL facility region surrounded by flight tracks of flight 8, enclosed by grid spacing of the GEM-MACH model. Wind vectors, water mixing ratio, temperature, species mixing ratio (SO_2 and CO) and surface elevation profiles were extracted from the GEM-MACH model’s cells, with 2.5 km by 2.5 km cross-section, which was co-located with the aircraft along flight tracks. Further, the extracted values were linearly interpolated in space to match the frequency of the aircraft measurements (1Hz and spaced ~ 100 m apart). The two different approaches for extracting data from the GEM-MACH model, 1) flying along the flight tracks (section



(a) Flight 8, viewed from east

(b) Flight 8, viewed from west

Figure 2.3: The same box flight as in Figure 2.2. In this illustration cell structure of the GEM-MACH model is also shown in white grid lines. The grid squares are spanned by 2.5 km horizontally on each side and to the scale. The vertical grid spacing is not to the scale and is actually not monotonic in size as it is depicted here, but it increases progressively from 35 m high for the cells near the ground surface to about 200 m at the top of the "box" at a height of about 1450 m agl, highest flight level during flight 8. The flight tracks, represented by black circles, are overlaid with the model grid. The hypothetical aircraft (in red), travels through the model cells along the box flight path and extracts meteorological data and species (e.g. SO_2 , CO) concentrations from each cell, mimicking aircraft-based measurements. The extracted data from the model cells (spaced 2.5 km horizontally) are then interpolated in time and space, down to 100 m spacing between each two point, to match the frequency of the aircraft measurements during the field campaign (every second).

2.2.1), and therefore simulating aircraft measurements, and 2) expanding on the first approach by extracting data in vertical columns (surface to ~ 7 km agl) following the aircraft's horizontal path (section 2.2.2), are explained next.

2.2.1 Along The Flight Tracks (AFT)

In this approach, the aircraft-based measurements for top down emissions estimation are simulated. The aim is to mimic all the steps performed during the 2013 field campaign, this time within the GEM-MACH model; from measuring the wind vectors and species concentrations to emissions estimations using TERRA. The time series of the state parameters (Lon, Lat, Alt) of the aircraft during each of the 22 flights were recorded, thus the path of a certain

flight (e.g. flight 8) can be determined using these parameters. A virtual aircraft is flown along the predetermined flight tracks within the GEM-MACH model; the aircraft travels through the model cells (each spanning 2.5 km horizontally on each side) that are collocated with aircraft locations along the flight tracks at each time-stamp. Figure 2.4 illustrates such a model cell, highlighted in red, that represents the aircraft's state parameters at the corresponding time-stamp. The portion of the plume engulfed by the sampling cell (one of the model cells comprising the plume that is collocated with the sampling volume) is represented as species average concentration within the volume of the sampling cell. All model cells, including those along the flight tracks, contain meteorology and concentration data that could be extracted for each time-stamp. Meteorology and species concentrations are then extracted from these model cells for every 2 min of the flight along the flight tracks, which mimics aircraft-based measurements with a frequency 120 times less than that of the actual aircraft-based measurements of 1 Hz sampling frequency during the field campaign. The extracted data is then interpolated linearly in space to match the 1 Hz frequency of aircraft-based measurements. Next, following the TERRA schemes, these extracted values are mapped onto a two-dimensional screen surrounding the facility (Figure 2.5a). This is the first of four steps required for preparing a screen for emissions estimation. Such a screen is generated for every extracted parameter (e.g. wind vectors, concentrations). The other three steps are as follows: 2) the kriging method [14] is used for the interpolation of each screen (Figure 2.5b), 3) for the elevations below the lowest flight path, where there were no data extraction, a simple kriging interpolation would not be suitable; therefore, the screen is emptied below the lowest flight level (Figure 2.5c) to be 4) filled by an extrapolation method, depending on meteorological conditions and the nature of species under study (Figure 2.5d). TERRA has several different methods of extrapolation available (subsection 1.2.2), for values below the lowest flight level down to the ground surface [12]. The screens that

are generated in this way are the four lateral sides of the box flight (control volume), unwrapped into a single 2D screen (Figure 2.5a). These screens and the application of the mass balance technique for emissions estimation, are at the core of the TERRA method. In this method, the control volume is surrounded by a screen that is traced by an aircraft flying around the facility; therefore, the system is assumed to be in steady state during the flight time of ~ 2 hours. Thus, two assumptions must be made before analyzing the data and retrieving emissions: 1) constant emission rate by the facility and 2) meteorological steady state during the flight time (the time it takes to extract data for generating a screen). Of these two assumptions the first is met since the emissions inventory of the GEM-MACH model is set to the constant value of the average hourly emissions over a month, see Tables 2.1 and 2.2. The latter however, is the assumption that adds to the uncertainties due to the meteorological temporal evolution of the system during the flight time.

2.2.2 Vertical Profiles (VP)

In a different approach, again a virtual aircraft is flown along the flight tracks; but this time in addition to values along the flight tracks, vertical profiles from the surface up to ~ 7 km are also extracted from the model and linearly interpolated in time and space to 1 Hz (frequency at which aircraft measurements were reported during the 2013 field campaign). Figure 2.6 illustrates the same box flight as in Figure 2.4; the major difference is the vertical extent of the sampling volume. In this case, a column comprised of several model cells, with the same longitude and latitude but at different elevations stacked on top of each other, forms the sampling volume. The sampling volume, highlighted as a rectangular column in Figure 2.6, follows the horizontal path of the aircraft at each time-stamp. The column follows the aircraft along the flight tracks and sweeps around the box flight, covering the entire lateral sides of the box at every circuit around the facility. The extracted data from the

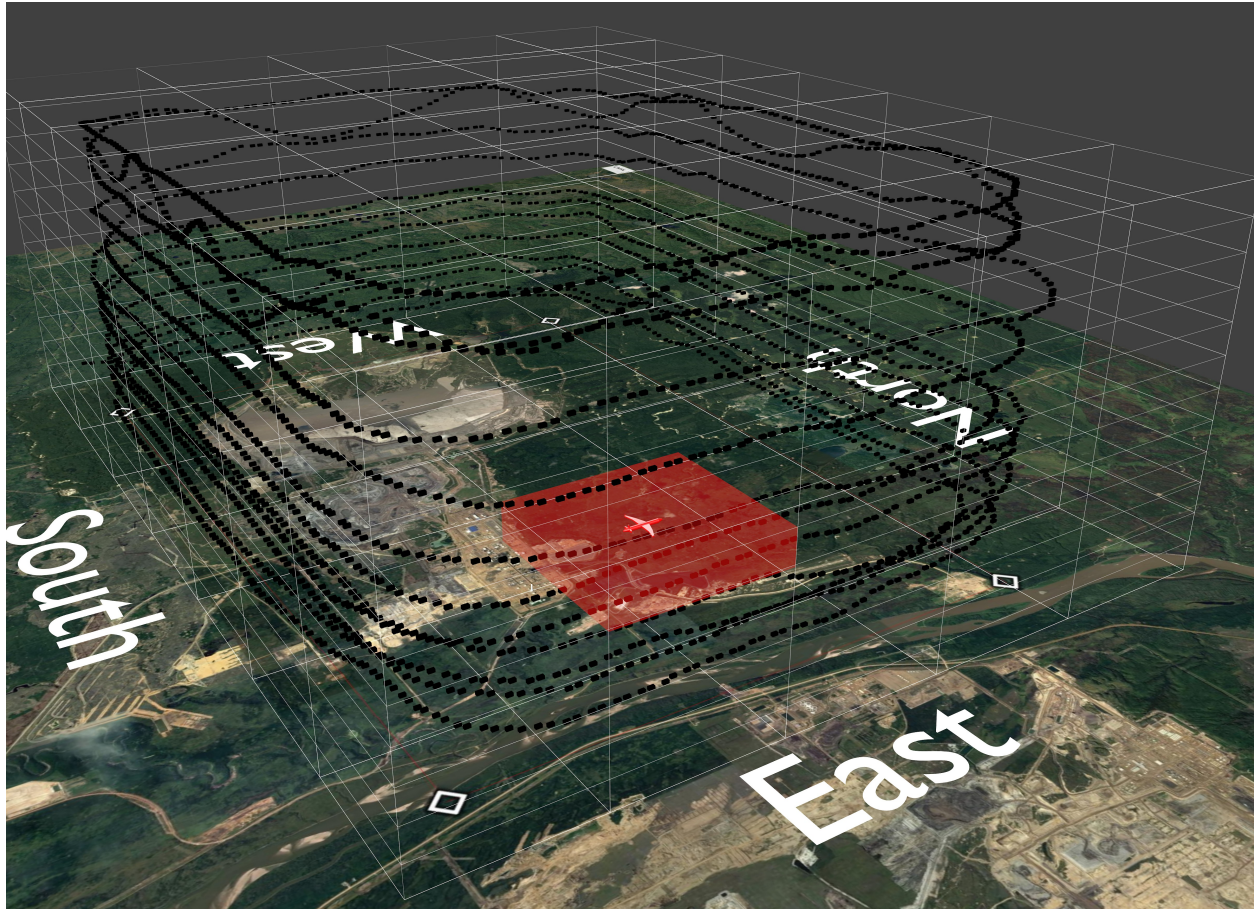
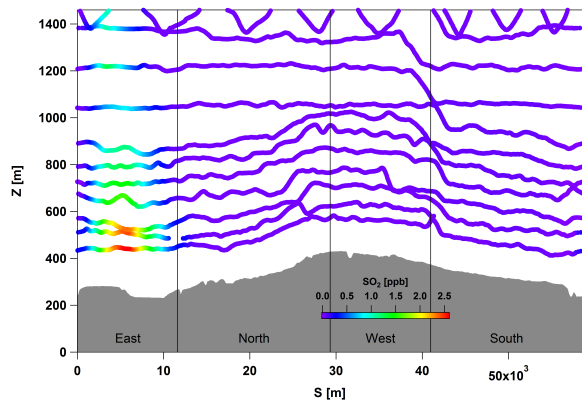
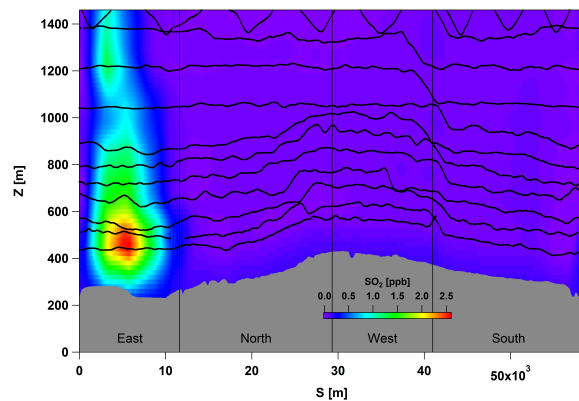


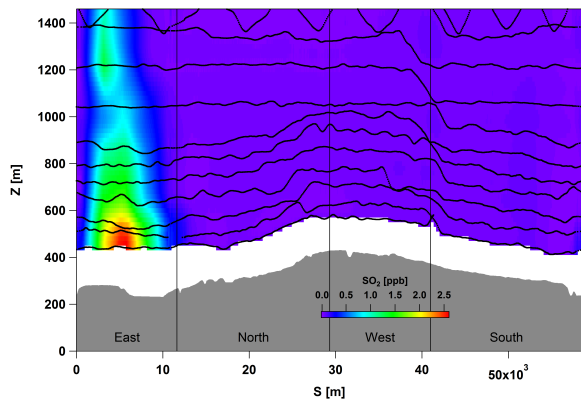
Figure 2.4: The region of the CRNL facility, flight 8 tracks (black circles) and GEM-MACH model grid spacing (white) are illustrated. The model cell, highlighted in red, is representing aircraft's (also red) state parameters along the flight tracks within the model. The highlighted model cell is the sampling volume. Extracting meteorology and concentration data from each individual cell along the flight tracks, simulates aircraft-based measurements. The species concentration corresponding to the portion of the plume engulfed by the cell, adds to the overall concentration within the sampling cell volume.



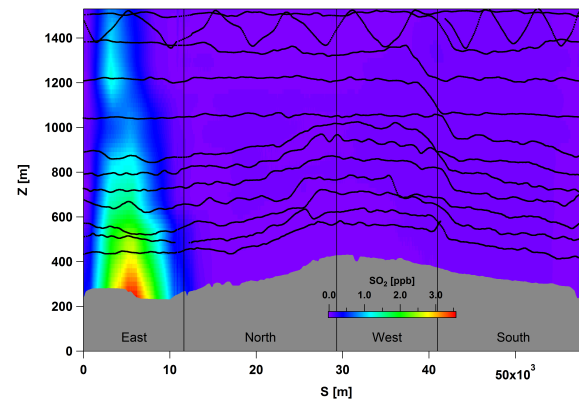
(a) Extracted concentrations along flight tracks



(b) Kriging interpolation of the screen



(c) Kriged screen emptied below the lowest flight



(d) Extrapolating linearly towards ground

Figure 2.5: Four steps of generating an SO_2 concentration screen from the model extracted values along the flight tracks of flight 8, on 20 August 2013 around the CNRL facility. Flight 8 tracks are superimposed with black dots and the box lateral walls are labeled with geographical directions East, North, West and South.

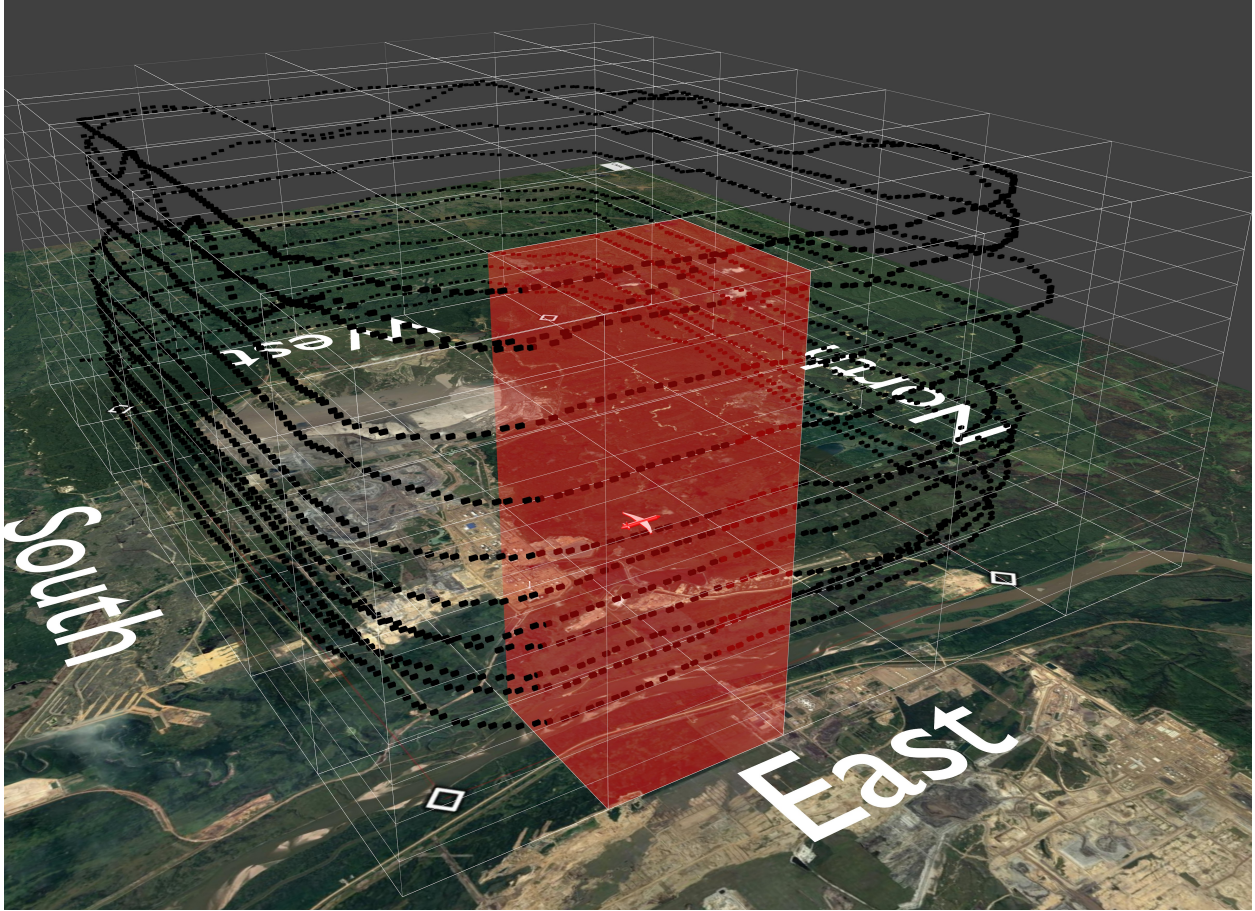


Figure 2.6: The region of the CRNL facility, flight 8 tracks (black circles) and GEM-MACH model grid spacing (white) are illustrated. The sampling volume is highlighted as a red column, comprised of several model cells stacked on top of each other, with the same longitude and latitude as the aircraft (red) along the flight path. This column sweeps all the lateral sides of the Box as the aircraft travels around the facility at each level. Extracting meteorology and concentration data from this sampling volume, provides enough data to generate a screen for every flight level.

column, which extends vertically from the surface to ~ 7 km agl (32 levels), covers the entire vertical extent of the screen comprised of four lateral walls of the box (between the surface and 1.6 km) including the 150 m gap between the surface and the lowest flight level (Figure 2.7a). As before (section 2.2.1), the extracted data is mapped onto a two dimensional screen, comprised of four lateral sides of the box. The screen is then filled by linear interpolation between extracted vertical columns (Figure 2.7b). In this approach, there is no need for extrapolation below the lowest flight level since the extracted profiles cover the entire extent of the screen vertically; which results in re-

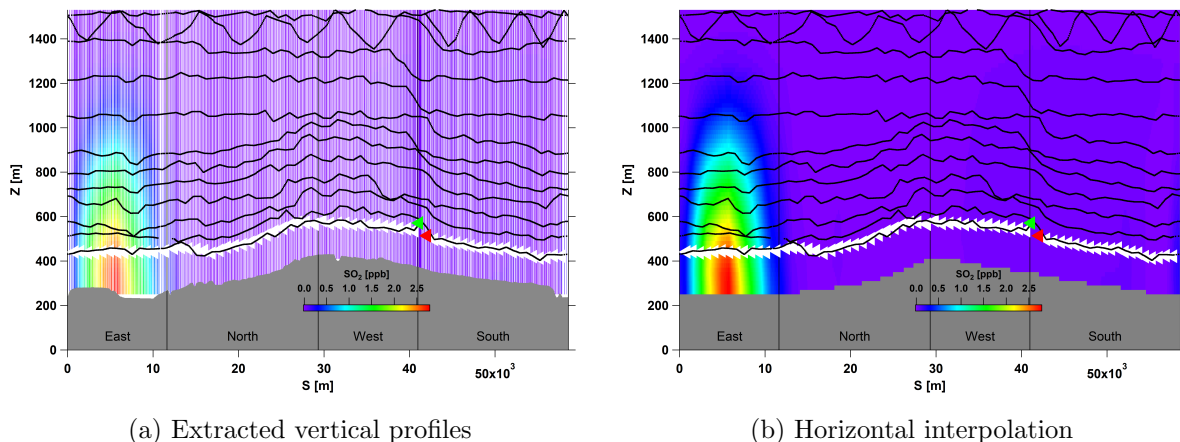


Figure 2.7: SO_2 concentration screen, generated for the first 10 min of the flight 8; In two steps: 1) extracting vertical profiles and interpolating vertically between points and 2) Interpolating horizontally between the vertical profiles and filling the screen. The location and direction (to the left) of the aircraft along the first flight track is shown with white triangles. The green and red triangles mark the start and end point at this level. In this case, vertical profiles extracted along the flight track at the lowest level, were used to construct a screen for the first 10 min of flight 8.

duced uncertainties and provides a means for investigating the uncertainties arising from extrapolations.

For this Aug 20 CNRL flight (flight 8), it takes the aircraft between 10 to 15 minutes to fly around the facility once. Since the sampling volume covers the entire vertical extent of the screen at each circuit around the facility, enough data can be extracted to generate a whole screen. Generating screens for every 10-15 minutes of the flight, covers 5-7 model time steps because the chemical time-step of the GEM-MACH model is 2 minutes with a meteorological time-step of about 1 minute. Analyzing the generated screens for emissions estimation, assuming meteorological steady state over a time period of 10-15 minutes, is an improvement upon the 2-hour steady state assumption (section 2.2.1). This allows evaluation of the steady state assumption by studying the temporal evolution of the system, and the resulting uncertainties in emissions estimation using TERRA, while the GEM-MACH model emissions inventory is set to a constant rate by design. For the case of an approximately 2 hour box-flight, about 12 consecutive screens for each of the parameters (e.g. wind vectors, concentrations) can be generated. See Figure

2.7b for SO₂ concentration screen for the first 10 minutes of flight 8, generated using the vertical profiles extracted along the flight tracks at the lowest level (highlighted with white triangles). Similarly, 11 other screens can be generated for each of the higher levels.

2.3 Pressure, Wind and Air density profiles

Temperature [K], water vapor mixing ratio [kg H₂O/kg air], topography (ground surface altitudes) [m], wind direction [degree], wind speed [m/s], CO mixing ratio [mole CO/ mole air] and SO₂ mixing ratio [mole SO₂/ mole air] profiles were extracted from the GEM-MACH model. Depending on the approach (AFT and VP described in sections 2.2.1 and 2.2.2) the extracted data result in a single screen or multiple screens for each flight (e.g flight 8, 2 hrs flight time), and for every parameter (e.g. temperature, CO mixing ratio). These screens are then either directly analyzed or used to generate secondary screens to be analyzed with TERRA for emissions estimation.

2.3.1 Logarithmic Pressure Profiles

Air density can be determined based on the extracted meteorological data (e.g. temperature, water vapor mixing ratio) at each level. Pressure levels were not determined in the extraction program and therefore estimations had to be made. To achieve this, the hourly average recorded air pressure for August and September 2013, for flights 8 and 18 respectively, at the weather station “AB FORT MCMURRAY A ALBERTA” was used [10]. The hourly average air pressures measured during the flight time at the elevation of $z_{ref} = 369.10$ m were, $P(z_{ref}) = 96.4$ kPa for August 20 (flight 8) and $P(z_{ref}) = 96.5$ kPa for September 3 (flight 18) 2013; To determine surface pressure P_{surf} , $P(z_{ref})$ was substituted into the following exponential profile,

$$P(z) = P_{surf} \exp(-(z)/(H_p)) \quad (2.1)$$

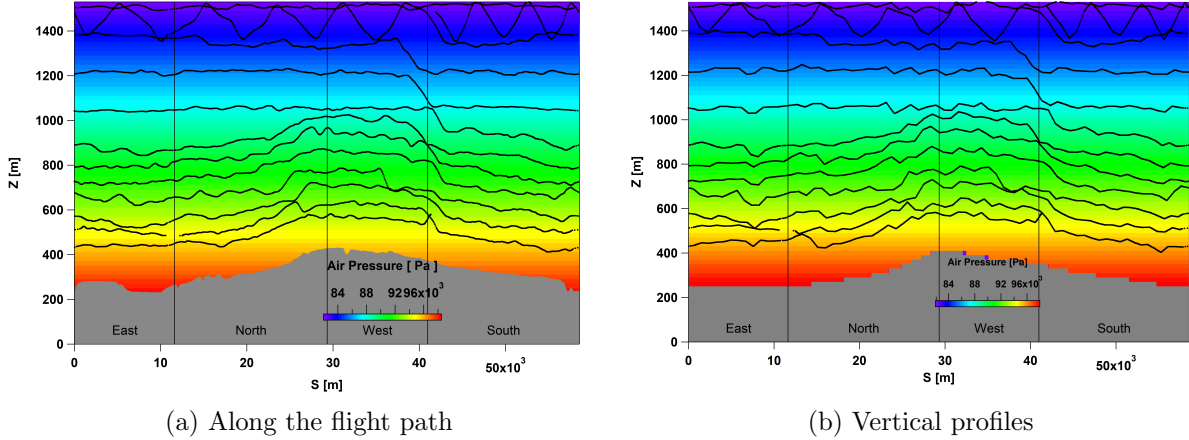


Figure 2.8: Air pressure screen constructed for flight 8, using recorded values at the “AB FORT MCMURRAY A ALBERTA” weather station , at the elevation of $z = 369.10$ m [10], and utilizing Equation 2.1 [24]. Note the difference in surface topography for (a) and (b).

where z is the height above the ground and $H_p = 7.29$ km, is the scale height [24]. After the surface pressure P_{surf} was determined for each horizontal location s along the flight path, the same profile (Equation 2.1) is used to generate vertical pressure profiles with one measured point at $z_{ref} = 369.10$ m. Next, these vertical profiles are used to construct an air pressure screen, Figure 2.8. There was a difference in representing the surface topography for the two approaches (a) AFT (section 2.2.1) and (b) VP (section 2.2.2). For (a), surface topography profiles that were measured during flights 8 and 18 (reported at a frequency of 1 Hz) were used to mimic aircraft-based measurements. For (b), surface topography was extracted from the model at a frequency of 0.1 Hz and then was interpolated in time and space to match 1 Hz. This resulted in a slight difference in the pressure profiles near the ground surface, with the negligible overall difference of 0.5%.

2.3.2 Temperature, Water Vapor Mixing Ratio and Air density

With temperature and water vapor mixing ratio profiles extracted from GEM-MACH and the air pressure profiles estimated as explained above, air-density

can be determined as follows

$$\rho_{air}(z) = \frac{P(z)}{RT(z)(1 + 0.6\chi_{H_2O}(z))} \quad (2.2)$$

where $P(z)$ is the air pressure, $R = 287.1 \text{ Jkg}^{-1}\text{K}^{-1}$, $T(z)$ is the temperature and $\chi_{H_2O}(z)$ is the water vapor mixing ratio [12].

Originally, this was the main method for estimating the air density in our analysis. Later on, the model air density profiles were also extracted to investigate the sensitivity of our results to air density estimations based on meteorological data (as described above).

2.3.3 Easterly and Northerly Wind Screens

Using the extracted wind speed and direction profiles from the GEM-MACH model, wind speeds are separated into easterly U_E and northerly U_N components [12].

$$U_E = M \sin(\alpha) \quad (2.3)$$

$$U_N = M \cos(\alpha) \quad (2.4)$$

where M is the wind speed in m/s and α is wind direction in degrees [24].

When simulating the aircraft-based measurements (section 2.2.1) no data are extracted below the lowest flight level. This is the case for all profiles including wind speeds. Thus, extrapolation is needed for elevations below the lowest flight level to the ground surface; similar to the steps shown in Figure 2.5. Wind speeds were extrapolated to the ground below the lowest flight level to the surface level (z_g), using a least-squares fit of U to $\ln(z)$ as

$$U(z) = \frac{u_*}{k} \ln(z - z_g - d) + f \quad (2.5)$$

where z is the height above the ground, $k = 0.4$, displacement height is $d = 6\text{m}$ [12]. Terms that are not z dependent are grouped in the fit parameter f [11]. Gordon et al., estimated f based on meteorological measurements

during each flight (e.g. $f = -2.64 \text{ m/s}$ for the flight 8) [12]. At each point along the horizontal flight path, the value of the wind speed at the lowest flight path was substituted in Equation 2.5 as $U(z)$ to calculate u_* ; then these values were used to calculate the vertical wind speed profiles in the surface layer.

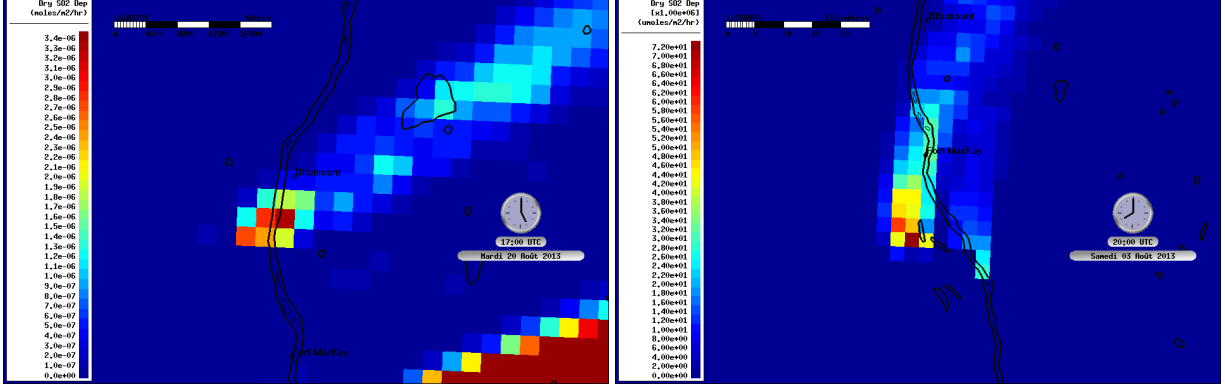
2.4 Surface Concentrations and Deposition

TERRA estimates surface deposition rates within the control volume by assuming a constant surface concentration equal to the average surface species mixing ratio along the box walls, $\chi_{surf,C} = \bar{\chi}_{surf,C}(s)$. This is then substituted in Equation 1.7 with deposition velocity $V_D = 10 \text{ mm/s}$ for SO_2 and $\simeq 0$ for CO [12] [27].

To test this assumption, surface species concentrations (CO and SO_2) were extracted from the GEM-MACH model for flight 8 on 20 August and flight 18 on 3 September, for two consecutive hours during the flight times. Surface concentrations for the first hour were subtracted by the second hour to estimate the deposition hourly average surface deposition rate, for each flight. Figure 2.9 shows a map of calculated deposition rate of SO_2 (with model resolution of 2.5 km) based on change in surface concentrations during the flight time, for each of flights 8 and 18.

2.5 Utilizing TERRA

Wind vectors, species concentrations and air density data are projected on corresponding screens, as described in previous sections. These 2D screens are comprised of four lateral walls of the control volume. By applying the convergence theorem to this control volume (box) as described in TERRA method (section 1.2), the air and species emissions fluxes and subsequently area source emission rates can be determined.



(a) Flight 8, 20 August 2013, 17-18 UTC

(b) Flight 18, 3 September 2013, 20-21 UTC

Figure 2.9: SO₂ deposition rates estimated based on surface concentrations extracted from GEM-MACH model for each flight.

Starting with the air mass flux estimation, the first term of Equation 1.1, the horizontal advective flux $E_{air,H}$, is calculated based on the wind and air density measurements along the box walls. The third term, $E_{air,M}$ which represents the increase in the air mass within the control volume, is calculated using Equation 1.4. The flight time (Δt) in Equation 1.4, is the time needed to extract enough data to generate a screen. When simulating the aircraft-based measurements, Δt is the entire box flight time (~ 2 hrs in case of flight 8), as opposed to the vertical profiles approach (section 2.2.2) where it is the time for flying once around the facility at each level. The vertical advective air flux $E_{air,V}$ is then estimated based on $E_{air,H}$ and $E_{air,M}$ from Equation 1.4.

Next, from the mass balance relation for compound C (Equation 1.5) compound mass fluxes can be estimated. Previous aircraft studies have shown that the advective fluxes dominate the change in the compound mass within the control volume, 85-95% for NO_x and CO [16] [22] and 95-99% for CH₄ and SO₂ [12]. Estimations of the advective fluxes along with surface deposition, $E_{C,VD}$, and changes in mass due to air densification, $E_{C,M}$, can account for over 99% of the total emissions. This assumption reduces Equation 1.5 to,

$$E_C = E_{C,H} + E_{C,V} + E_{C,VD} - E_{C,M} \quad (2.6)$$

where $E_{C,H}$ is the horizontal advective flux and $E_{C,V}$ is the vertical box top advective flux, both positive outwards. $E_{C,VD}$ is always positive since it represents the mass leaving the box through surface deposition. $E_{C,M}$ is positive for the increased (and negative for decreased) mass due to change in air density. $E_{C,H}$ is calculated based on the extracted species mixing ratio along the box walls and the horizontal advective air flux (Equation 1.6) and $E_{C,V}$ is calculated using Equation 1.8 based on the estimated box top species mixing ratio and vertical advective air flux. $E_{C,VD}$ is estimated based on the species surface mixing ratio and deposition rate extracted from GEM-MACH (see Figure 2.9) and using Equation 1.7, and $E_{C,M}$ is determined based on the estimated species mixing ratio within the control volume at each height and using Equation 1.9. After all these terms were determined, they are substituted in Equation 2.6 to determine the total species emission rate E_C .

On 20 August 2013, during flight 8, the aircraft started a box flight path at 16:31:24 UTC (10:31:24 local time) around the CNRL facility and completed the path approximately 2 hours later at 18:40:19 UTC (see Figure 2.1a). On 3 September 2013, during flight 18, the aircraft started another box flight path at 20:58:01 UTC (14:58:01 local time) around the Syncrude facility and completed the path approximately 2 hours later at 22:56:29 UTC (see Figure 2.1b). During each flight, the aircraft sampled meteorological and species concentrations and reported data at a frequency of 1 Hz along with aircraft state parameters (Lon, Lat, Height). The aircraft state parameters for flights 8 and 18 were then used to fly a virtual aircraft within the GEM-MACH model and simulate aircraft-based measurements. The data were extracted from the model output at a frequency of 0.1 Hz and interpolated in time and space to match the frequency of reported aircraft-based measurements. Depending on the approach, AFT (section 2.2.1) and VP (section 2.2.2), emission rates were estimated over approximately 2 hrs (box flight time) and for periods of approximately 10-15 min (flight time at each level), respectively. Emission rates estimated using either of the methods

were compared to each other and to the model input values (see Tables 2.1 and 2.2). The purpose of this comparison is three fold: 1) to investigate the sensitivity of the results on the temporal evolution of the system by assuming different steady state periods (10 min vs. 2 hrs), 2) testing and improving the downward extrapolation schemes used in TERRA, 3) investigating the performance of TERRA method in retrieving emissions using aircraft-based measurements, by comparing estimated emissions to emissions inventories input in the GEM-MACH model.

Chapter 3

Implementation and Results

3.1 Estimated Emission Rates: AFT Method

3.1.1 Air Density

The average hourly emissions estimated over approximately 2 hrs were made based on the data collected along the flight tracks, simulating aircraft-based measurements. Extrapolations were made to fill the gap below the lowest flight level (see Figure 2.5). Air pressure values recorded on 20 August and 3 September 2013 at the weather station “AB FORT MCMURRAY A ALBERTA” (near oil sands) were substituted in Equation 2.1 to generate pressure profiles along the walls of the box flights 8 and 18 around CNRL for August 20 and Syncrude for September 3 (Figures 3.1a and 3.2a)) [10]. Similar screens were generated for temperature and water vapor mixing ratio for the same day, based on extracted values along the flight tracks during flights 8 and 18 (see Figures 3.1b, 3.1c, 3.2b and 3.2c). Next, pressure, temperature and water vapor mixing ratio screens were substituted in Equation 2.2 to generate an air density screen (Figures 3.1d and 3.2d). This is how air density screens are generated in TERRA, based on measured/extracted meteorological data.

Air density profiles were also extracted directly from the GEM-MACH model and aircraft-based measurements of air density were simulated. This was done to evaluate air density estimations based on meteorological data.

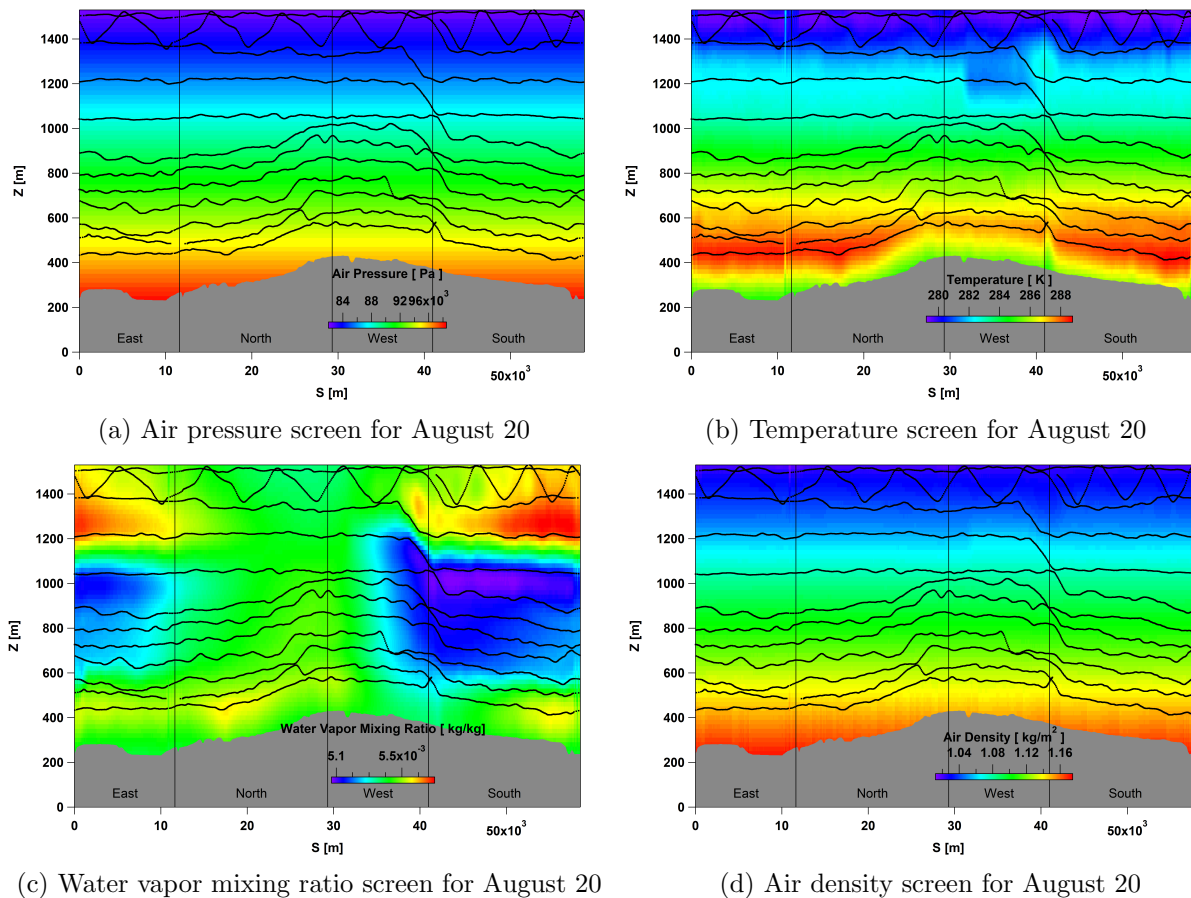
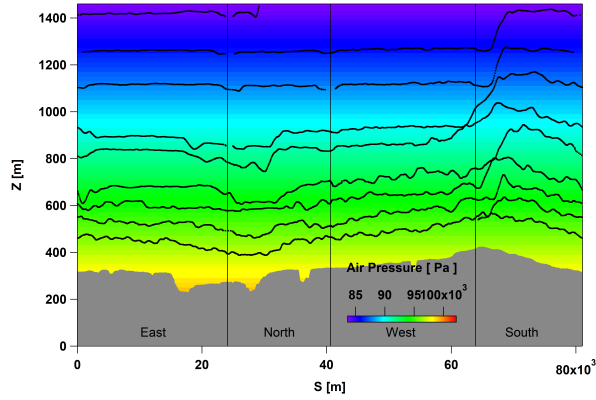
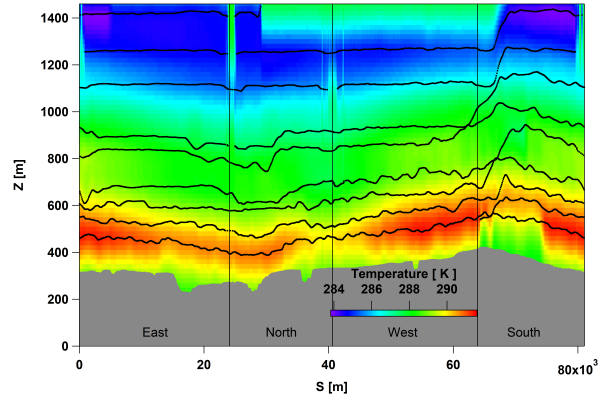


Figure 3.1: Pressure, temperature, water vapor mixing ratio and air density screens were constructed for 20 August 2013 around the CNRL facility, based on extracted values along the flight tracks (AFT) during flight 8 and profiles described by Equations 2.1 and 2.2. Flight 8 tracks are superimposed with black dots and the box lateral walls are labeled with geographical directions East, North, West and South.

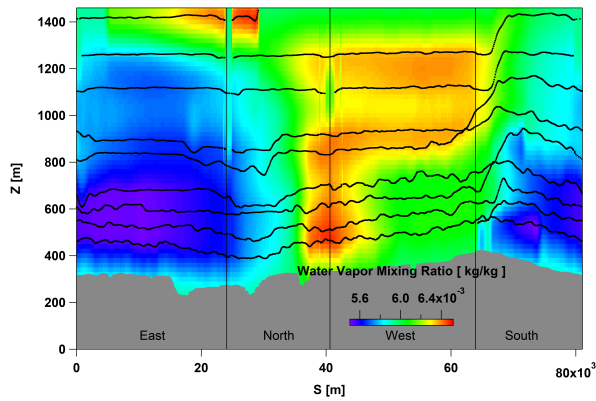
For all AFT cases, air density screens were extrapolated linearly below the lowest flight level to the ground. Figure 3.3 shows the AFT extracted air density screens for flights 8 and 18. Mean air density calculated with TERRA is very close to the mean value extracted from the model and only differs by about 1.1% for the case of flight 8. This results in 15% difference in the estimated air flux and 1.6% difference in the total estimated compound (e.g. SO_2) emission rate. For flight 18, the mean deviation in TERRA estimated air densities from model extracted values is about 2.7%, which results in 4.2% deviation in air flux and 2.3% deviation in total estimated species emission rate.



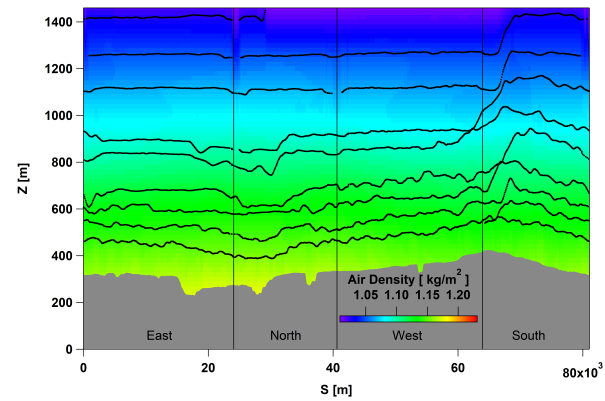
(a) Air pressure screen for 3 September



(b) Temperature screen for 3 September

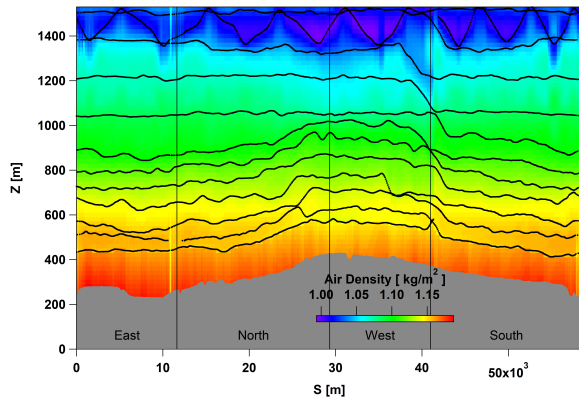


(c) Water vapor mixing ratio screen for 3 September

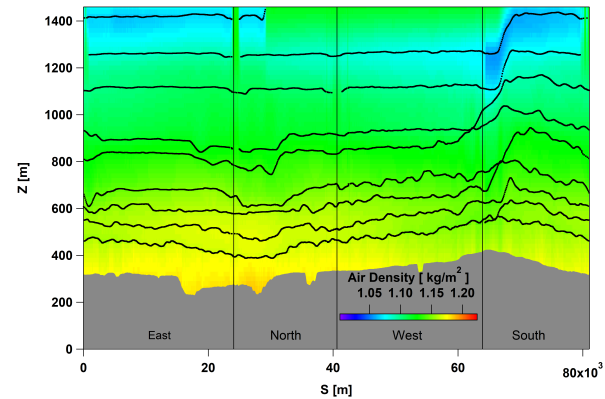


(d) Air density screen for 3 September

Figure 3.2: Pressure, temperature, water vapor mixing ratio and air density screens were constructed for 3 September 2013 around the Syncrude facility, based on extracted values along the flight tracks (AFT) during flight 18 and profiles described by Equations 2.1 and 2.2. Flight 18 tracks are superimposed with black dots.



(a) Air density screen for August 20



(b) Air density screen for September 3

Figure 3.3: Screens constructed based on the AFT extracted air density values. Flights 8 and 18 tracks are superimposed with black dots and the box lateral walls are labeled with geographical directions East, North, West and South.

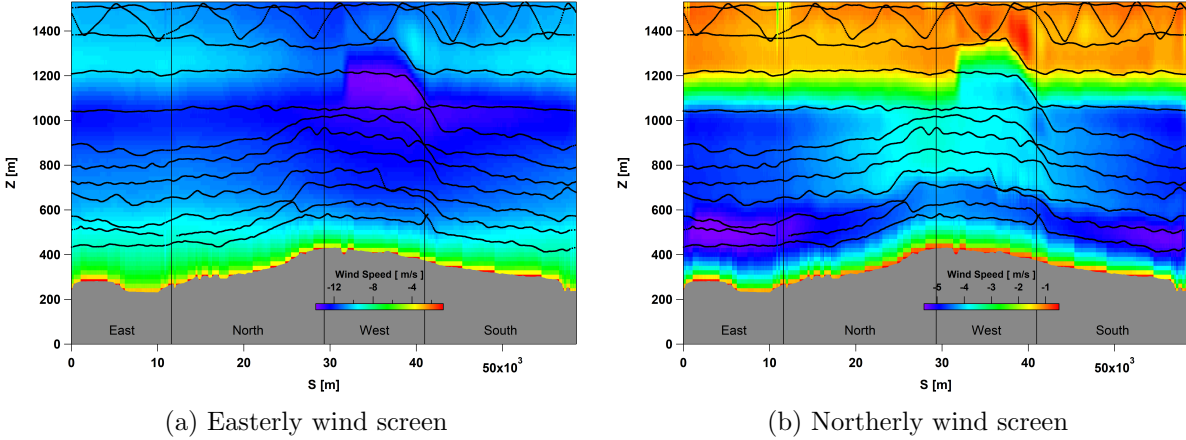


Figure 3.4: Easterly and northerly wind speed screens were created based on wind vectors extracted along the flight tracks (AFT) for flight 8 on August 20 2013. Flight 8 tracks are superimposed with black dots and the box lateral walls are labeled with geographical directions East, North, West and South.

3.1.2 Wind

Wind speed (M) and direction (α) screens were constructed based on the extracted wind vectors along the flight tracks (AFT). Wind speeds were separated into easterly U_E and northerly U_N components using Equations 2.3 and 2.4 respectively, and the corresponding screens were constructed. Wind screens were then filled with extrapolation below the lowest flight level using Equation 2.5. Figures 3.4 and 3.5 show easterly and northerly wind profiles along the lateral walls of the box flights 8 and 18 respectively.

3.1.3 Air Flux

Air density (AFT extracted, see Figure 3.3), easterly and northerly wind screens were used to calculate the horizontal advective air flux using Equations 1.2 and 1.3.

For flight 8, it can be seen from Figure 3.6a that the main air flux enters the box from the west wall and leaves the box through the east wall. Therefore, emissions from a source within the facility inside the box, would most likely be picked up by the incoming air flux and carried to the east wall where it exits the box. Thus, the east wall is where the apparent plume is expected

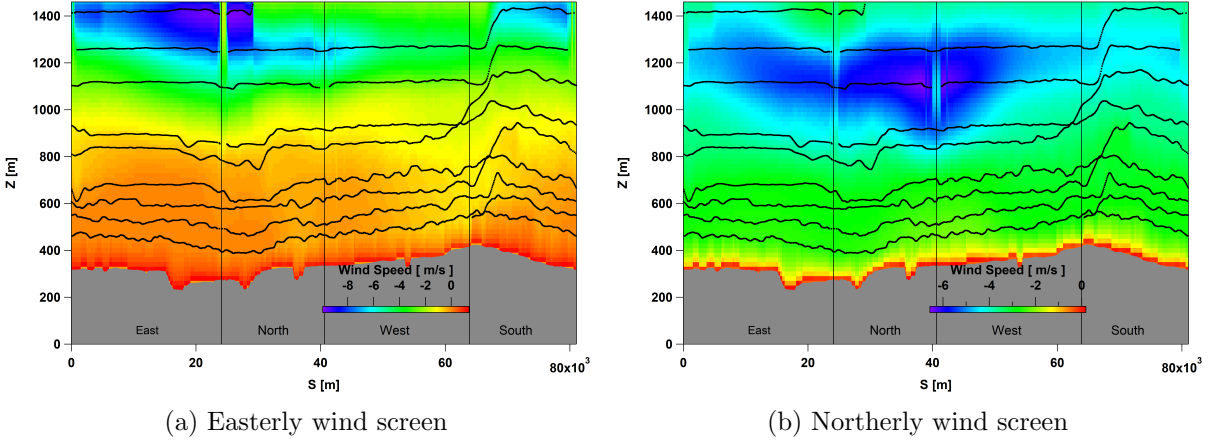
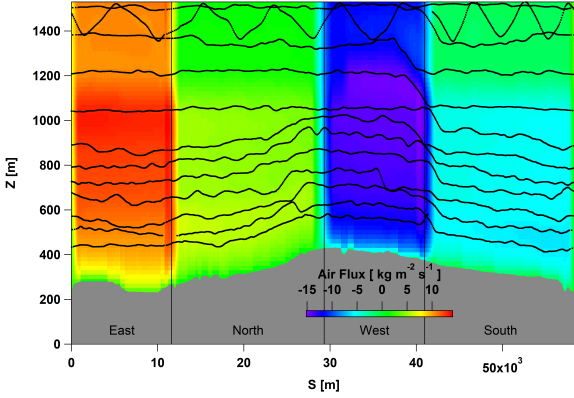


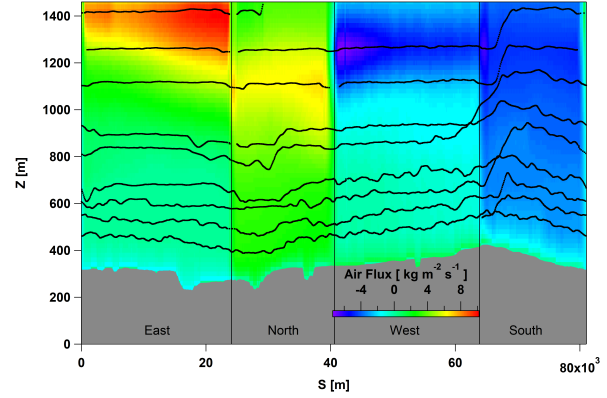
Figure 3.5: Easterly and northerly wind speed screens were created based on wind vectors extracted along the flight tracks (AFT) for flight 18 on 3 September 2013. Flight 18 tracks are superimposed with black dots.

to be observed on the screen, which turns out to be the case (Figure 3.7). Similarly for flight 18, it can be seen from Figure 3.6b that the main air flux enters the box from the west and south walls and leaves the box through the east and north walls. Therefore, emissions from a source within the facility inside the box, would most likely be picked up by the incoming air flux and carried to the east and north walls where it exits the box. Thus, the east and north walls are where the apparent plume is expected to be observed on the screen (Figure 3.8).

The total horizontal advective air flux ($E_{air,H} = E_{air,H,out} - E_{air,H,in}$), over the ~ 2 hrs flight time, was estimated to be $E_{air,H} = -2.22 \times 10^{10}$ kg/hr or -22.2 Mt/hr (mega tonnes per hour) for flight 8 and $E_{air,H} = +1.27 \times 10^{11}$ kg/hr or 127 Mt/hr for flight 18. The negative (positive) sign indicates that the net horizontal advective air flux is into (out of) the box. This provides assumptions for estimating the vertical advective air flux through the box top. Calculating the vertical air flux requires the calculated change in air density, $E_{air,M}$. Using Equation 1.4, the total $E_{air,M}$ was estimated to be -5.9×10^8 kg/hr for flight 8 and -1.8×10^9 kg/hr for flight 18. The negative sign represents a decrease in air mass due to reduced air density. The advective vertical air flux was then estimated by substituting the estimated values of



(a) Flight 8 $E_{air,H}$ screen



(b) Flight 18 $E_{air,H}$ screen

Figure 3.6: Horizontal advective air flux $E_{air,H}$ screen (positive out of the box), generated based on air density and wind speed screens. Flights 8 (a) and 18 (b) tracks are superimposed with black dots and the box lateral walls are labeled with geographical directions East, North, West and South. (a) the main air flux enters the box from the West wall and exits from the East wall. Therefore, the East wall is where the apparent plume on the screen from the emission source within the box, is expected to be found. (b) the main air flux enters the box from the west and south walls and exits from the east and north wall. East and north walls are where the apparent plume is expected to be found.

$E_{air,H}$ and $E_{air,M}$ in Equation 1.1 to be $E_{air,V} = 2.16 \times 10^{10}$ kg/hr for flight 8 and -1.29×10^{11} kg/hr for flight 18.

3.1.4 Compound Mixing Ratio

Concentration screens were generated based on the extracted mixing ratios of SO_2 and CO along the flight tracks, and by kriging interpolation between the extracted points and using TERRA extrapolation methods below the lowest flight level (Figures 3.7 and 3.8). As mentioned before, the outgoing lateral advective air flux, results in both SO_2 and CO plumes appearing on the east wall for flight 8 (Figure 3.7) and on the east and north walls for flight 18 (Figure 3.8).

3.1.5 Advective Fluxes

With air flux and compound mixing ratio screens constructed, the compound horizontal advective flux $E_{C,H}$ can be estimated using Equation 1.6 and the

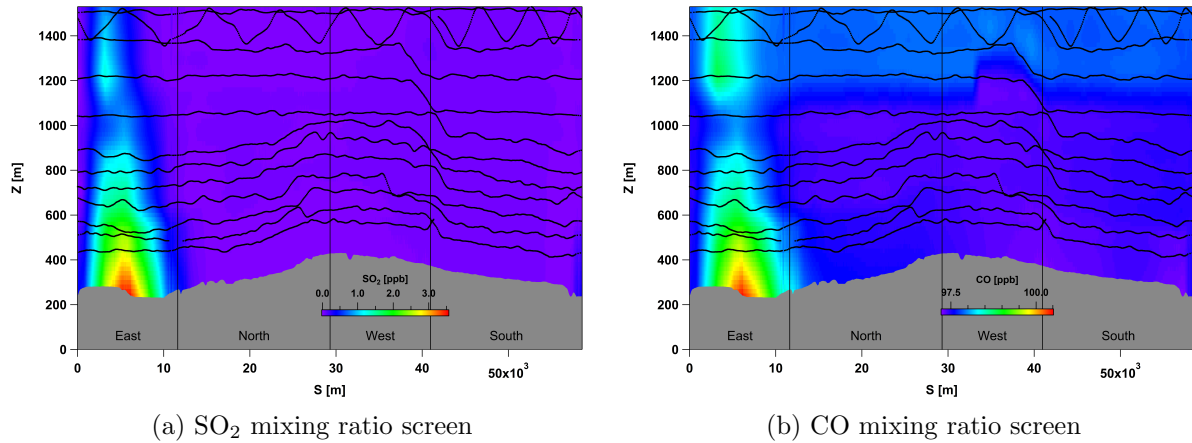


Figure 3.7: Mixing ratio screens constructed based on measurements along the flight 8 tracks on August 20 2013, extrapolated below the lowest flight level (extrapolations using the Linear fit method are shown as examples). Flight 8 tracks are superimposed with black dots and the box lateral walls are labeled with geographical directions East, North, West and South. In both cases the plume appears on the East wall.

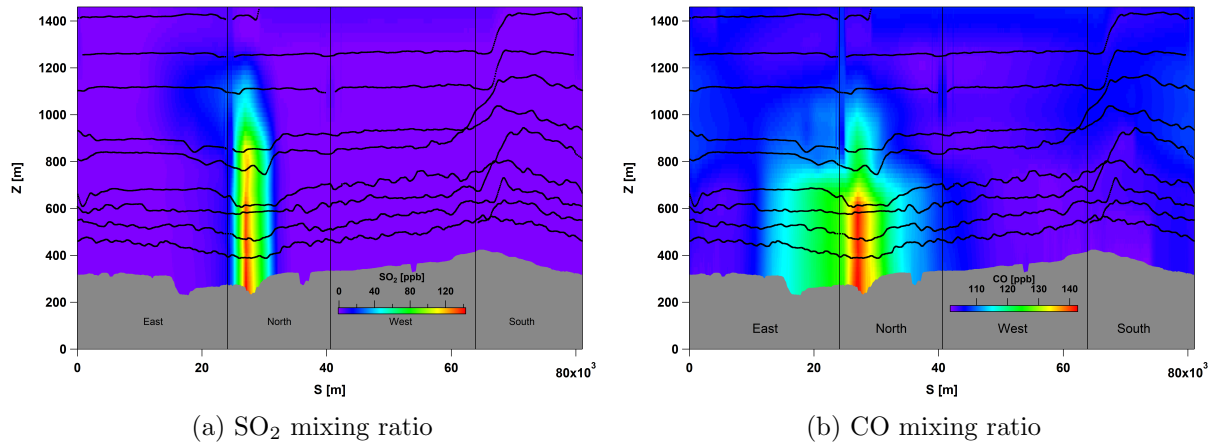


Figure 3.8: Mixing ratio screens constructed based on measurements along the flight 18 tracks on 3 September 2013, extrapolated below the lowest flight level (extrapolations using the Linear fit method are shown as examples). Flight 18 tracks are superimposed with black dots and the box lateral walls are labeled with geographical directions East, North, West and South. In both cases the plume appears on the North wall.

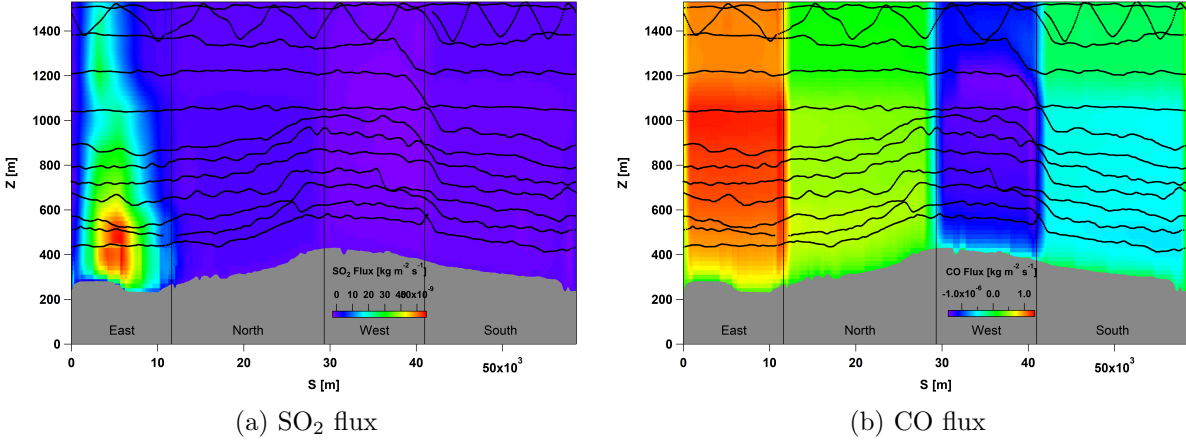


Figure 3.9: Compound horizontal advective mass flux through lateral walls of the box. Screens were constructed based on compound mixing ratio measurements along the flight 8 tracks on 20 August 2013 and the estimated horizontal advective air flux. Flight 8 tracks are superimposed with black dots and the box lateral walls are labeled with geographical directions East, North, West and South.

corresponding screens generated (Figures 3.9 and 3.10). For flight 8, the SO_2 flux is greatest on the east wall (Figure 3.9a). This is due to high concentrations of SO_2 at the location of the plume on the east wall and near zero concentrations elsewhere (Figure 3.7a). However, due to high concentrations of CO (97-100 ppb) along all four lateral walls of the box (Figure 3.7b), CO flux is high wherever the air flux is strong (Figure 3.9b). The same is true for flight 18 with the SO_2 plume on the north wall (Figure 3.10).

3.1.6 Surface Deposition

Surface deposition rates ($E_{C,VD}$) were estimated in two ways as described in section 2.4: 1) TERRA estimation by making assumptions about surface concentrations and utilizing Equations 1.7 and 2) based on model extracted surface mixing ratios and their temporal changes. TERRA estimated deposition rates range between 6.26 - 9.18 kg/hr for flight 8 and 295.11 - 405.08 kg/hr for flight 18, depending on the surface layer extrapolation method used. The hourly average $E_{C,VD}$ based on model extracted values for SO_2 was estimated to be 5.75 kg/hr and 285.5 kg/hr during flights 8 and 18, respectively.

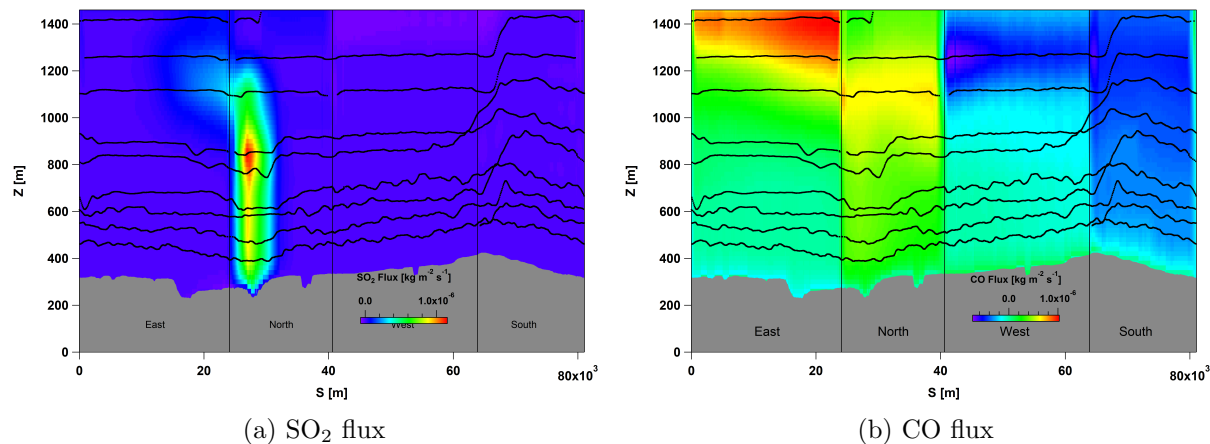


Figure 3.10: Compound horizontal advective mass flux through lateral walls of the box. Screens were constructed based on compound mixing ratio measurements along the flight 18 tracks on 3 September 2013 and the estimated horizontal advective air flux. Flight 18 tracks are superimposed with black dots.

TERRA estimates are higher than model extracted values by 8.9 - 59.6% for flight 8 and by 3.4 - 41.9% for flight 18. CO depositions were negligible ($\simeq 0$ kg/hr) for both cases.

3.1.7 Emissions

$E_{C,M}$ and $E_{C,V}$ were calculated using Equations 1.9 and 1.10, respectively. The total hourly $E_{C,V}$, estimated over the ~ 2 hrs flight time, was 4.68 kg/hr for SO_2 and 2043.84 kg/hr for CO during flight 8. Estimates during flight 18 were -1079.88 kg/hr for SO_2 and -13249.7 kg/hr for CO. Note that the CO advective vertical flux is about 400 times that of SO_2 for flight 8. This is due to near zero levels of SO_2 and high CO concentrations (97 ppb) at the top of the box. These parameters were then substituted in Equation 2.6 to estimate the total emission rate E_C . Different emission levels were estimated for each case of extrapolation below the lowest flight, for SO_2 and CO. Results are presented in Tables 3.1, 3.2, 3.3 and 3.4 and are plotted as dashed lines in Figures 3.21, 3.22, 3.23 and 3.24.

Table 3.1: Extracted meteorological and concentration profiles along the flight 8 tracks on 20 August 2013, were used to estimate SO₂ emission rates. Four different extrapolation methods, for heights below the lowest flight level to the surface, were examined.

Extrapolation Method	$E_{C,H}$ [kg/hr]	$E_{C,M}$ [kg/hr]	E_C [kg/hr]
Zero to Constant	782.45	-0.20	787.33
Constant	859.68	-0.31	864.66
Linear Fit	900.53	-0.36	905.56
Exponential Fit	903.14	-0.35	908.17
		$E_{C,Inventory}$	513.73

Table 3.2: Extracted meteorological and concentration profiles along the flight 8 tracks on 20 August 2013, were used to estimate CO emission rates. Four different extrapolation methods, for heights below the lowest flight level to the surface, were examined.

Extrapolation Method	$E_{C,H}$ [kg/hr]	$E_{C,M}$ [kg/hr]	E_C [kg/hr]
Zero (background min) to Constant	-1751.96	-56.31	348.19
Constant	-1717.01	-56.35	383.19
Linear Fit	-1698.71	-56.37	401.50
Exponential Fit	-1684.53	-151.25	415.70
		$E_{C,Inventory}$	246.00

3.2 Estimated Emission Rates: VP Method

During flight 8 on 20 August 2013, the aircraft flew along a horizontal rectangular path at about 12 consecutive altitude levels around the CNRL facility (Figure 2.2). On 3 September 2013 and during flight 18, the aircraft flew a similar path around Syncrude at about 8 consecutive levels. It took the aircraft about 10 min for flight 8 and about 15 min for flight 18 to travel once around the facility at each level. Model data were extracted as vertical profiles along the aircraft’s path at each time-stamp (Figure 2.6). Vertical profiles extracted during the flight around the facility at each level, generated enough data for constructing a screen for each parameter (e.g. compound mixing ratio, wind) as described in section 2.2.2. Since the time lag between the first and the last extracted vertical profile for constructing each screen is the flight time at each level, the steady state assumption of the system is

Table 3.3: Extracted meteorological and concentration profiles along the flight 18 tracks on 3 September 2013, were used to estimate SO₂ emission rates. Four different extrapolation methods, for heights below the lowest flight level to the surface, were examined.

Extrapolation Method	$E_{C,H}$ [kg/hr]	$E_{C,M}$ [kg/hr]	E_C [kg/hr]
Zero to Constant	14704.5	-22.8	13932.9
Constant	15084.2	-31.1	14320.9
Linear Fit	15175.8	-31.7	14413.2
Exponential Fit	15489.7	-35.9	14731.3
		$E_{C,Inventory}$	9094.36

Table 3.4: Extracted meteorological and concentration profiles along the flight 18 tracks on 3 September 2013, were used to estimate CO emission rates. Four different extrapolation methods, for heights below the lowest flight level to the surface, were examined.

Extrapolation Method	$E_{C,H}$ [kg/hr]	$E_{C,M}$ [kg/hr]	E_C [kg/hr]
Zero (background min) to Constant	14562.5	-186.36	1499.13
Constant	14608.4	-188.98	1547.65
Linear Fit	14622.4	-189.07	1561.77
Exponential Fit	14677.4	-189.91	1617.63
		$E_{C,Inventory}$	1192.43

made only for about 10-15 minutes, as opposed to steady state assumption over approximately 2 hours with the AFT approach (section 3.1.1). This provides a method to assess the assumptions about the temporal evolution of the system. The other advantage of this approach is that the vertical profiles are extracted for the heights from the surface to altitudes above the top of the box. This removes the need for extrapolation below the lowest flight level and the surface (section 1.2.2), and can be utilized for assessing the uncertainties arising from mixing ratio screen extrapolations in emissions estimation.

3.2.1 Air Density, Wind and Air Flux

Pressure screens were created for August 20 and September 3 (for flight time period) based on measured values, in an approach similar to that of section 3.1.1. Using the extracted meteorological vertical profiles during the flight at each level (\sim 10-15 min), screens were constructed for each parameter: tem-

perature, water vapor mixing ratio and wind; and the air density screens were constructed, as described in section 2.3. Air density profiles were also directly extracted from the GEM-MACH model to be compared with the TERRA estimated profiles based on meteorological data. TERRA estimations of air density result in a deviation in air flux calculations when compared to estimations made based on extracted model air densities of about 7% for flight 8 and about 2% for flight 18.

Wind speeds were separated into east and north winds, and air flux screens were generated based on VP extracted model wind and air density values (Figures 3.11 and 3.12). It can be seen from Figure 3.11 (flight 8) that the horizontal advective flux leaving the box through the east wall is decreasing with time, while the air flux entering the box through the west wall is decreasing at a slower rate. This results in a change in the net horizontal air flux from positive (leaving the box) to negative (entering the box) and consequently a negative to positive change in the net vertical advective air flux through the box top (mass conservation). Results are presented in Table 3.5. It can also be seen from the table that the net air flux through the lateral sides changes from positive (out of the box) to negative and back to positive, over time. While the air densification rate remains roughly the same, the mass conservation of air within the box (Equation 1.1) requires the vertical flux through the box top to change opposite to the horizontal air flux. Results for flight 18 are also presented in Table 3.6. The average net air flux through the lateral walls is into the box (negative) and equal to $\bar{E}_{air,H} = -12.6$ Mt/hr for flight 8 and diverging (positive) and equal to $\bar{E}_{air,H} = 51.2$ Mt/hr for flight 18. The average net vertical flux is positive and equal to $\bar{E}_{air,V} = 12.0$ Mt/hr for flight 8 and negative and equal to $\bar{E}_{air,V} = -54.1$ Mt/hr for flight 18. These could be compared to the estimations over the box flight time (~ 2 hrs) of section 3.1.3, $E_{air,H} = -22.2$ Mt/hr and $E_{air,V} = 21.6$ Mt/hr for flight 8 and $E_{air,H} = 127$ Mt/hr and $E_{air,V} = -129$ Mt/hr for flight 18. While signs (into or out of the box) are consistent, estimates

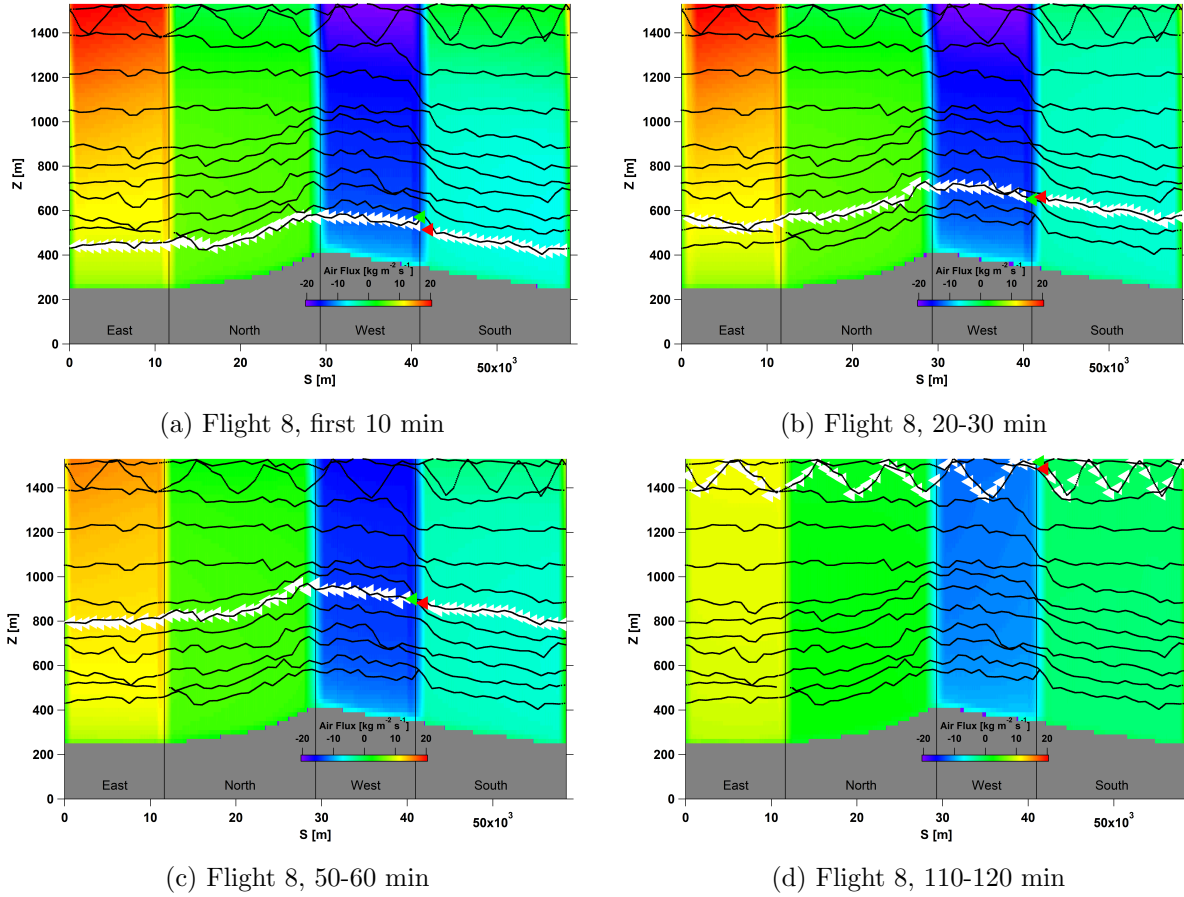
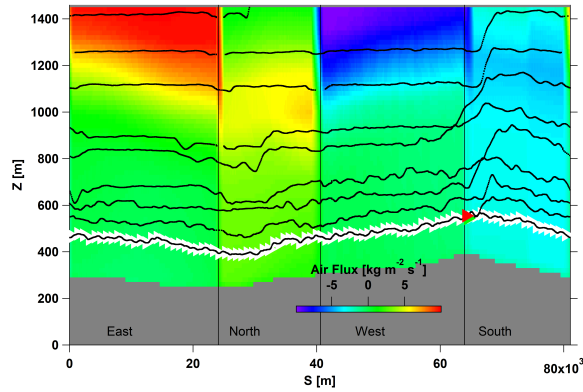
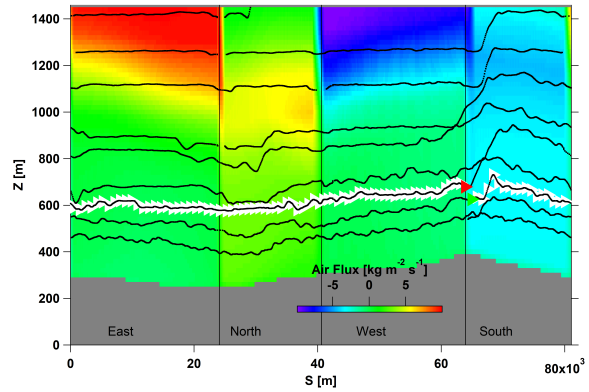


Figure 3.11: Four of the twelve horizontal advective air flux screens, generated for flight 8. The location and direction (to the left) of the aircraft along the flight tracks is shown with white triangles. The green triangle marks the starting point at each level. The path terminates at the red triangle. At each level, the aircraft travels around the facility, from the green triangle to the red, in about 10 min. Vertical profiles extracted along the flight track, were used to construct screens for each 10 min. Therefore, the temporal evolution of the system can be studied. Note how the horizontal advective air flux is changing with time (more visible on East and West walls).

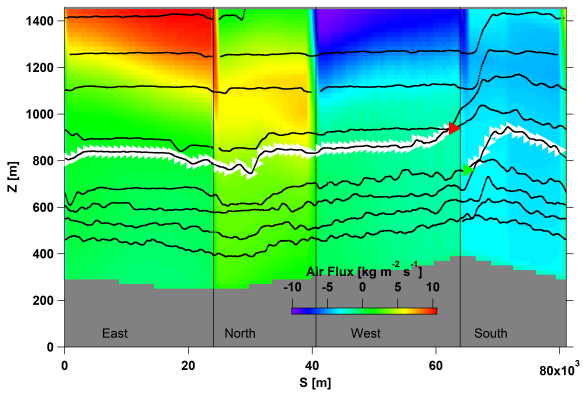
over the ~ 2 hrs box flight time, are about two times higher than the average of estimates over the consecutive ~ 10 -15 min periods of the flight. This is the first indication of the sensitivity of the results on the assumptions made about the steady state time of the system (2 hrs vs. 10-15 min).



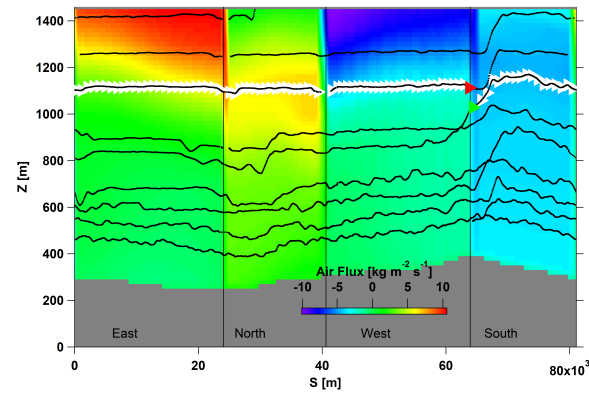
(a) Flight 18, first 15 min



(b) Flight 18, 30-45 min



(c) Flight 18, 60-75 min



(d) Flight 18, 90-105 min

Figure 3.12: Four of the eight horizontal advective air flux screens, generated for flight 18. The location and direction (to the right) of the aircraft along the flight tracks is shown with white triangles. The green triangle marks the starting point at each level. The path terminates at the red triangle. At each level, the aircraft travels around the facility, from the green triangle to the red, in about 15 min. Vertical profiles extracted along the flight track, comprise screens for each 15 min. Therefore, the temporal evolution of the system can be studied.

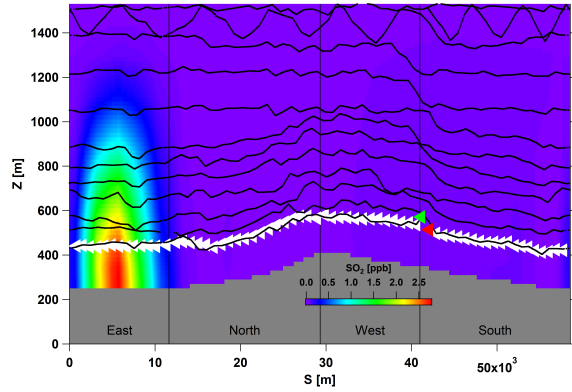
Table 3.5: Advective air fluxes through the lateral sides and the top of the box and the rate of air densification, were estimated for periods of ~ 10 min during flight 8. Estimations were made based on the vertical profiles extracted from the GEM-MACH model (section 2.2.2). The average net air flux through the lateral walls is into the box (negative) and the average net vertical flux is out of the box (positive).

Flight 8: 8/20/2013 (UTC)	$E_{air,H}$ [Mt/hr]	$E_{air,M}$ [Mt/hr]	$E_{air,V}$ [Mt/hr]
16:31:24 - 16:42:27	10.2	0.05	-10.2
16:42:27 - 16:52:57	10.6	-1.20	-11.8
16:52:57 - 17:03:49	-22.7	-1.85	20.9
17:03:49 - 17:14:41	-18.9	-0.01	18.9
17:14:41 - 17:25:41	-18.5	-0.04	18.5
17:25:41 - 17:36:36	-17.5	-0.004	15.2
17:36:36 - 17:47:27	-18.5	-0.01	18.5
17:47:27 - 17:58:19	-17.3	-3.45	13.8
17:58:19 - 18:09:00	-94.7	-0.62	94.0
18:09:00 - 18:19:27	13.4	0.09	-13.4
18:19:27 - 18:29:59	12.7	-0.09	-15.6
18:29:59 - 18:40:19	10.2	-0.08	-10.3
Average	-12.6	-0.60	12.0

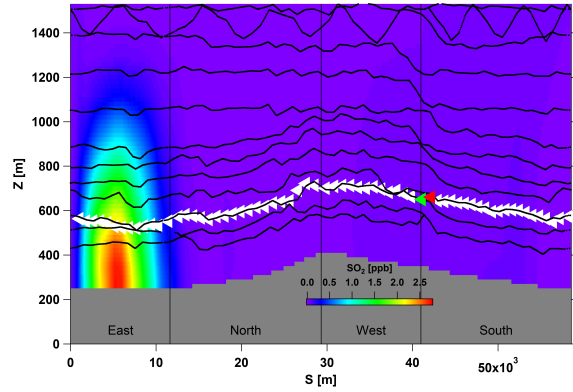
3.2.2 Compound Mixing Ratio, Surface Deposition and Emission Rates

Similarly, compound mixing ratio screens were constructed for each 10-15 min segment of the flight for SO_2 (Figures 3.13 and 3.15) and CO (Figures 3.14 and 3.16). Studying the twelve and the eight consecutive screens of flights 8 and 18 respectively, each corresponding to a 10-15 min segment of the box flight, the temporal evolution of the system can be seen. In the case of flight 8, the center of the plume for both SO_2 and CO, is rising and diluting with time. Two other interesting features can be seen in CO mixing ratio screens (Figure 3.14): 1) development of another weak plume on the South wall near the surface and 2) change in CO background levels.

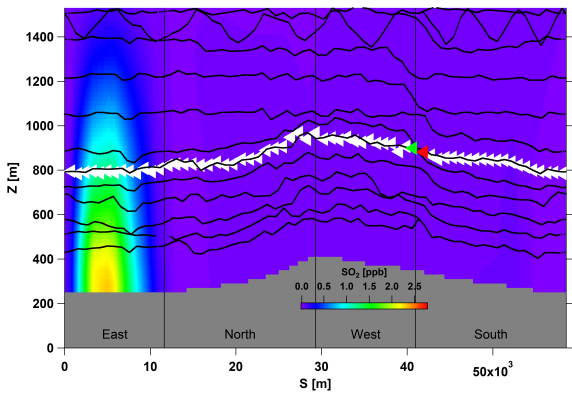
A total of twelve sets of screens were generated and therefore twelve sets of emission rate estimations were made for flight 8. Similar calculations were made for the eight sets of screens of flight 18. Four out of twelve generated SO_2 flux screens, corresponding to four different ~ 10 min segments of flight 8, are shown in Figure 3.17. It can be seen from Figure 3.17 that the SO_2 flux is decreasing with time. Similar screens were created for CO horizontal



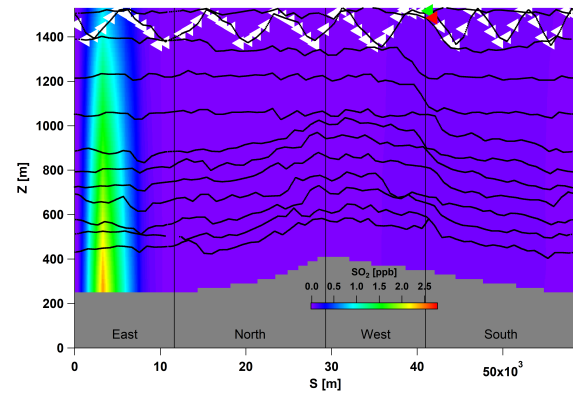
(a) Flight 8, first 10 min



(b) Flight 8, 20-30 min

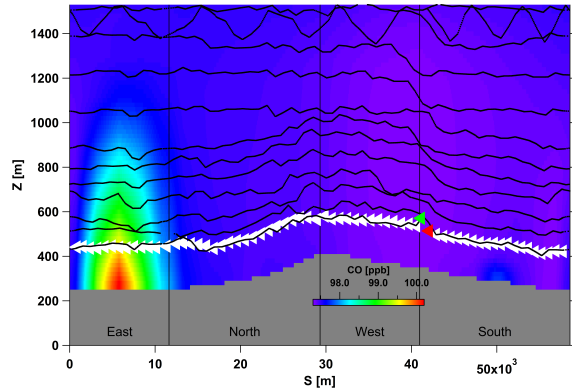


(c) Flight 8, 50-60 min

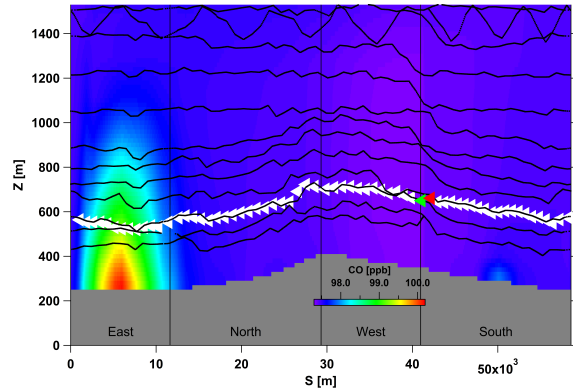


(d) Flight 8, 110-120 min

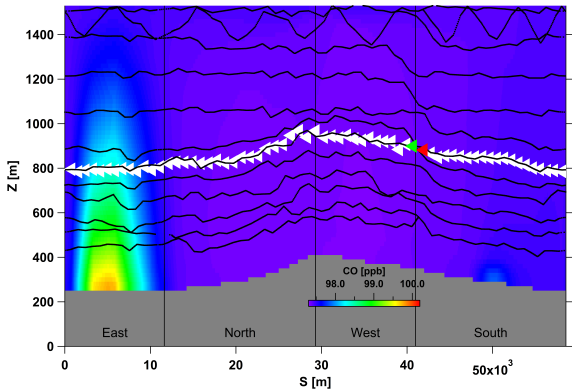
Figure 3.13: Four of the twelve SO_2 concentration screens, generated for flight 8. The location and direction (to the left) of the aircraft along the flight tracks is shown with white triangles. The green triangle marks the starting point at each level. The path terminates at the red triangle. At each level, the aircraft travels around the facility, from the green triangle to the red, in about 10 min. Vertical profiles extracted along the flight track, were used to construct screens for each 10 min. Therefore, the temporal evolution of the system can be studied, a rising and diluting plume center in this case.



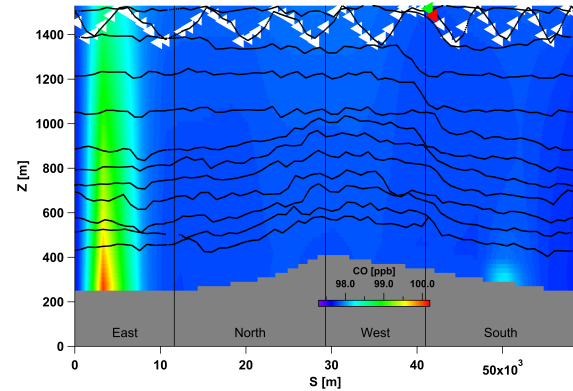
(a) Flight 8, first 10 min



(b) Flight 8, 20-30 min

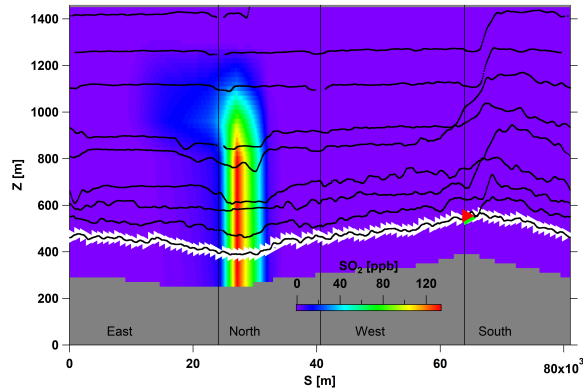


(c) Flight 8, 50-60 min

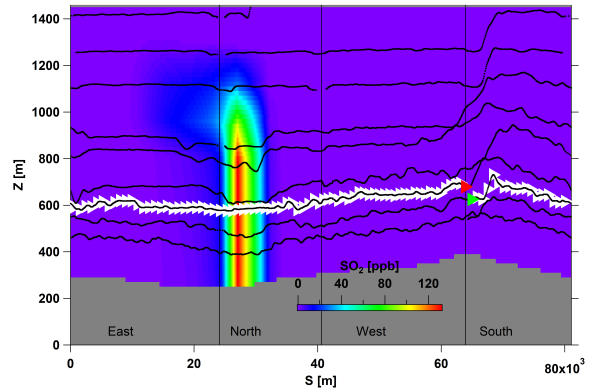


(d) Flight 8, 110-120 min

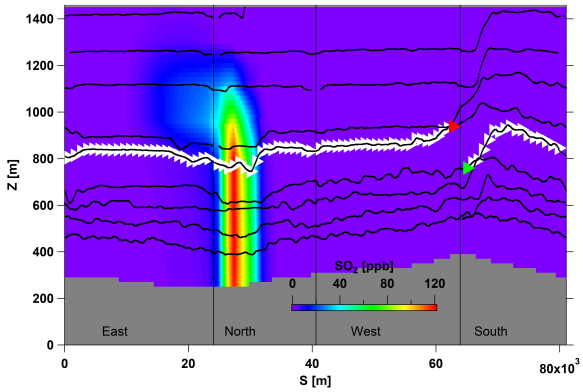
Figure 3.14: Four of the twelve CO concentration screens, generated for flight 8. The location and direction (to the left) of the aircraft along the flight tracks is shown with white triangles. The green triangle marks the starting point at each level. The path terminates at the red triangle. At each level, the aircraft travels around the facility, from the green triangle to the red, in about 10 min. Vertical profiles extracted along the flight track, were used to construct screens for each 10 min. Therefore, the temporal evolution of the system can be studied, a rising and diluting plume center in this case. Note the weak plume developing on the South wall near the surface. A change in background levels of CO can also be seen.



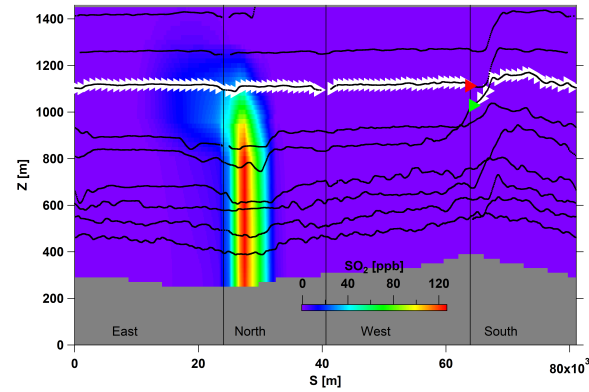
(a) Flight 18, first 15 min



(b) Flight 18, 30-45 min

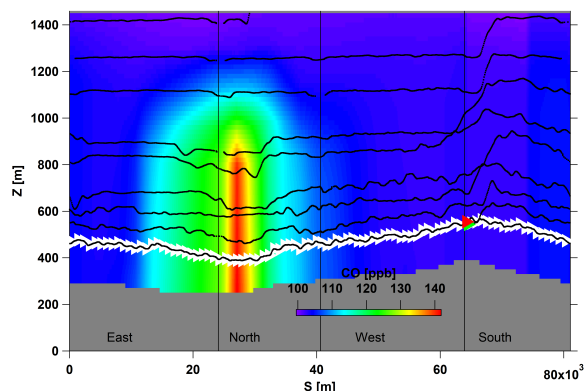


(c) Flight 18, 60-75 min

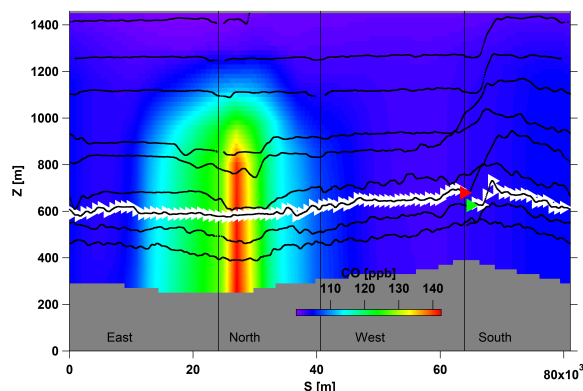


(d) Flight 18, 90-105 min

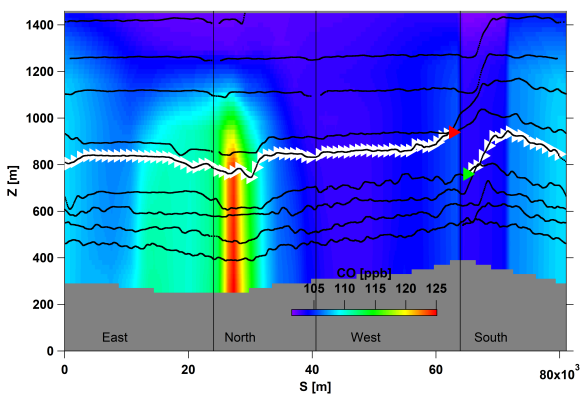
Figure 3.15: Four of the eight SO_2 concentration screens, generated for flight 18. The location and direction (to the right) of the aircraft along the flight tracks is shown with white triangles. The green triangle marks the starting point at each level. The path terminates at the red triangle. At each level, the aircraft travels around the facility, from the green triangle to the red, in about 15 min. Vertical profiles extracted along the flight track, comprise screens for each 15 min. Therefore, the temporal evolution of the system can be studied.



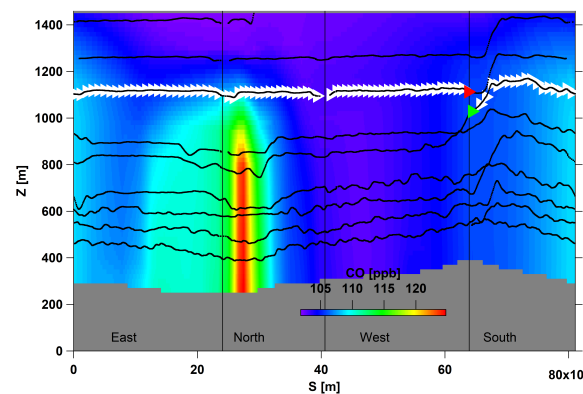
(a) Flight 18, first 15 min



(b) Flight 18, 30-45 min



(c) Flight 18, 60-75 min



(d) Flight 18, 90-105 min

Figure 3.16: Four of the eight CO concentration screens, generated for flight 18. The location and direction (to the right) of the aircraft along the flight tracks is shown with white triangles. The green triangle marks the starting point at each level. The path terminates at the red triangle. At each level, the aircraft travels around the facility, from the green triangle to the red, in about 15 min. Vertical profiles extracted along the flight track, comprise screens for each 15 min. Temporal variation in CO levels can be seen from the figure.

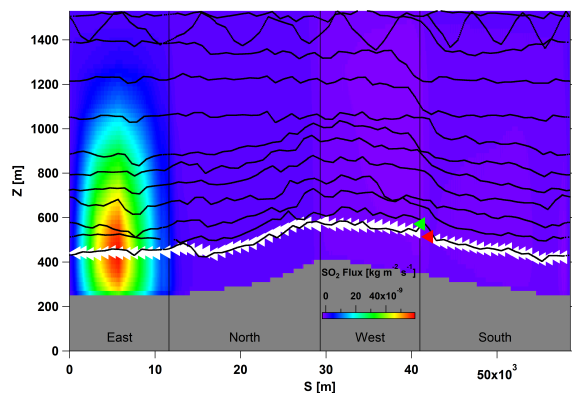
Table 3.6: Advective air fluxes through the lateral sides and the top of the box and the rate of air densification, were estimated for periods of ~ 15 min during flight 18. Estimations were made based on the vertical profiles extracted from the GEM-MACH model (section 2.2.2). The net air flux through the lateral sides remains positive (out of the box) but decreases, over time. The average net air flux through the lateral walls is positive and the average net vertical flux is negative.

Flight 18: 9/3/2013 (UTC)	$E_{air,H}$ [Mt/hr]	$E_{air,M}$ [Mt/hr]	$E_{air,V}$ [Mt/hr]
20:58:01 - 21:13:17	77.4	-1.70	-79.1
21:13:17 - 21:28:28	61.7	-0.003	-61.8
21:28:28 - 21:43:41	61.6	0.01	-61.5
21:43:41 - 21:58:38	61.8	-10.90	-72.7
21:58:38 - 22:12:44	46.0	-1.11	-47.1
22:12:44 - 22:27:25	32.7	-0.05	-32.8
22:27:25 - 22:42:01	35.6	0.03	-35.6
22:42:01 - 22:56:29	33.0	-9.23	-42.1
Average	51.2	-2.86	-54.1

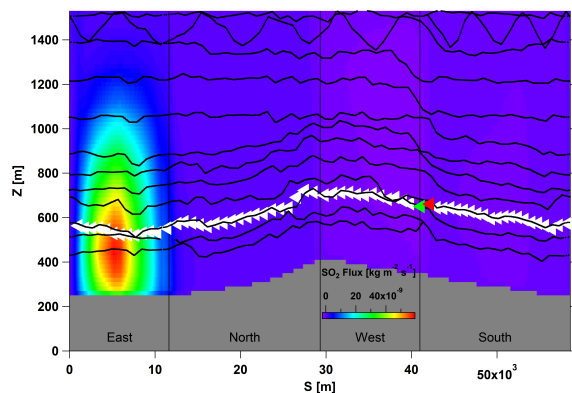
advective flux (Figure 3.18). Four out of eight generated SO_2 and CO flux screens, corresponding to four different ~ 15 min of flight 18, are also shown in Figures 3.19 and 3.20.

Results of SO_2 and CO emission rate estimations are presented in Tables 3.7, 3.8, 3.9 and 3.10 and also plotted as solid lines in Figures 3.21, 3.22, 3.23 and 3.24. The average surface deposition rates ($E_{C,VD}$) of SO_2 were determined based on surface mixing ratios extracted from the GEM-MACH model to be 5.75 kg/hr for flight 8 and 285.50 kg/hr for flight 18 (Figure 2.9). TERRA estimations of deposition rates were also made, as described in section 2.4 and by utilizing equation 1.7. Average SO_2 deposition rate was estimated to be 5.09 kg/hr for flight 8 and 281.71 kg/hr for flight 18 which shows 11.5% and 1.3% deviation from model extracted values, respectively. CO depositions were negligible, since for all cases the deposition velocity V_D is assumed to be near zero for CO [27]. In generating the results presented in Tables 3.7 and 3.9, model SO_2 deposition rates of $E_{C,VD,8} = 5.72$ kg/hr and $E_{C,VD,18} = 285.50$ kg/hr were used.

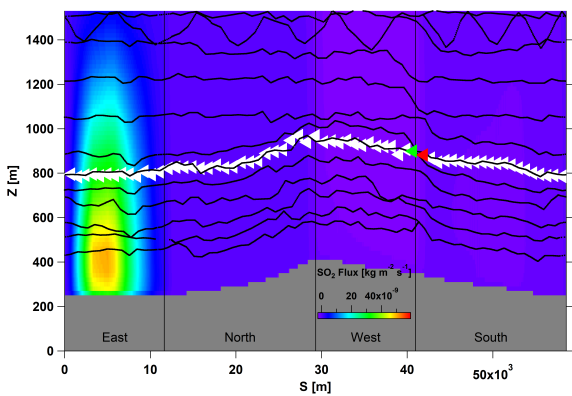
The temporal fluctuation in estimated SO_2 emissions can be seen from Tables 3.7 and 3.9. Breakdown of the total emission rate (E_C), shows that



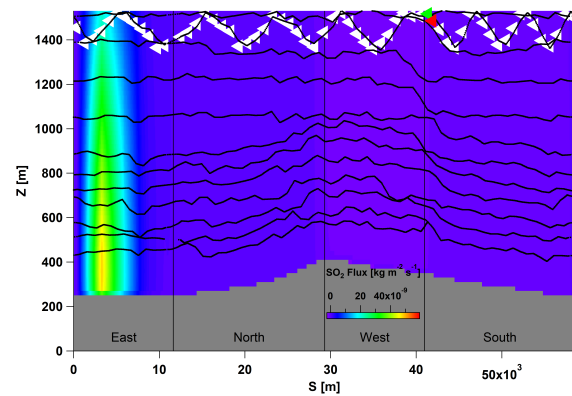
(a) Flight 8, first 10 min



(b) Flight 8, 20-30 min



(c) Flight 8, 50-60 min



(d) Flight 8, 110-120 min

Figure 3.17: Four of the twelve SO_2 advective horizontal flux screens, generated for flight 8. The location and direction (to the left) of the aircraft along the flight tracks is shown with white triangles. The green triangle marks the starting point at each level. The path terminates at the red triangle. At each level, the aircraft travels around the facility, from the green triangle to the red, in about 10 min. The temporal evolution of the SO_2 flux can be seen from the figure, in this case the total flux is decreasing with time.

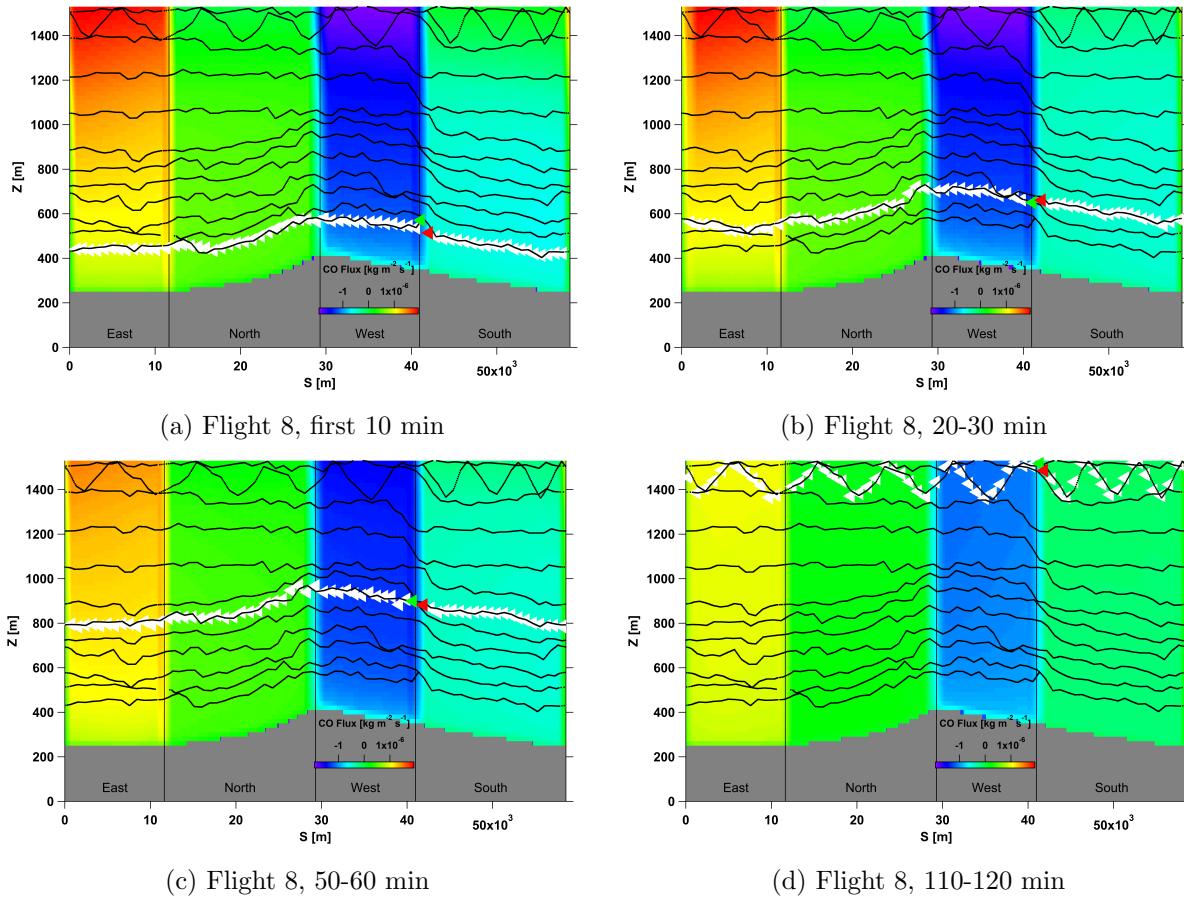
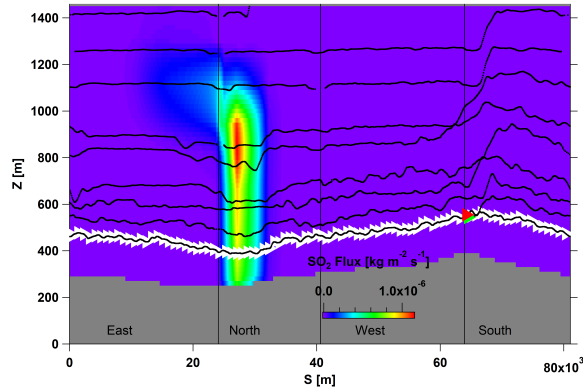
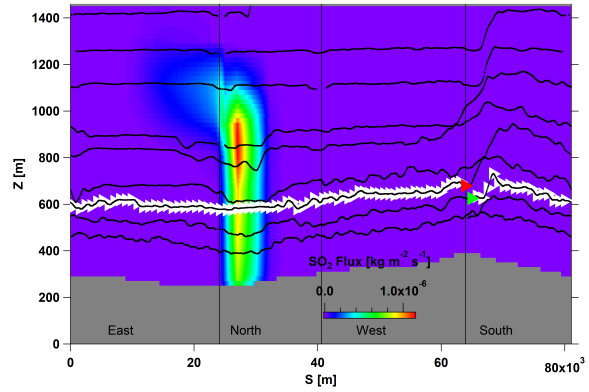


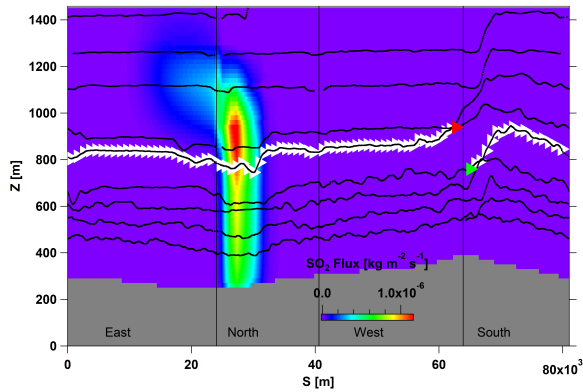
Figure 3.18: Four of the twelve CO advective horizontal flux screens, generated for flight 8. The location and direction (to the left) of the aircraft along the flight tracks is shown with white triangles. The green triangle marks the starting point at each level. The path terminates at the red triangle. At each level, the aircraft travels around the facility, from the green triangle to the red, in about 10 min. The temporal evolution of the CO flux can be seen from the figure, in this case fluxes through the East and West walls are decreasing with time, at different rates.



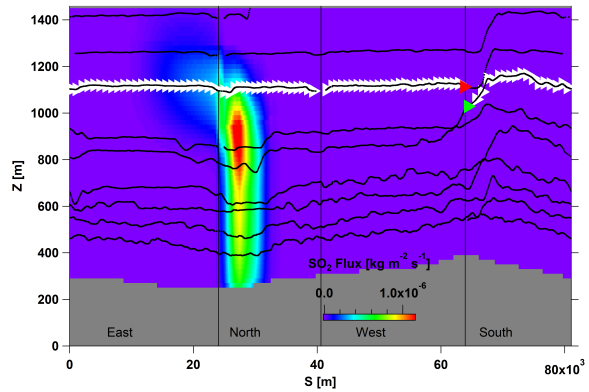
(a) Flight 18, first 15 min



(b) Flight 18, 30-45 min

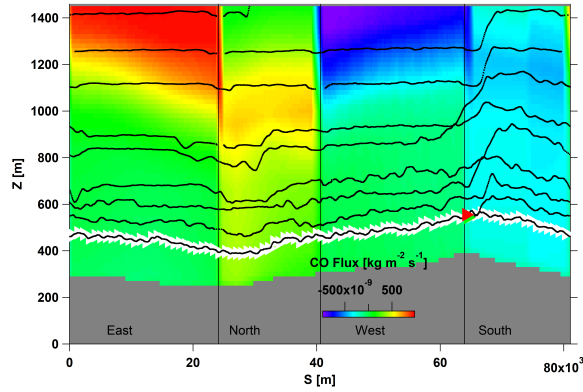


(c) Flight 18, 60-75 min

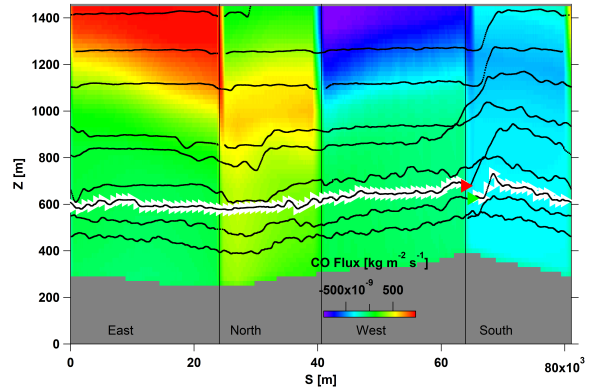


(d) Flight 18, 90-105 min

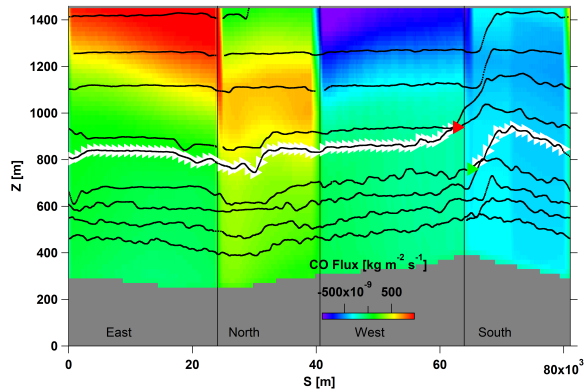
Figure 3.19: Four of the eight SO_2 advective horizontal flux screens, generated for flight 18. The location and direction (to the right) of the aircraft along the flight tracks is shown with white triangles. The green triangle marks the starting point at each level. The path terminates at the red triangle. At each level, the aircraft travels around the facility, from the green triangle to the red, in about 15 min.



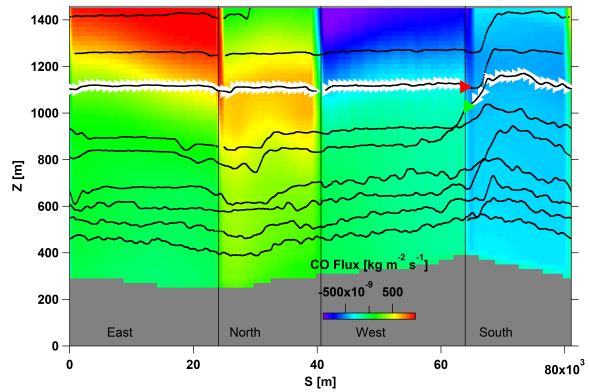
(a) Flight 18, first 15 min



(b) Flight 18, 30-45 min



(c) Flight 18, 60-75 min



(d) Flight 18, 90-105 min

Figure 3.20: Four of the eight CO advective horizontal flux screens, generated for flight 18. The location and direction (to the right) of the aircraft along the flight tracks is shown with white triangles. The green triangle marks the starting point at each level. The path terminates at the red triangle. At each level, the aircraft travels around the facility, from the green triangle to the red, in about 15 min.

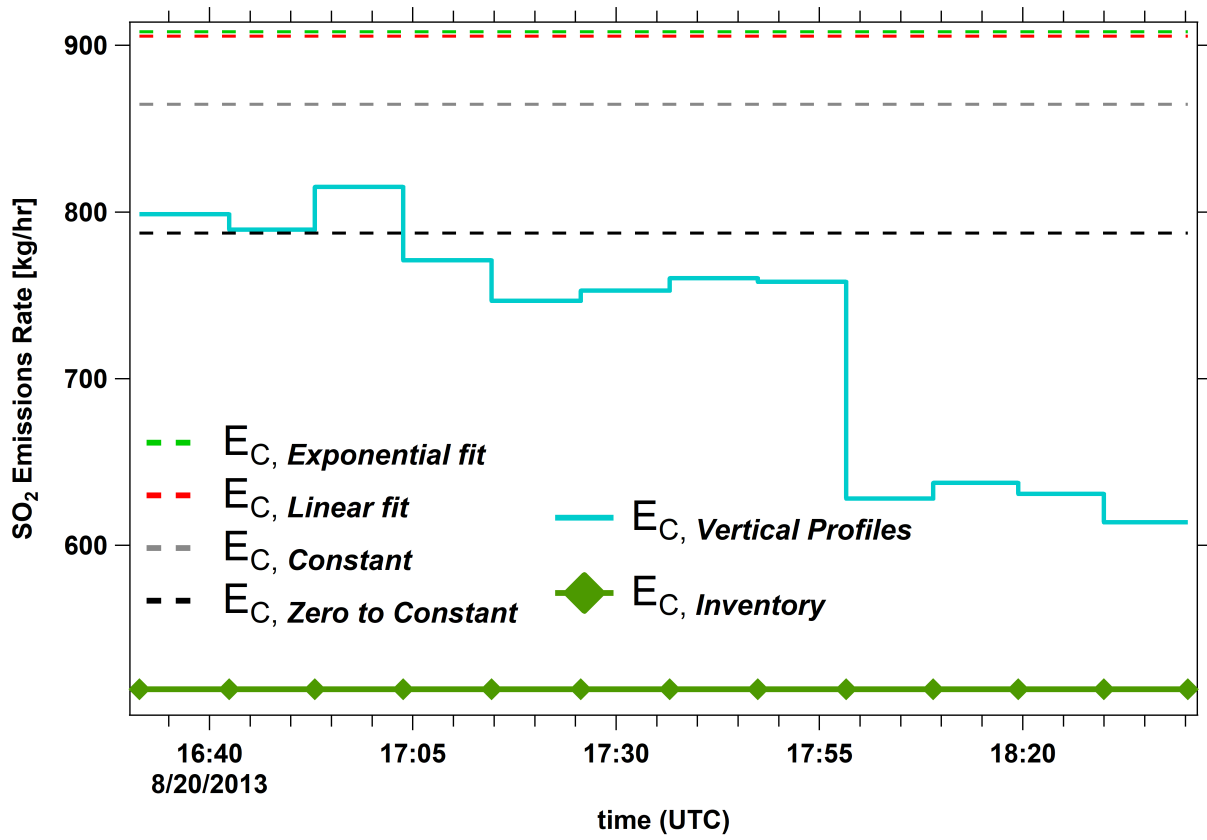


Figure 3.21: SO_2 emissions by sources within CNRL on 20 August 2013 (Flight 8) were estimated based on model extracted values in two different approaches: 1) AFT (section 2.2.1) estimation over ~ 2 hours and 2) VP (section 2.2.2) estimations over periods of ~ 10 min. The first approach requires extrapolations below the lowest flight level for SO_2 mixing ratio screens. Different extrapolation methods resulted in different estimates. Four of these methods are compared to each other (dashed lines). Emissions retrieved for each ~ 10 minute with VP method (no extrapolation needed) are also plotted for comparison. Note how emission rates fluctuate and decrease with time. Model emission inventory is also plotted for comparison.

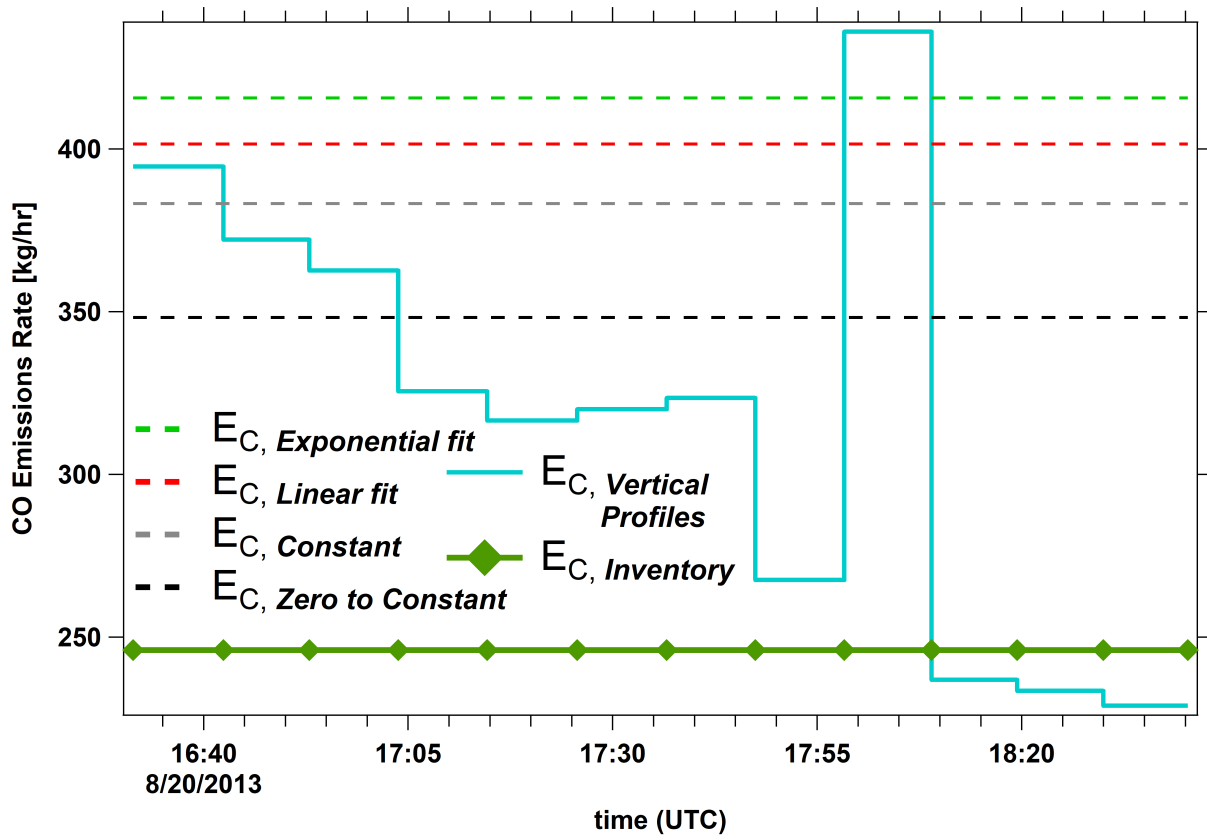


Figure 3.22: CO emissions by sources within CNRL on 20 August 2013 (Flight 8) were estimated based on model extracted values in two different approaches: 1) AFT (section 2.2.1) estimation over ~ 2 hours and 2) VP (section 2.2.2) estimations over periods of ~ 10 min. The first approach requires extrapolations below the lowest flight level for CO mixing ratio screens. Different extrapolation methods resulted in different estimates. Four of these methods are compared to each other (dashed lines). Emissions retrieved for each ~ 10 minute with VP method (no extrapolation needed) are also plotted for comparison. Note how emission rates fluctuate and decrease with time. Model emission inventory is also plotted with lines and markers.

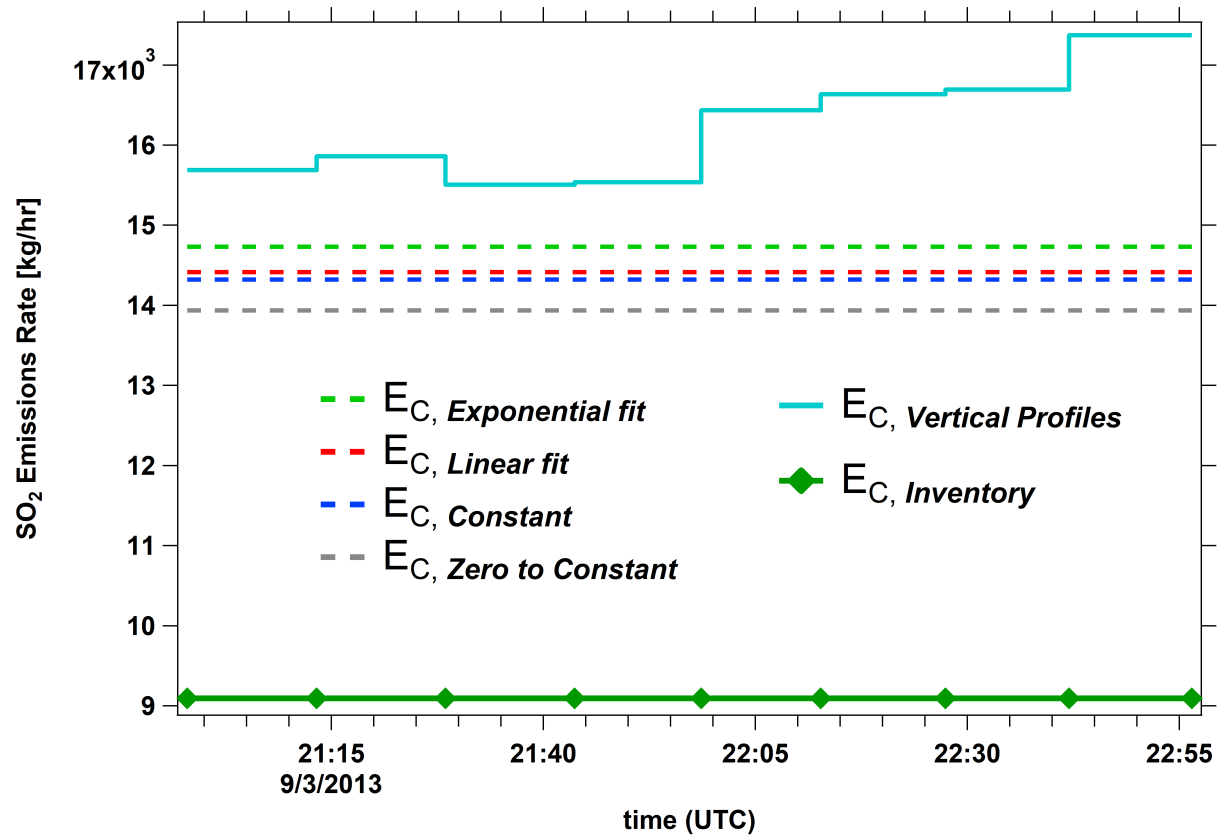


Figure 3.23: SO₂ emissions by sources within Syncrude on 3 September 2013 (during flight 18) were estimated based on model extracted values in two different approaches: 1) AFT (section 2.2.1) estimation over ~2 hours and 2) VP (section 2.2.2) estimation over ~ 15 min. The first approach required extrapolations below the lowest flight level for SO₂ mixing ratio screens. Different extrapolation methods resulted in different estimates. Four of these methods are compared to each other (dashed lines). Emissions retrieved for each ~15 minute with VP method (no extrapolation needed) are also plotted for comparison. Note how emission rates fluctuate and increase by time. SO₂ model emission inventory is also plotted for this flight.

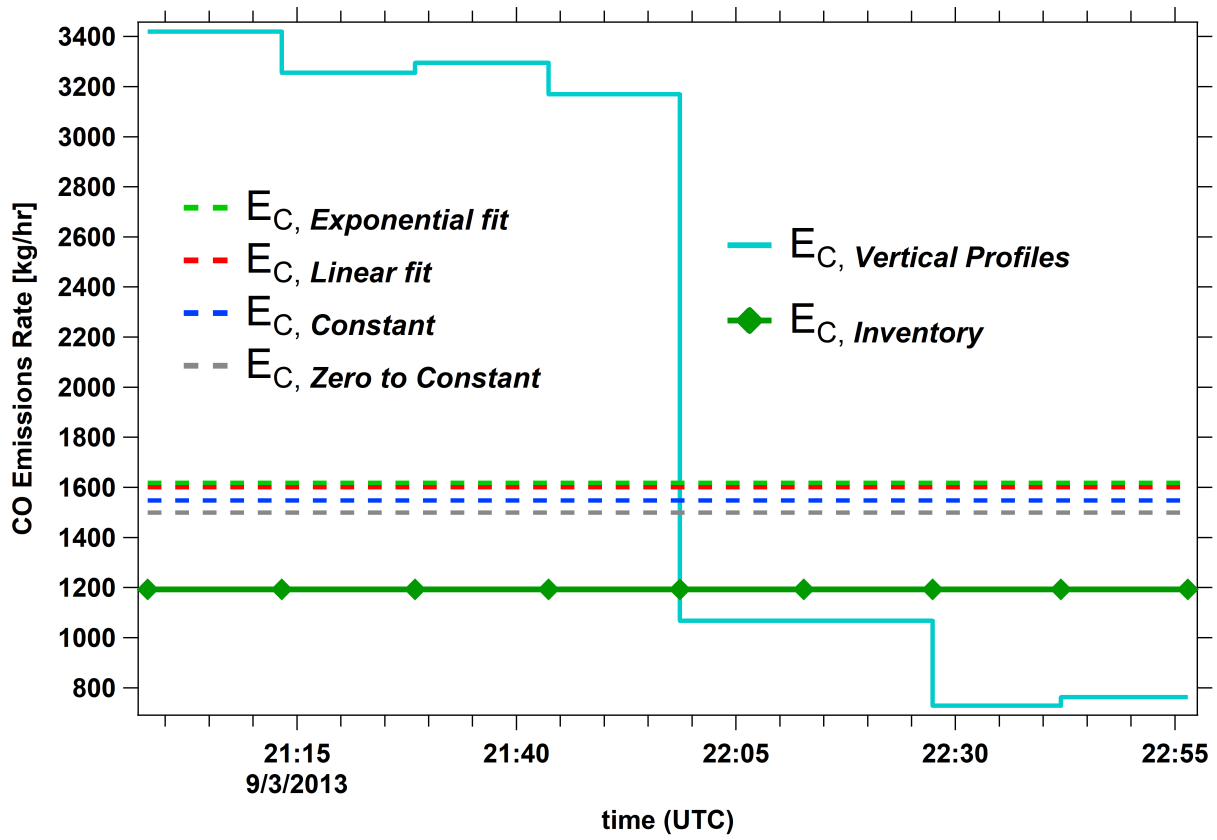


Figure 3.24: CO emissions by sources within Syncrude on 3 September 2013 (during flight 18) were estimated based on model extracted values in two different approaches: 1) AFT (section 2.2.1) estimation over ~ 2 hours and 2) VP (section 2.2.2) estimation over ~ 15 min. The first approach requires extrapolations below the lowest flight level for CO mixing ratio screens. Different extrapolation methods resulted in different estimates. Four of these methods are compared to each other (dashed lines). Emissions retrieved for each ~ 15 minute with VP method (no extrapolation needed) are also plotted for comparison. Note how emission rates fluctuate and increase by time. CO model emission inventory is plotted for comparison.

Table 3.7: SO₂ emission rates were derived based on the vertical profiles extracted from the GEM-MACH model for flight 8, as described in section 2.2.2. Emission rates were estimated for periods of ~ 10 min.

Flight 8: 8/20/2013 (UTC)	$E_{C,H}$ [kg/hr]	$E_{C,M}$ [kg/hr]	$E_{C,V}$ [kg/hr]	E_C [kg/hr]
16:31:24 - 16:42:27	793.31	0.017	-0.46	798.59
16:42:27 - 16:52:57	783.79	-0.418	-0.54	789.42
16:52:57 - 17:03:49	807.33	-0.664	1.34	815.08
17:03:49 - 17:14:41	763.03	-0.004	2.21	771.00
17:14:41 - 17:25:41	738.81	-0.013	2.13	746.71
17:25:41 - 17:36:36	745.03	-0.001	2.01	752.80
17:36:36 - 17:47:27	752.33	-0.003	2.13	760.22
17:47:27 - 17:58:19	749.51	-1.139	1.60	758.01
17:58:19 - 18:09:00	603.31	-0.180	18.73	627.97
18:09:00 - 18:19:27	634.29	0.025	-2.63	637.38
18:19:27 - 18:29:59	627.66	-0.023	-2.53	630.90
18:29:59 - 18:40:19	610.03	-0.021	-2.02	613.79
Average	717.37	-0.202	1.83	725.16
			$E_{C,Inventory}$	513.73

the horizontal advective flux ($E_{C,H}$) contributes to almost 99% of the total SO₂ emissions for flight 8 and 98% for flight 18. With the addition of the vertical advective flux ($E_{C,V}$), advective fluxes contribute to above 99% of the total SO₂ emissions (contribution of turbulence and chemistry processes are assumed to be zero, Equation 2.6). This is a reflection of our assumption for SO₂ emissions based on the results of Gordon et al., [12]. On the other hand, estimated emission rates for CO (Tables 3.8 and 3.10), show a totally different emissions allocation. Due to high background concentrations of CO along the box walls (from natural and anthropogenic sources) and the fact that the net horizontal advective air flux is into the box (negative) for flight 8, a net horizontal advective CO flux is entering the box through the lateral walls. Similarly, the net positive vertical air flux (out of the box) through the box top, results in a vertical CO flux leaving the box through the top. For flight 18, a net negative vertical air flux (into the box) results in a vertical CO flux entering the box through the top. The change in compound mass due to air densification is significant for CO (more than 200 times that of SO₂) and it is equal to about 15% of the total CO emissions (see Table 3.8),

Table 3.8: CO emission rates were derived based on the vertical profiles extracted from the GEM-MACH model for flight 8, as described in section 2.2.2. Emission rates were estimated for periods of ~ 10 min.

Flight 8: 8/20/2013 (UTC)	$E_{C,H}$ [kg/hr]	$E_{C,M}$ [kg/hr]	$E_{C,V}$ [kg/hr]	E_C [kg/hr]
16:31:24 - 16:42:27	1352.5	3.83	-954.2	394.5
16:42:27 - 16:52:57	1391.6	-93.8	-1113.3	372.1
16:52:57 - 17:03:49	-1749.4	-144.8	1967.3	362.6
17:03:49 - 17:14:41	-1459.8	-0.96	1784.3	325.5
17:14:41 - 17:25:41	-1428.2	-3.11	1741.6	316.5
17:25:41 - 17:36:36	-1332.7	-0.28	1652.4	320.0
17:36:36 - 17:47:27	-1417.5	-0.80	1740.1	323.5
17:47:27 - 17:58:19	-1307.7	-270.1	1305.1	267.5
17:58:19 - 18:09:00	-8512.6	-49.01	8899.6	436.0
18:09:00 - 18:19:27	1508.4	6.78	-1264.8	236.8
18:19:27 - 18:29:59	1438.6	-6.34	-1211.6	233.4
18:29:59 - 18:40:19	1195.6	-5.97	-972.7	228.9
Average	-860.09	-47.05	1131.1	318.1
			$E_{C,Inventory}$	246.0

for flight 8.

The average emissions estimated over periods of ~ 10 min ($\bar{E}_{SO_2} = 725.16$ kg/hr and $\bar{E}_{CO} = 311.3$ kg/hr) for flight 8 and estimated over periods of ~ 15 min ($\bar{E}_{SO_2} = 16220.0$ kg/hr and $\bar{E}_{CO} = 2039.6$ kg/hr) for flight 18, can be compared to the emission rates estimated over the box flight time of ~ 2 hrs (section 3.1.7). In general, flight time estimations (~ 2 hrs) are 8-30% higher for flight 8. Flight time estimations of flight 18 are 9-32% lower. This could be a result of overestimation in advective air flux due to different assumptions for the time period over which the system is assumed to be in steady state (~ 2 hr vs. 10-15 min), and/or due to AFT-kriging interpolation. This will be discussed in Chapter 4.

Comparing these results with the emissions inventories input in the GEM-MACH model (Tables 2.1 and 2.2) shows a general overestimation by both AFT and VP methods. Tables 3.11 and 3.12 show summaries of these comparisons. Emissions estimated with the AFT method for different extrapolation methods for the surface level are compared with the GEM-MACH model inputs for SO_2 and CO. All of the methods overestimate the model

Table 3.9: SO₂ emission rates were derived based on the vertical profiles extracted from the GEM-MACH model for flight 18, as described in section 2.2.2. Emission rates were estimated for periods of ~ 15 min.

Flight 18: 9/3/2013 (UTC)	$E_{C,H}$ [kg/hr]	$E_{C,M}$ [kg/hr]	$E_{C,V}$ [kg/hr]	E_C [kg/hr]
20:58:01 - 21:13:17	15393.0	-23.1	-14.1	15687.4
21:13:17 - 21:28:28	15585.1	-0.05	-10.8	15859.9
21:28:28 - 21:43:41	15231.2	0.17	-11.3	15505.3
21:43:41 - 21:58:38	15114.4	-147.9	-13.7	15534.1
21:58:38 - 22:12:44	16155.9	-14.8	-22.3	16434.0
22:12:44 - 22:27:25	16362.0	-0.63	-15.2	16632.9
22:27:25 - 22:42:01	16423.3	0.38	-17.0	16691.5
22:42:01 - 22:56:29	17017.8	-132.2	-20.3	17415.2
Average	15910.3	-39.8	-15.6	16220.0
			$E_{C,Inventory}$	9094.4

Table 3.10: CO emission rates were derived based on the vertical profiles extracted from the GEM-MACH model for flight 18, as described in section 2.2.2. Emission rates were estimated for periods of ~ 15 min.

Flight 18: 9/3/2013 (UTC)	$E_{C,H}$ [kg/hr]	$E_{C,M}$ [kg/hr]	$E_{C,V}$ [kg/hr]	E_C [kg/hr]
20:58:01 - 21:13:17	10999.5	-142.8	-7723.3	3419.0
21:13:17 - 21:28:28	9299.0	-0.33	-6044.0	3255.4
21:28:28 - 21:43:41	9317.3	1.08	-6021.2	3295.0
21:43:41 - 21:58:38	9346.6	-935.1	-7112.6	3169.0
21:58:38 - 22:12:44	5654.7	-94.2	-4681.2	1067.7
22:12:44 - 22:27:25	4019.0	-3.91	-3263.3	759.6
22:27:25 - 22:42:01	4276.3	2.38	-3545.9	728.0
22:42:01 - 22:56:29	4034.6	-782.5	-4193.6	762.3
Average	7118.4	-244.4	-5323.1	2057.0
			$E_{C,Inventory}$	1192.4

emissions inventory. The average hourly estimations with the VP method are also higher than model emissions, with a better performance compared to AFT estimations for the case of flight 8 and a weaker performance in the case of flight 18.

The results of Tables 3.11 and 3.12 show that the overestimation is independent of the method used in estimating emissions (AFT vs. VP). Further, it can be seen from Table 3.12 for flight 18 emissions that AFT estimates are closer than VP estimates to the model emissions inventory, despite expectation (the VP method removes the need for extrapolations below the

Table 3.11: Comparing the estimated emissions of SO₂ and CO by CNRL during flight 8 with the GEM-MACH model emissions inputs. Both AFT and VP methods overestimate the emissions. Only AFT Constant and Linear fit methods are compared here, as they have shown the best performance out of the five TERRA extrapolation methods. Percentage differences from the model inputs are shown for each method.

Flight 8	Model Input	AFT-Constant	AFT-Linear Fit	VP	estimation
SO ₂ [kg/hr]	513.7	864.7	905.6	725.2	
% Difference		↑ 68%	↑ 76%	↑ 41 %	over
CO [kg/hr]	246.0	383.2	415.7	318.1	
% Difference		↑ 56%	↑ 69%	↑ 26 %	over

Table 3.12: Comparing the estimated emissions of SO₂ and CO by Syncrude during flight 18 with the GEM-MACH model emissions inputs. Both AFT and VP methods overestimate the emissions. Only AFT Constant and Linear fit methods are compared here, as they have shown the best performance out of the five TERRA extrapolation methods. Percentage differences from the model inputs are shown for each method.

Flight 18	Model Input	AFT-Constant	AFT-Linear Fit	VP	estimation
SO ₂ [kg/hr]	9094.4	14320.9	14413.2	16220.0	
% Difference		↑ 57%	↑ 58%	↑ 78%	over
CO [kg/hr]	1192.4	1547.6	1561.8	2039.6	
% Difference		↑ 30%	↑ 31%	↑ 71%	over

lowest flight level among other improvements and was developed for testing AFT). This is due to an error arising from kriging interpolation, which will be discussed in Chapter 4.

Chapter 4

Discussions

The purpose of this work was to evaluate aircraft-based area source emissions estimation. TERRA schemes were studied as the main example of an aircraft-based method for emissions rate retrieval [12] and AQ forecasts by the GEM-MACH model were used for virtual aircraft-based sampling of meteorological and compound mixing ratio data [18]. AFT extraction of data from the model mimics aircraft-based measurements (section 2.2.1). Therefore, estimations made using this method are the primary case of investigation. The VP method was developed to provide a platform for testing AFT (section 2.2.2). More specifically, the method by which mixing ratio and meteorological screens were constructed in AFT could be examined by comparing the results to those generated by the VP method.

4.1 Sub-flight-level Gaussian Interpolation (SGI)

One of the advantages of extracting vertical profiles (VP) from the model is that a consistently distributed/spaced grid of data points is extracted and projected on the screen, which is then linearly interpolated (vertically and horizontally) to fill the screen (Figure 2.7). This is opposed to AFT data sampling which results in a more spatially scattered data set to be projected on the screen, which is then filled by kriging interpolation (Figure 2.5). The idea is that generating screens using VP extracted data lowers the interpola-

tion error. For instance, comparing the AFT generated screens for flight 18 (Figure 3.8) with vertical profiles for the same flight (Figures 3.15 and 3.16), reveals some of the differences. A more perceptive way to make this comparison is by looking at the centerline plots for these screens. Figure 4.1 depicts SO₂ centerlines (vertical profiles passing through the plume center/maxima) for flight 18. On the horizontal axis the SO₂ levels are shown and heights above mean sea level (amsl) are shown on the vertical. Horizontal dashed lines (gray) show flight levels, Levels 3 and 4 are labeled. The green line is the extracted vertical profile at $s = 27.2$ km and while the aircraft was at the 3rd level. The virtual aircraft sampled one data point from the vertical profile (green line) at this s location and at the height of the 3rd flight level (lowest black circle). After about 15 min (after the centerline evolved over time from the green line to the red line) the aircraft sampled another data point at $s = 27.2$ km, this time at the height of the 4th flight level (second lowest black circle). The same is true for sampling at other flight levels (black circles/AFT Extracted). AFT treats these extracted data points as sampling at different spatial points (consecutive heights) and ignores the evolution of the plume during the elapsed time. Further, the complete vertical profile is reconstructed from these points by kriging interpolation between the points (black dashed line). The vertical profiles on the other hand, are extracted at their respective instants of time for all the heights (green and red lines). The average of the two vertical profiles (dashed blue line) could be considered as representing the average SO₂ mixing ratio values for the heights between the 3rd and the 4th flight levels. Therefore, the krigged AFT vertical profile (black line) can be compared to this average (blue line). It can be seen from Figure 4.1 (inside the cyan box) that the krigged line estimates lower SO₂ concentrations for the highlighted heights, compared to the mean vertical profile. As shown on the figure, a liner interpolation (cyan line) improves concentration estimations for the vertical gap between the flight levels 3 and 4. Similar observations can be made for other heights and in general for other

screens.

While in many of the cases averaging or linear interpolation improves the estimates, there are cases where it results in underestimations. One such case is where there is a peak or maxima located in the gap between the two flight levels, especially when the spacing between the levels is relatively large. While developing the analysis methods for this work, model outputs from three different modified versions of the GEM-MACH model (with different wind fields and emissions inventories) were examined. The results presented in this work are from the model version GEM-MACHv2. Figure 4.2 shows SO₂ screens from a previous GEM-MACH version model run during flight 18. It demonstrates the case of a plume center being located between two flight levels with a relatively large spacing. Looking at the VP screen (Figure 4.2b), an elevated SO₂ plume can be seen with the plume center located at a height between flight levels 5 and 6 where there is a wide gap between the levels. Kriging interpolation of the AFT extracted model values places the plume center on the 6th level (Figure 4.2a). The difference in estimated SO₂ levels with both methods becomes more apparent when the centerlines are compared. As can be seen from Figure 4.3, AFT samples one data point at the 5th level and another one at the 6th (blue circles) and kriging interpolation estimates an increase in SO₂ from level 5 upward with the maximum (plume center) at the 6th level, while the plume center is at a height between the two levels (green dashed line). To improve mixing ratio estimations for these heights, the krigged values were removed from the screen in the vicinity of the plume. Assuming a vertical Gaussian distribution of SO₂ concentrations, a Gaussian vertical profile (red dashed line) was fitted to the AFT extracted values (blue circles). The resulting profile places the plume maximum at the right height level and improves concentration estimations. Repeating this process for vertical profiles at all the other s locations results in an AFT SO₂ screen with less deviation from the corresponding VP screen (Figure 4.2c). We refer to this process of correcting meteorology and mixing ratio

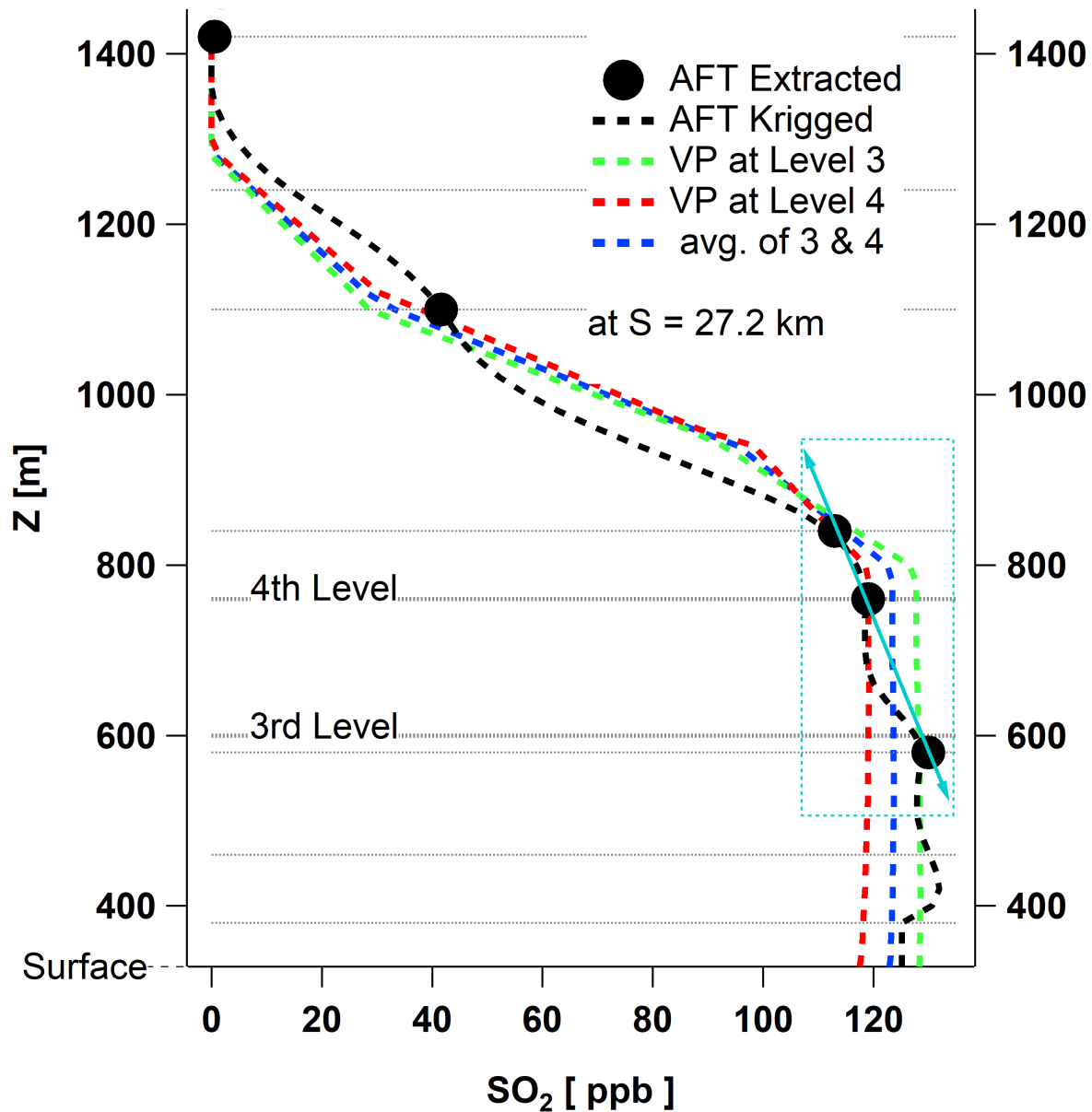


Figure 4.1: Flight 18 SO_2 centerlines at $s = 27.2$ km for different screens are compared. z on the vertical axis is height above mean sea level (amsl). Dashed green and red lines are vertical profiles at s during the 5th and 6th 15 min of the flight. Black circles are the AFT extracted data points and the dashed black line is the vertical profile reconstructed from the extracted data points by kriging. The cyan line (with arrows) represents 2D linear interpolation instead of kriging. Compared to the mean vertical distribution for these heights and the time period between flight at levels 3 and 4 (blue), the linear interpolation shows a better performance.

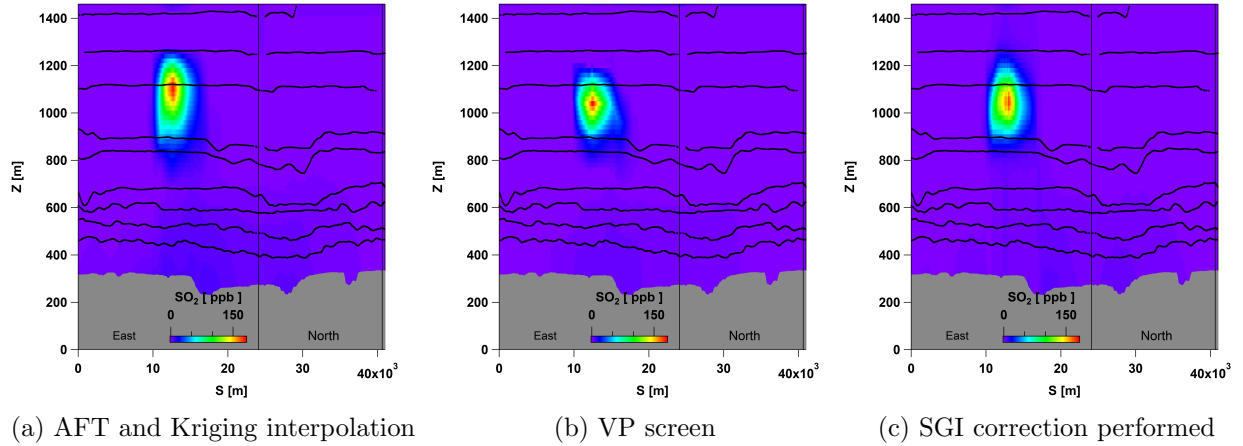


Figure 4.2: Comparing the AFT (a) and VP (b) screens shows that kriging misplaces the plume maximum. SGI correction improves the estimation (c).

screens as Sub-flight-level Gaussian Interpolation (SGI). Application of SGI improved the emissions estimation (relative to emissions inventory) by 15% for the studied case. In analyzing aircraft-based measurements, this method is suggested wherever there is a probability of a plume center being located between two widely spaced flight levels such as the case shown in Figure 4.2.

4.2 AFT Krigged Screen and Surface Layer Extrapolation

TERRA has several extrapolation methods for filling the gap below the lowest flight level, which result in different estimation of the emission rates. Tables 3.11 and 3.12 compare the results for different methods to the model input values and VP estimates. As before, performance of different methods can be compared by looking at the centerlines. Figure 4.4 compares flight 8 SO₂ centerlines of two AFT extrapolation method to a level 0 (first 10 min segments of the flight) vertical profile (VP). Level 11(highest) VP is also plotted for comparison. Looking at centerlines for the surface layer (below the lowest flight level), it can be seen that the zero level VP SO₂ mixing ratios for these heights lie between the Constant and Linear fit extrapolated values (section 1.2.2). Results of the other extrapolation methods diverge more from the VP centerline, therefore Constant and Liner fit methods are the

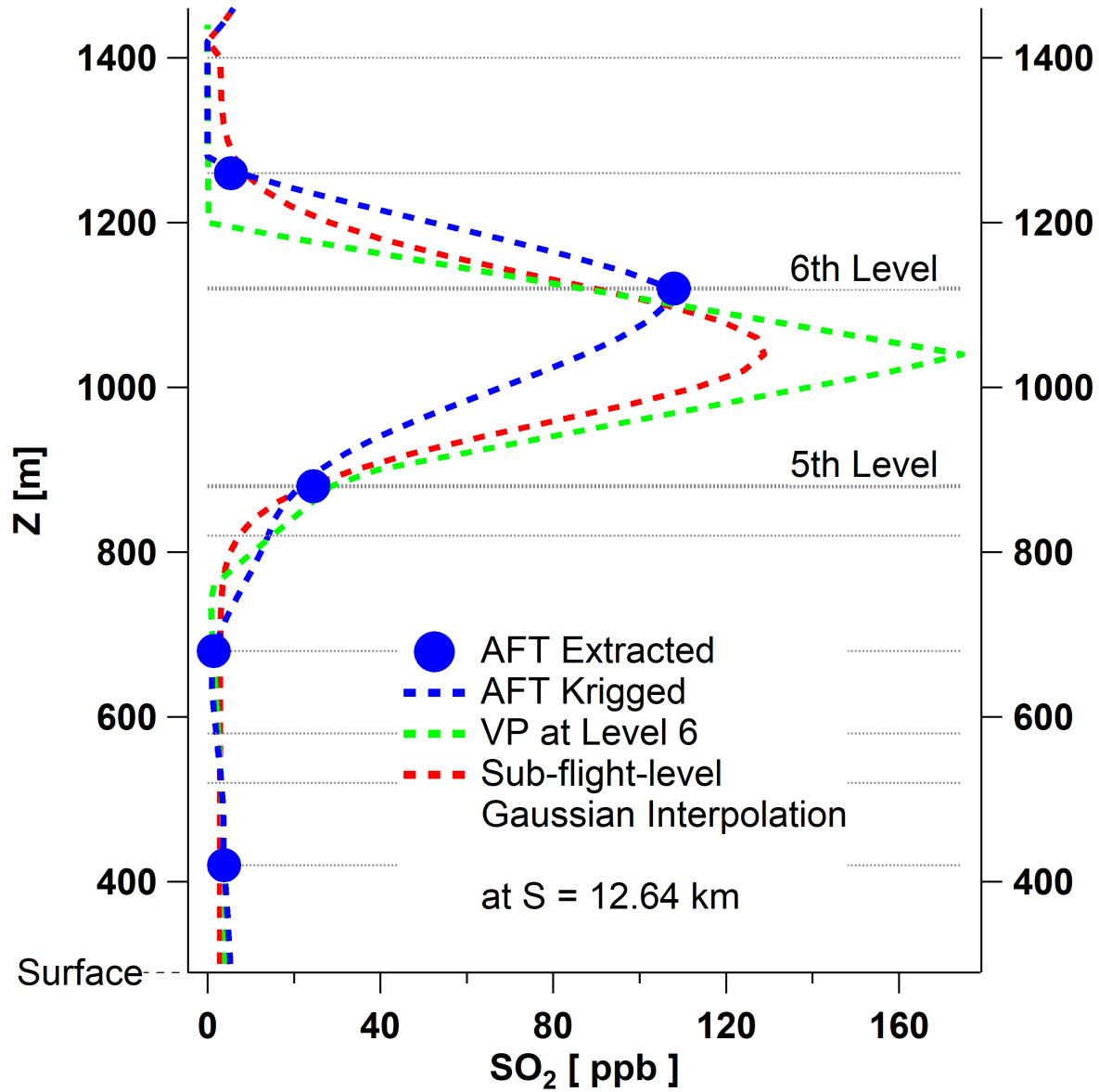


Figure 4.3: Sub-flight-level Gaussian Interpolation (SGI): AFT and VP centerlines of the plume shown in Figure 4.2 are compared here. z on the vertical axis is height above mean sea level (amsl). Looking at the green vertical profile, the peak is located between levels 5 and 6. Kriging misplaces the maximum on the 6th level. SGI correction places the maximum at the right height and improves the estimation.

best candidates for filling the gap below the lowest flight level. The same is true for all the other studied cases. In general the *Zero* and *Zero to Constant* methods are applicable to the cases with an elevated plume located well above the lowest flight level (see Figure 4.2 for an example of an elevated plume). For a low plume (Figures 3.7 and 3.8), the applicable extrapolation methods are *Constant*, *Linear fit* and *Exponential fit* (section 1.2.2). The estimations made by the first two (Constant and Linear fit) are the closest to the vertical profiles extracted from the model for altitudes below the lowest flight level (surface layer).

Kriging is a weighted (spatially) interpolation method and the interpolation results are biased to the data points sampled in the vicinity of each (s, z) point on the 2D screen along the flight tracks. For instance, the krigged values near the bottom of the screen resemble the temporally corresponding vertical profiles (the first, second and third 10 min segments of the flight) and the values near the top of the screen resemble those of the latest vertical profiles (11th 10 min segment of the flight). This can be seen from Figure 4.4. Therefore, the extrapolated profiles for the surface layer are also biased to measurements along the lowest flight level and correspond to the initial vertical profiles. And if the plume is evolving over time (which is the case for almost all the studied cases in this work) the extrapolated profiles are not in agreement and not comparable to later vertical profiles (Figure 4.4). Consequently, to be able to decide which extrapolation method performs the best we first need to choose a VP generated screen as the one with vertical profiles of reference. In AFT analysis the aircraft sampled distribution of relevant information (e.g. SO_2 mixing ratio) over the ~ 2 hr flight time are assumed to be the temporal mean distributions over this time and the resulting krigged screens are used for estimating the average hourly emission rates. VP generated screens correspond to 10-15 min segments of the flight time and can be averaged to construct screens of temporal mean distribution of mixing ratio data. The mean VP screen can be compared to the krigged

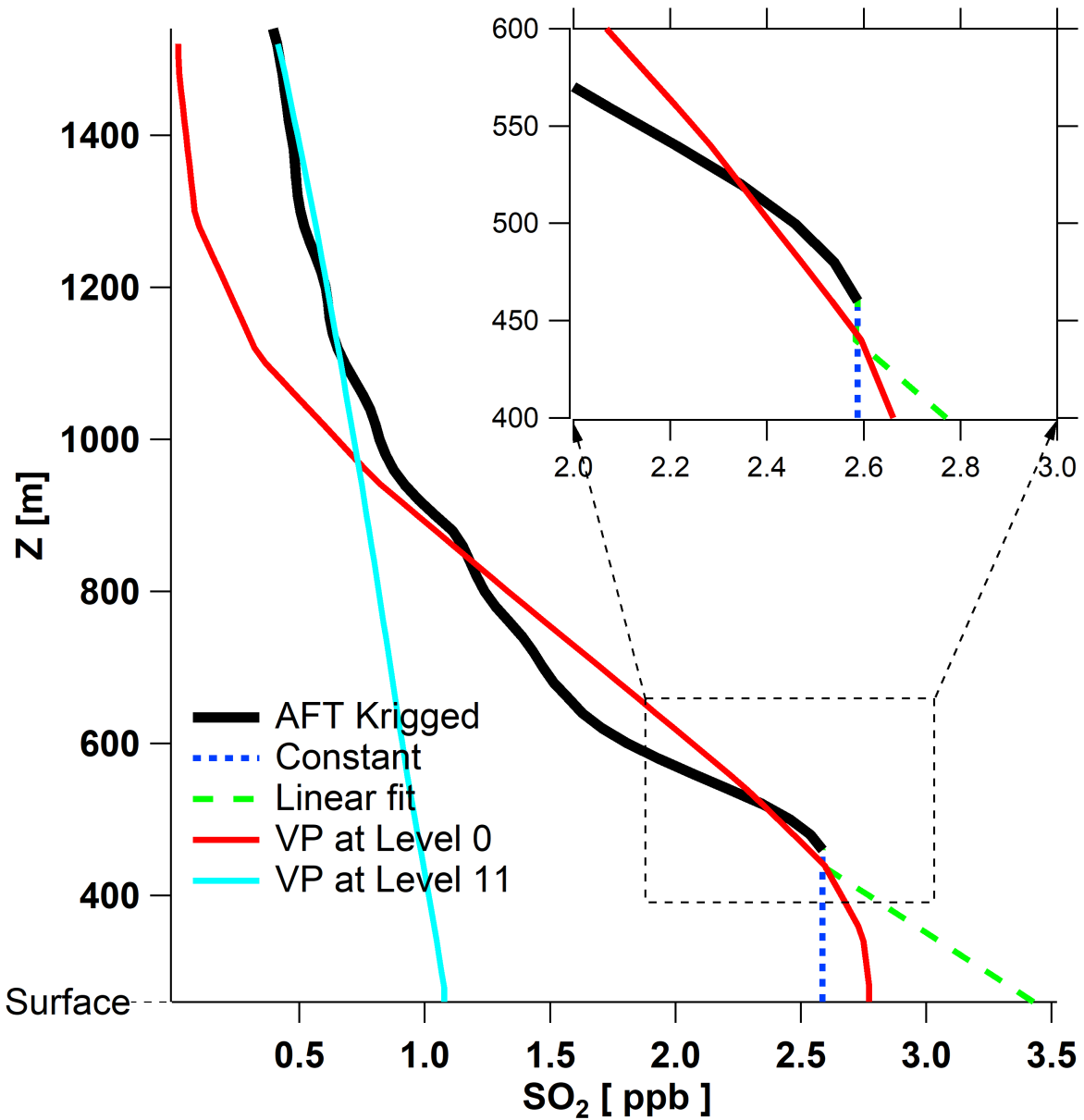


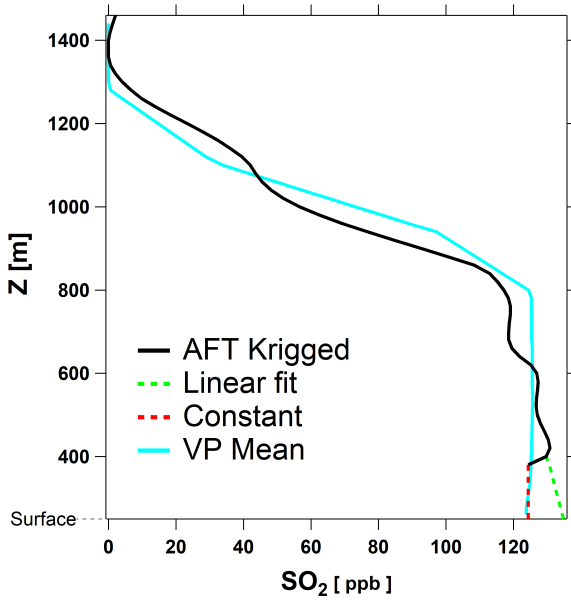
Figure 4.4: Flight 8 SO₂ centerlines at $s = 5680$ m are compared. z on the vertical axis is height above mean sea level (amsl). The black line shows the krigged vertical profile with no values below the lowest flight level. Blue and green dashed lines show the extrapolated values below the lowest flight with Constant and Linear fit methods, respectively. The level 0 vertical profile extracted from the model is plotted as a reference profile. Level 11(highest) VP is also plotted for comparison.

screen. Figure 4.5 compares flight 18 mean vertical profiles of SO₂ and CO to krigged profiles for extrapolation methods Constant and Linear fit. From the figure it can be seen that agreement between the krigged profile and the mean VP is poor for both CO and SO₂, with better performance for SO₂. Nevertheless, the Constant method seems to be a better choice of extrapolation method. The same is true for flight 8 profiles. However, due to the general overestimation in mixing ratio distribution for krigged screens compared to mean VPs, vertical profile comparisons for heights below the lowest flight level are not very useful. Another way to compare these screens is to look at the average mixing ratios on each screen. Table 4.1 demonstrates this comparison. In all cases the Constant method agrees better with the mean VP. For CO, the Linear fit method performs almost as good as the Constant method (less than 0.1% difference). Although krigged screens show overestimations relative to the mean VP for all cases, overestimations in SO₂ levels for flight 8 are relatively higher than other cases. This will be discussed in Section 4.4.

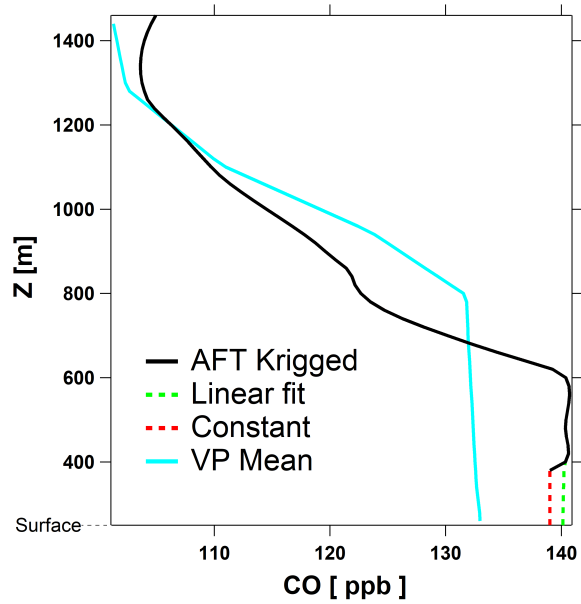
Table 4.1: Comparing average SO₂ and CO mixing ratios on AFT krigged screens extrapolated below the lowest flight level (Constant and Linear fit methods) to mean VP for each case. ↑ indicates overestimation relative to mean VP.

	Mean VP	AFT-Constant	AFT-Linear fit
Flight 8 SO ₂	0.2 [ppb]	↑ 21.1%	↑ 28.1%
Flight 8 CO	97.7 [ppb]	↑ < 0.1%	↑ < 0.1%
Flight 18 SO ₂	6.0 [ppb]	↑ 5.1%	↑ 5.4%
Flight 18 CO	106.8 [ppb]	↑ 0.7%	↑ 0.7%

Due to mixing ratio overestimation by krigged screens, it is expected that AFT emissions estimates deviate more from model emissions inventory compared to VP method estimates. While this is true for flight 8 (Table 3.11), it can be seen from Table 3.12 that flight 18 AFT estimates are closer to model emissions despite the fact that krigged screens overestimate mixing ratios. To address this discrepancy, we need to look at the AFT krigged



(a) SO₂ centerlines



(b) CO centerlines

Figure 4.5: Flight 18 SO₂ and CO centerlines at $s = 27240$ m are compared to mean vertical profiles (cyan). z on the vertical axis is height above mean sea level (amsl). For each case, extrapolated profiles below the lowest flight level are shown with green and red dashed lines for Linear fit and Constant methods respectively. The agreement between the krigged profile (black line) and the mean VP for SO₂ is better than CO, and the Constant method shows a better performance compared to the Linear fit.

screens for flight 18 (Figure 3.8). Due to lack of sampled data near the top of the screen on north and west walls (the highest flight track is broken and does not cover the entire width of the screen at the highest level), kriging interpolation overestimates SO₂ and CO concentrations near the top of the screen. This results in overestimations in the vertical advective fluxes ($E_{C,V}$) entering the box through the top. Which in turn cancel out bigger portions of the horizontal advective fluxes ($E_{C,H}$) in the mass balance equation (Equation 2.6) and result in lower estimated emissions compared to those of the VP method. Both methods overestimate model emissions inventory, but the AFT method overestimates less due to the explained error arising from kriging interpolation.

4.3 Mass Balance Technique and Temporal Evolution of The System

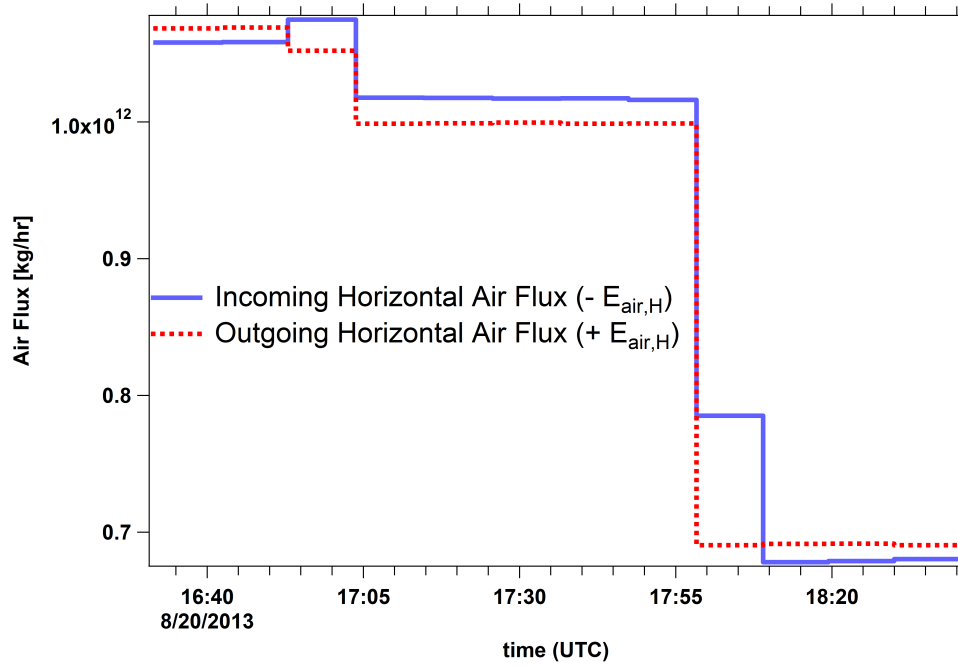
To evaluate the performance of the mass balance approach (divergence theorem) that is applied by TERRA (section 1.2.1), we will be relying on VP generated screens. Starting by looking at Figures 3.21, 3.22, 3.23 and 3.24 the temporal change in estimated emission rates can be observed. In fact in three of the four studied cases, emission rates decrease with time (flight 18 SO₂ emission rates increase over time, Figure 3.23). This could be a result of temporal evolution of the system and more specifically the change in advective fluxes. The GEM-MACH model emissions by sources within the studied facilities (CNRL and Syncrude) were constant. Figures 4.6 and 4.7 show the temporal change in horizontal and vertical advective air fluxes for flights 8 and 18, respectively. Looking at Figure 4.6a, it can be seen that both the incoming and outgoing horizontal fluxes through the box lateral sides are decreasing over time during flight 8. For this flight, the SO₂ plume is on the east wall with near zero levels everywhere else (Figure 3.13). Air is also leaving the box (positive $E_{air,H}$) through the east wall (Figure 3.11). SO₂ flux

depends on the air flux and the SO_2 concentrations on the screen. Figure 4.8 shows the temporal change in average SO_2 concentrations on the screen. The outgoing horizontal advective air flux ($E_{air,H}$) is also plotted, both SO_2 concentrations on the screen and $E_{air,H}$ decrease over time. Consequently, estimated SO_2 emissions (based on calculated advective fluxes) follow a similar decreasing trend (Figure 3.21).

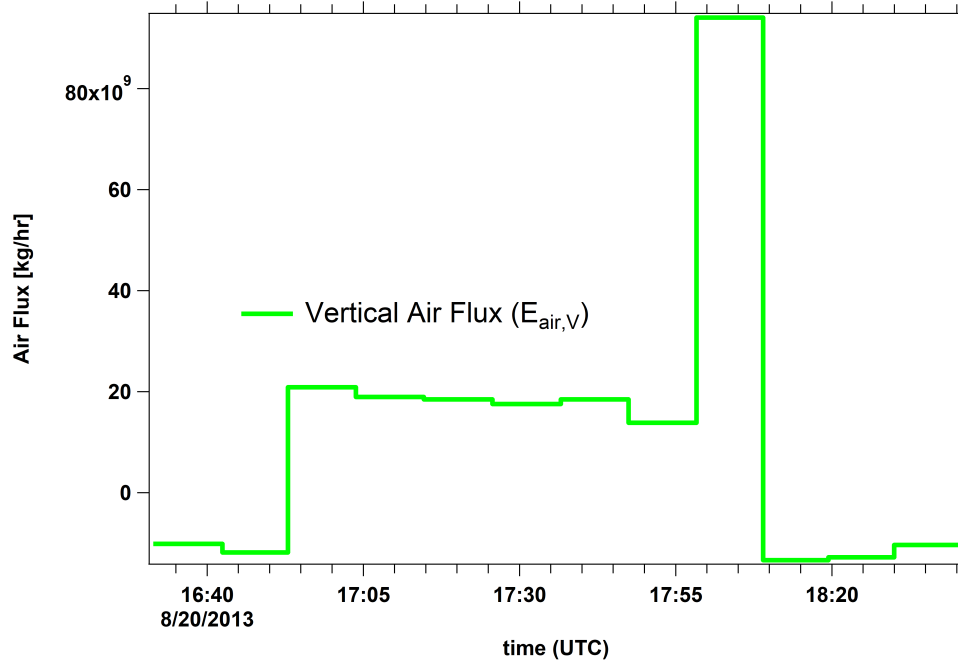
CO emissions are also decreasing over time (Figure 3.22) with the exception of a sudden increase in emission rates during the 9th 10 minute segment of flight 8. This can be attributed to a similar increase in the vertical air flux ($E_{air,V}$) during the same segment of the flight time (Figure 4.6b). The reason for this is that due to high levels of CO mixing ratios near the top of the box, the total estimated CO emissions rate is very sensitive to vertical advective CO flux (Table 3.8).

Similar observations can be made for flight 18. Estimated horizontal advective fluxes increase and the incoming (negative) vertical flux decreases (in magnitude) over time (Figure 4.7). Following the increase in horizontal advective air flux (Figure 4.7a), estimated SO_2 emission rates increase as well. Figure 3.24 shows a temporal decrease in CO estimated emissions during flight 18. During this flight, the net horizontal advective flux remained positive while decreasing over time. This positive net horizontal flux was balanced by a negative (incoming) decreasing (in magnitude) vertical flux through the box top (Figure 4.7b). Hence, the decrease in the net outgoing (positive) air flux resulted in a temporal decrease in estimated CO emission rates for flight 18 (Figure 3.24).

Air flux is proportional to the wind speed. Equation 1.6 shows the dependence of the advective flux on wind speed and species (e.g. SO_2) concentration. For the flux to remain constant, for a decrease in concentration on the screen the wind speed must increase and vice versa; which was not true for the studied cases except for flight 18 SO_2 emissions. Even for this case, the inverse proportionality of advective air flux and the total SO_2 con-

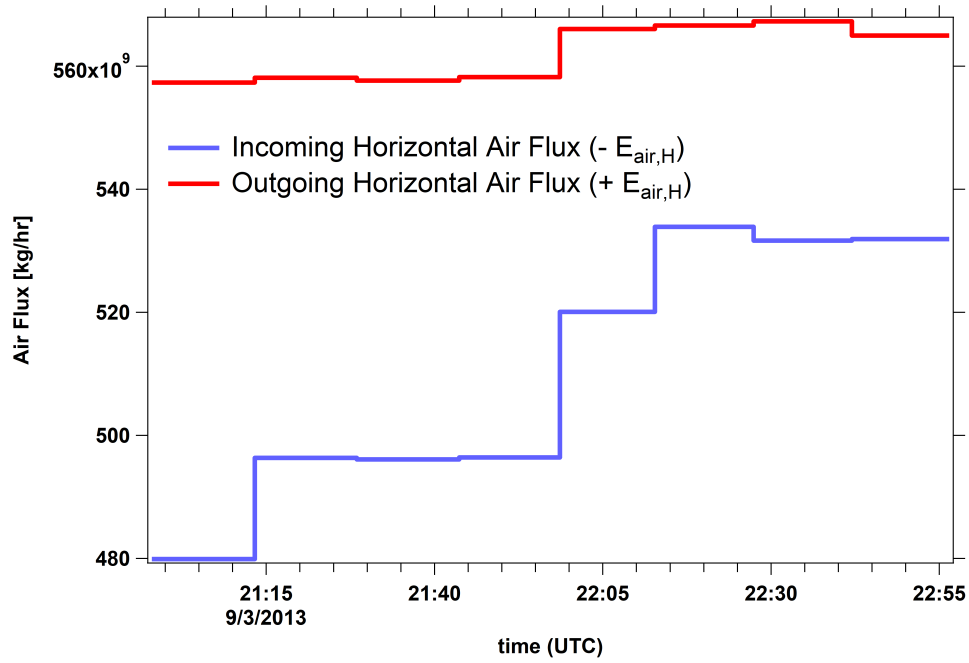


(a) Horizontal advective flux, $E_{air,H}$

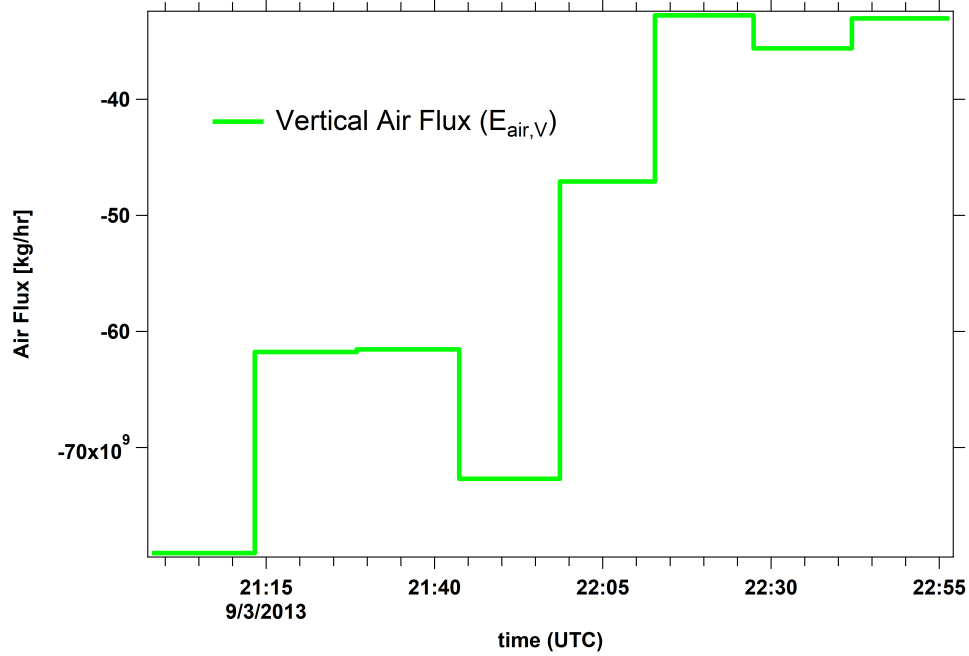


(b) Vertical advective flux, $E_{air,v}$

Figure 4.6: Advective air fluxes estimated based on VP extracted model data during flight 8. (a) Horizontal air flux ($E_{air,H}$) entering (red) and leaving (blue) through the lateral sides of the box. Horizontal fluxes decrease over time. (b) Vertical air flux ($E_{air,v}$) leaving through the top of the box. Air is horizontally entering the box through the lateral walls and vertically leaving through the top (Convergence).



(a) Horizontal advective flux, $E_{air,H}$



(b) Vertical advective flux, $E_{air,v}$

Figure 4.7: Advective air fluxes estimated based on VP extracted model data during flight 18. (a) Horizontal air flux ($E_{air,H}$) entering (red) and leaving (blue) through the lateral sides of the box. Horizontal fluxes increase over time. (b) Vertical air flux ($E_{air,v}$) entering (negative) through the top of the box. Air is entering the box vertically through the top and leaving horizontally through the lateral walls (divergence).

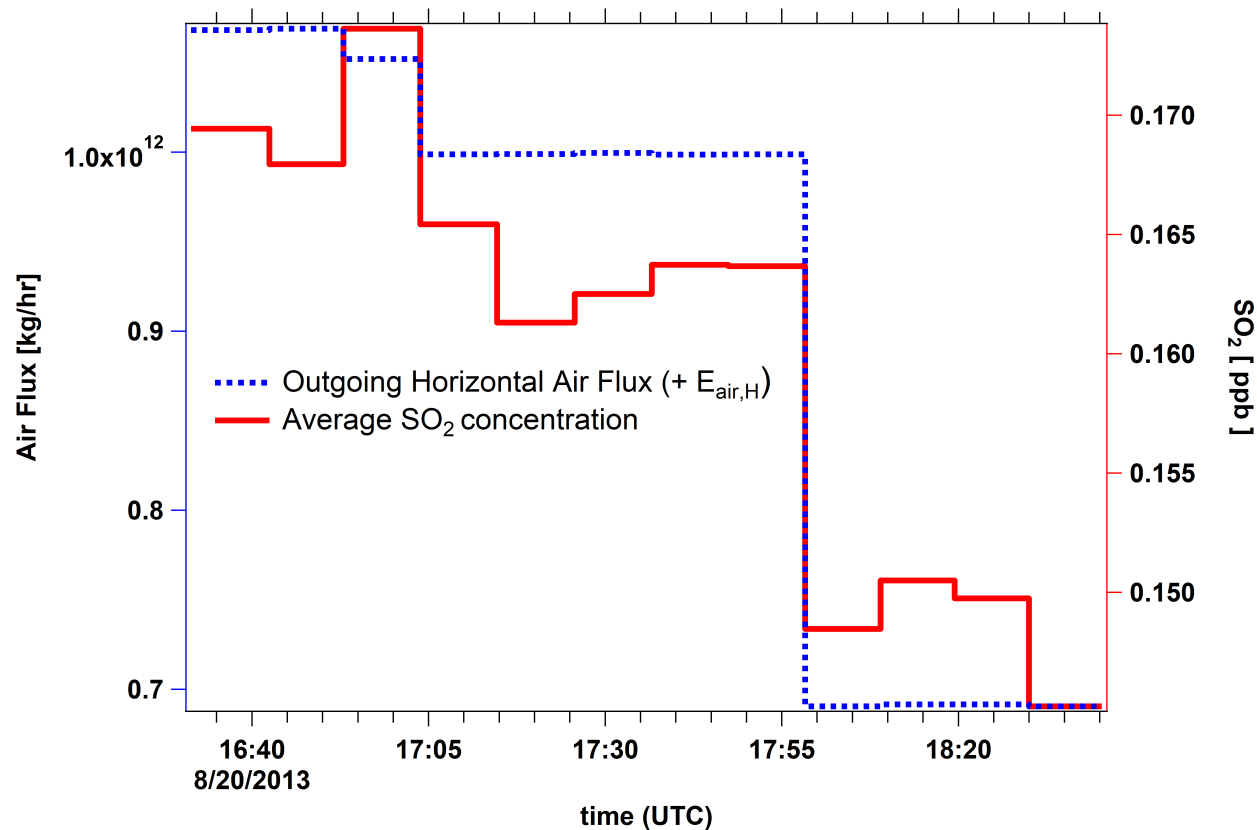


Figure 4.8: Temporal change in average SO₂ concentrations on the screen during flight 8. The outgoing horizontal advective air flux ($E_{air,H}$) is also plotted. Both the concentration and the air flux decrease over time. Consequently, estimated SO₂ emissions also decrease over time.

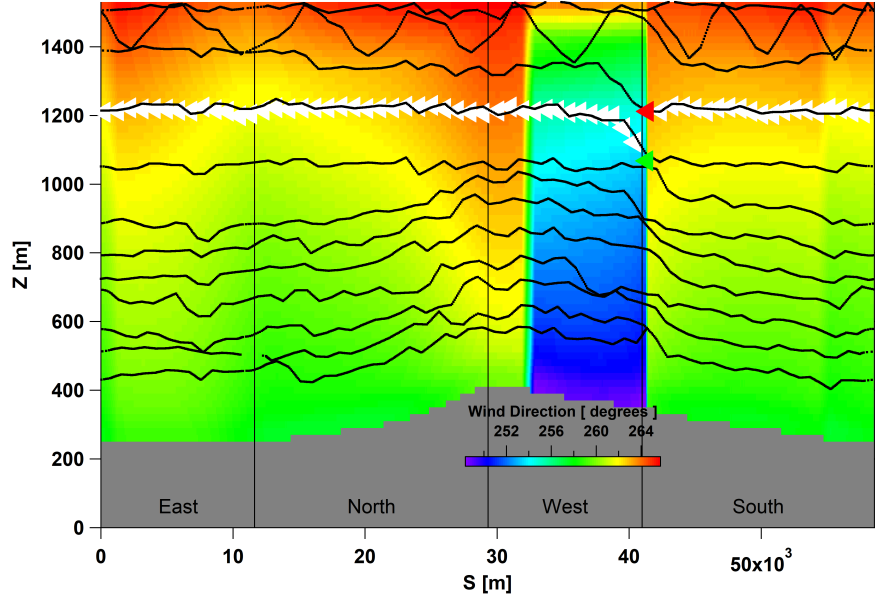
centration on the screen was not enough to result in a constant advective SO_2 flux. The contribution of all the other processes other than advective fluxes in describing the emissions originated within a control volume (box), are too small (less than 5% of the total E_C in Equation 2.6) to compensate for the non constant advective flux and result in a constant estimated total emissions rate. The dominance of advective fluxes in determining the total emissions has been shown in this work and has also been demonstrated in previous studies [12] [16] [22]. Hence, all the estimated emissions show temporal change.

Another observation that can be made by looking at CO estimated emissions for flight 8 (Figure 3.22) is the sudden increase in emission rates during the 9th 10 min segment of the flight. As mentioned before, this is a result of a sudden increase in vertical air flux during the same period of time (Figure 4.6b). Figure 4.9 reveals the reason for this sudden change in estimated values. Figure 4.9a shows a wind direction screen constructed using VP extracted model data during the 9th 10 minute segment of flight 8. The screen is distorted on the west wall. The flight track during this segment of the flight time is highlighted by white triangles that show the location and direction (to the left) of the virtual aircraft at each point. In addition, a green triangle marks the start point and a red triangle shows where the 9th flight level terminates. As the aircraft starts at the green triangle and extracts vertical profiles along the west wall, before it reaches the north wall the model iterates into a new time step. This discontinuity can also be seen by looking at wind direction values at a fixed height ($z = 600$ m) along the box walls (Figure 4.9b). The blue dashed line shows wind directions during the 8th 10 min segment and the green dashed line shows wind directions during the 10th 10 min segment of the flight. Both are continuous smooth horizontal profiles. The red line shows the horizontal profile extracted between minutes 80 and 90 of the flight time. Data collection starts while the model is still at the previous state (during the 8th 10 min) and continues while the model gets updated

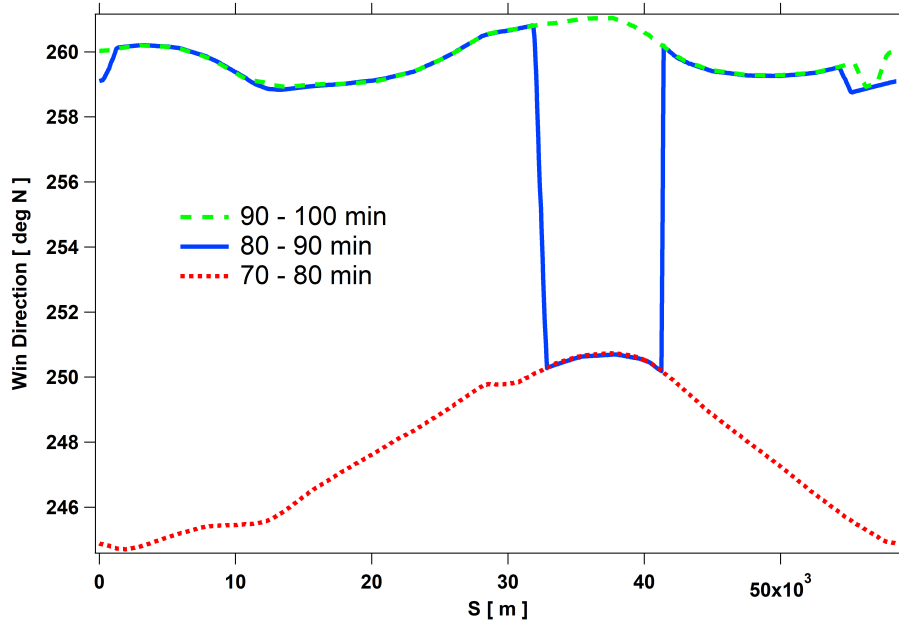
into the next state. The outcome is the distorted screen that can be seen in Figure 4.9a. This discontinuity results in an unbalanced estimated air flux, which in turn leads to the sudden increase in estimated CO emissions (Figure 3.22). SO₂ emission rate estimations are less affected by the discontinuity on the west wall, since the SO₂ plume is primarily located on the east wall with near zero concentrations on the west wall (Figure 3.13). Nevertheless, the estimations using distorted screens are not accurate since the fluxes are not balanced and the divergence theorem is not applicable. There is another such discontinuity in the wind screen during the 5th 15 min segment of flight 18. Estimations for these periods must be excluded. This improves estimated CO emissions by 4% for flight 8, relative to model emissions inventory. The other cases are not affected (negligible difference in estimated emissions) by this correction.

The above discussion suggests that the observed variations in estimated emission rates result directly from the temporal (both meteorological and species concentration levels) evolution of the system. In fact, it appears that estimations are affected by diurnal cycles when considering the times of the day each flight was conducted. The box pattern segment of flight 8 was flown between 16:31 - 18:40 UTC (10:31 - 12:40 local time) on August 20. The box pattern segment of flight 18 was between 20:58 - 22:56 UTC (14:58 - 16:56 local time) on September 3. The effect of diurnal cycles needs to be further investigated by studying the convection during flight times.

Assuming the observed advective trends persisted (following the temporal trends in estimated air fluxes $E_{air,H}$ and $E_{air,V}$) over periods longer than the flight times, estimations can be projected forward or backward in time. Figure 4.10 shows estimated emission rates of flight 8, projected linearly forward in time. As can be seen from Figure 4.10, estimations during the flight time (blue line) are higher than the known model emissions inventories (green dashed line) but moving in the right direction over time, for both SO₂ and CO. The red dashed line is a linear fit to estimated emission rates (blue

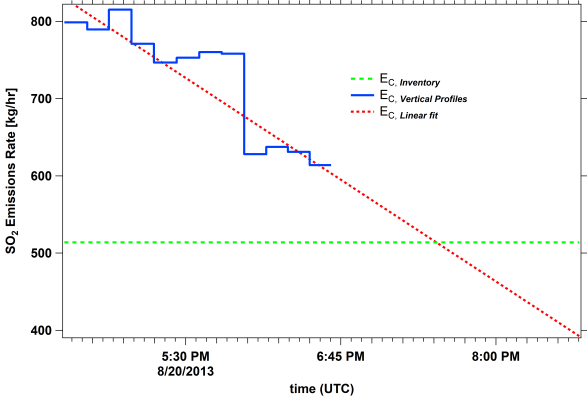


(a) Wind direction screen

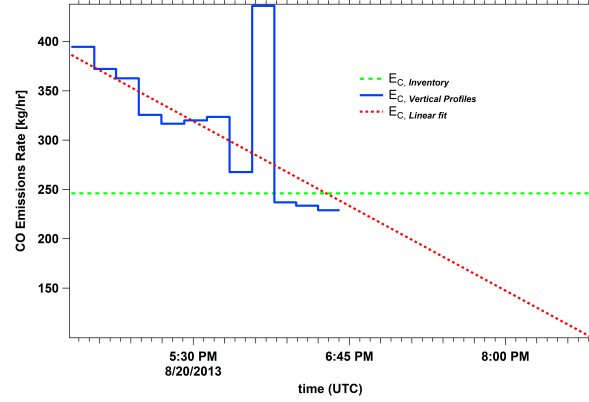


(b) Wind direction horizontal profile

Figure 4.9: Wind direction screen, generated using the VP extracted model data during the 9th 10 min segment of flight 8. (a) The screen is distorted, since the model was updated into a new state while the data was being collected for screen generation. (b) Horizontal profiles of wind direction along the box walls at $z = 600$ m are shown for the 8th, 9th and 10th 10 min segments of the flight. The profile during the 9th 10 min segment is partially in the previous state (during the 8th 10 min) and partially in the next state (during the 10th 10 min). This resulted in a distorted wind direction screen and unbalanced air flux estimations.



(a) Flight 8 SO₂ emissions



(b) Flight 8 CO emissions

Figure 4.10: Flight 8 estimated emissions (blue) follow a decreasing trend. Linear fits (red) of the estimated emissions, projected forward for the next two hours after the flight time reach the model emissions inventory (green) and continue decreasing.

line) projected forward in time for another 2 hrs. This projection approaches the emissions inventory ($E_{C,Inventory}$) approximately one hour after the flight ends for SO₂ emissions (Figure 4.10a), and towards the end of box flight time for CO emissions (Figure 4.10b). The projection continues to fall below the inventory values, this results in a mean value close to inventory emission levels. Similar observation can be made for flight 18 CO emissions (Figure 3.24), Flight 18 SO₂ emissions increase and deviate more from inventory values over time (Figure 3.23). These observations suggest that extending the flight times can potentially improve the estimations. Table 4.2 lists percentage improvements (relative to model emissions inventory) in mean estimated emissions for each extra hour of flight time, for flights 8 (SO₂ and CO) and 18 (CO). Flight 18 SO₂ estimates are not improved by extending the flight time. Mean CO emissions approach the inventory emission values for less than two additional hours (extended flight time) for both flights. In fact, flight 18 mean CO emissions (averaged over flight time + 1 hr) reach model emissions inventory level for only one hour additional flight time (72% improvement). Flight 8 SO₂ emission estimations also show substantial improvements for each extended hour, about 11% for each extra hour of flight time.

Furthermore, for these three cases (flight 8 SO₂ and CO and flight 18 CO

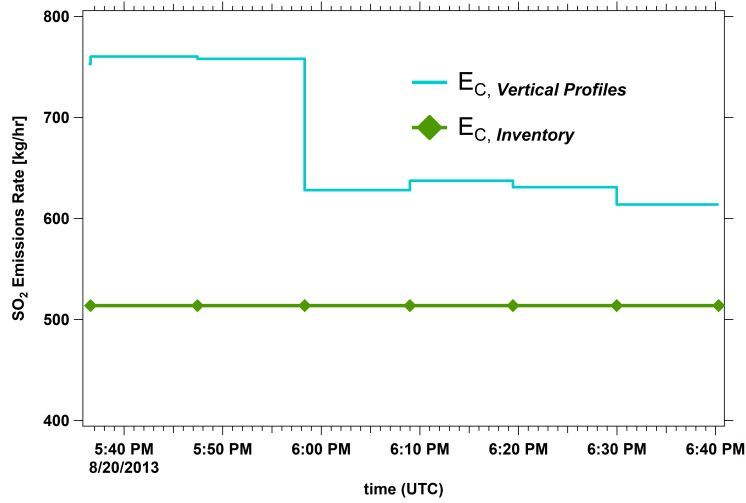
Table 4.2: Potential improvements in mean estimated emissions for each extra hour of flight time. Percentage improvements relative to model emissions inventory for flight 8 SO₂ and CO and flight 18 CO emissions are shown. For flight 18 SO₂ the result is negative, meaning that the estimates continue to deviate from the model emissions inventory and therefore no improvements are made by extending the flight time for this case.

	1 hr	2 hr	3hr
Flight 8 SO ₂	11%	22%	33%
Flight 8 CO	15%	28%	
Flight 18 SO ₂	-5%		
Flight 18 CO	72%		

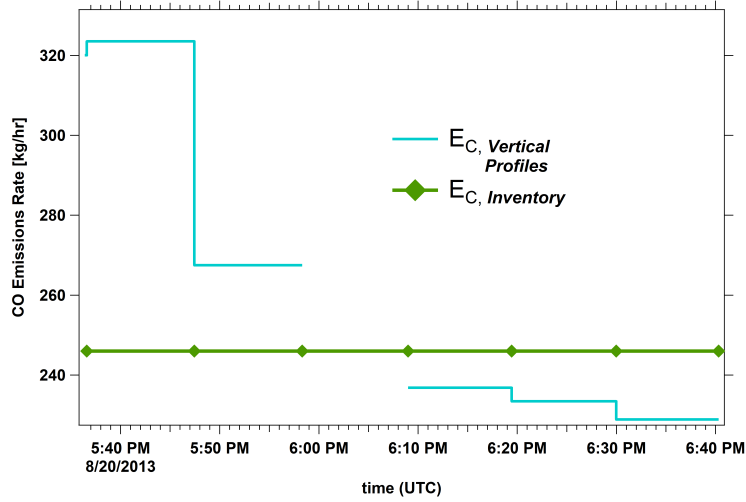
emissions) the estimated emissions for the second half of both flights 8 and 18 (the second hour of a 2 hr flight) are more consistent with model emissions inventories, especially for CO emissions. Figure 4.11 shows SO₂ and CO estimated emissions for the second half of flights 8 and 18. Note that in Figure 4.11b the peak resulting from discontinuity in wind direction is removed (see Figure 4.9 for the discussion). The mean estimated emissions (three cases out of four) for the second hour of the flight times are in better agreement with model emissions inventory (green line and markers) than those for the first hour. The average emissions for this period and their comparison to model emissions inventory are shown in Table 4.3. Their deviation from the model emissions inventory is at most 26% and in one case as low as 3% (Flight 8 CO emissions), which is a great improvement compared to the results presented in Tables 3.11 and 3.12.

Table 4.3: Mean estimated emissions for the second hour of flights 8 and 18 are compared to model emissions inventory. Percentage differences show the estimated emissions during the second half of the flights agree better with inventory values. Flight 18 SO₂ emissions for this period deviate more from model emissions and are not shown here.

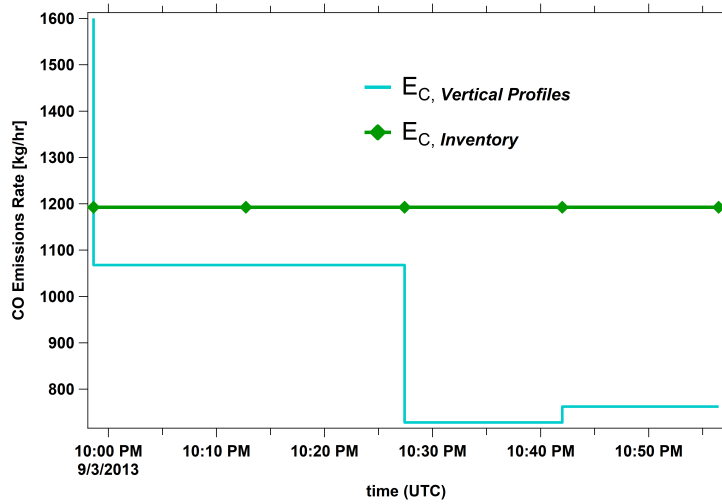
	Flight 8 SO ₂	Flight 8 CO	Flight 18 CO
Emissions Inventory [kg/hr]	513.7	246.0	1192.4
2nd hr Estimations [kg/hr]	647.0	253.1	877.6
Percentage Difference	26%	3%	26%



(a) Flight 8 E_{SO_2}



(b) Flight 8 E_{CO}



(c) Flight 18 E_{CO}

Figure 4.11: Estimated emissions for the second half (first hour of flight not shown here) of flights 8 and 18 are compared to model emissions inventory (a) flight 8 SO_2 emissions (b) flight 8 CO emissions (estimation for the 9th 10 min segment is removed) and (c) flight 18 CO emissions. Estimated emissions during the second hour of the 2 hr flights agree better with inventory values. This was not true for flight 18 SO_2 emissions, which are not shown here.

4.4 Shift In Plume Location Relative to Aircraft's Motion

During the flight time on 20 August 2013, as the model evolved over time, the location of the plume on the east wall shifted towards south as it was elevating. Figure 4.12 shows the SO₂ plume on the east wall during the first 10 min segment of flight 8. The perimeter of the plume is highlighted with a white contour labeled 1st (for 1st 10 min) and also location and direction (to the left) of the aircraft is shown with white triangles, along the flight tracks during this time. Perimeters and flight levels for the 5th (yellow) and the 10th (green) 10 min segments of the flight are also superimposed on the screen. Looking at the consecutive contours (plume perimeters), it can be seen that the plume is rising and shifting to the left (south) over time. The aircraft was also flying towards south (triangles pointing to the left) and moving to the higher levels, while extracting data along flight tracks. This resulted in over-sampling of the same plume and therefore the appearance of a second plume while using the AFT extracted data for generating SO₂ mixing ratio screen (Figure 3.7). In AFT method analysis, the aircraft-based measurements are treated as temporal mean distributions of relevant data (e.g. SO₂ mixing ratio) over the period of the box flight time. This makes AFT screens comparable to the temporal average of VP screens which correspond to 10-15 min segments of the box flight time. Figure 4.13 compares the SO₂ AFT krigged screen (Constant method extrapolation) to the mean VP screen for flight 8. In addition to higher levels of SO₂ on the AFT krigged screen compared to the mean VP screen (note the difference in the two color scales), a secondary plume can also be seen on the krigged screen. According to Table 4.1, the overestimation of average SO₂ concentrations by the AFT krigged-Constant screen relative to the mean VP screen is about 21% for flight 8. For the other cases this relative overestimation is at most 5.4%. No substantial plume shift was observed for the other cases. Therefore, it can be deduced that potentially between 16 to 21% of overestimation in SO₂

concentrations can be attributed to the observed shift in SO₂ plume location during flight 8. This effect contributes to overestimation of emission rates and can be responsible (at least partially) for estimated emission rates being higher than model emissions inventory (Tables 3.11). This idea was tested by increasing the SO₂ concentration levels in VP method estimations and observing the resulting changes in the total estimated emissions for flight 8. Results are summarized in Table 4.4, the changes are essentially one to one (↑ 20% concentration ⇒ ↑ 20% estimated emission). Therefore, the 19% difference between AFT-Constant and average VP estimations shown in Table 3.11 can be the direct result of 19% overestimation in SO₂ concentrations by AFT method. The complete opposite is also possible, with the aircraft flying in the same direction but with the plume falling and shifting to the right. In which case an underestimation will result.

Table 4.4: Dependence of estimated emission rates on overestimation in SO₂ concentrations for flight 8 VP method estimations, was examined. Results show that the changes are one to one, N % increase in total SO₂ concentration results in almost N % increase in estimated emission rates.

Increase in SO ₂ concentrations	10.0%	20.0%	30.0%
Change in total estimated emissions	9.9%	19.8%	29.8%

Gordon et al., in their analysis of the aircraft-based measurements during the 2013 field campaign also observed multiple plumes (separated plume maxima) on SO₂ mixing ratio screens for different flights (including flight 8) [12]. They suggested that shifts in wind direction and speed and also changes in temperature can result in a shift in plume position and therefore under/oversampling of the same plume. Changes in temperature can change plume buoyancy and result in plume vertical movement, and shifts in mean wind direction and speed can result in plume lateral movement. Figure 4.14 shows temporal evolution of temperature, wind speed and direction at $s = 5680$ m and $z = 500$ m (on initial plume centerline) during flight 8. Temperature increases by 1.5 degrees over the 2 hr and 10 min flight time

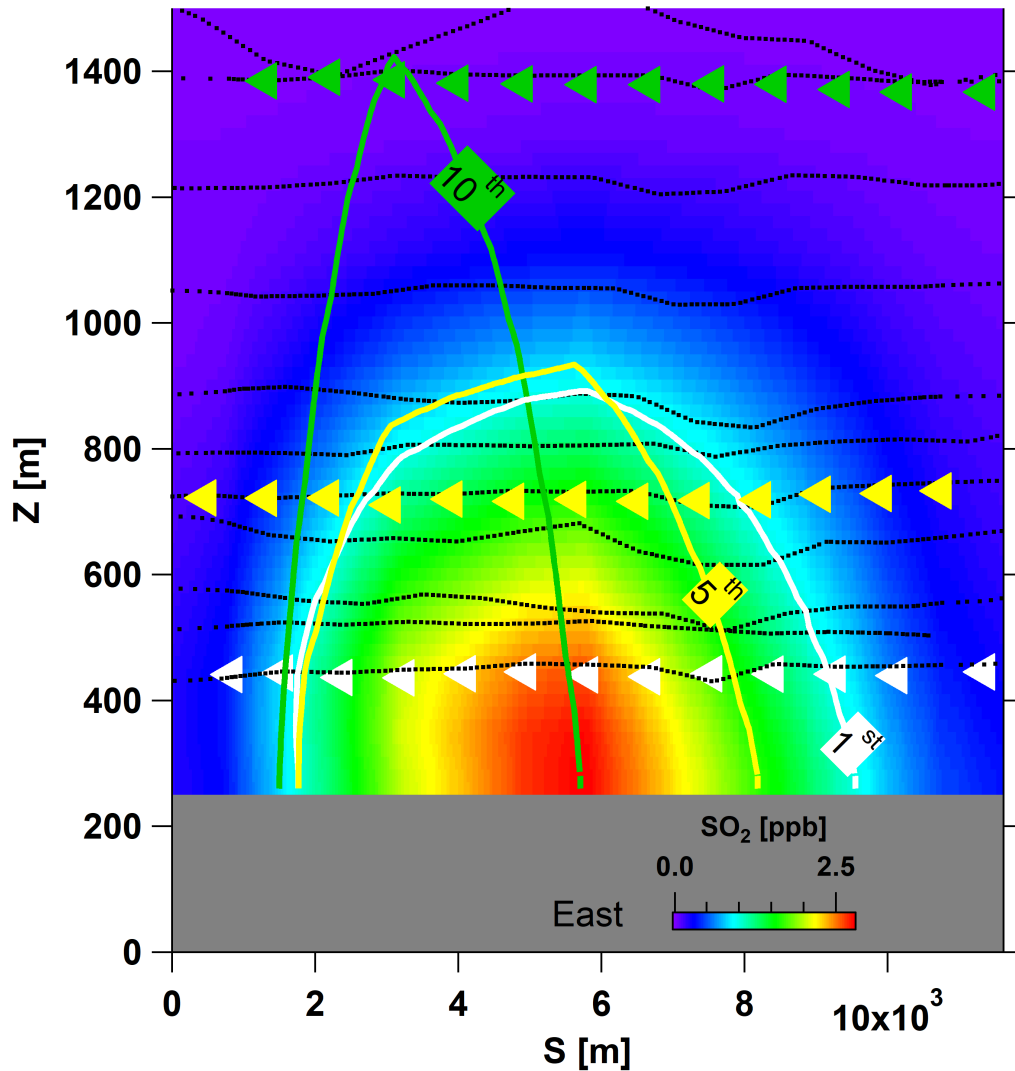
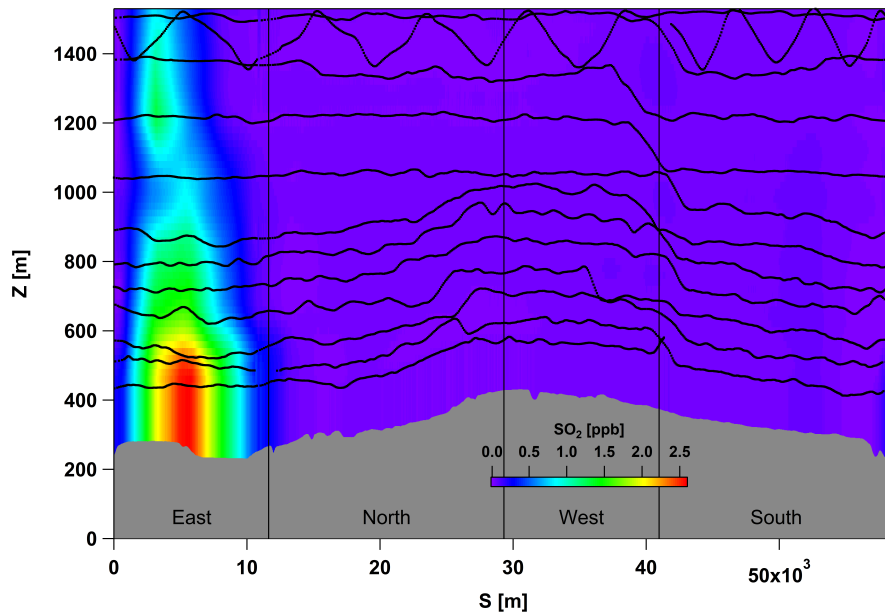
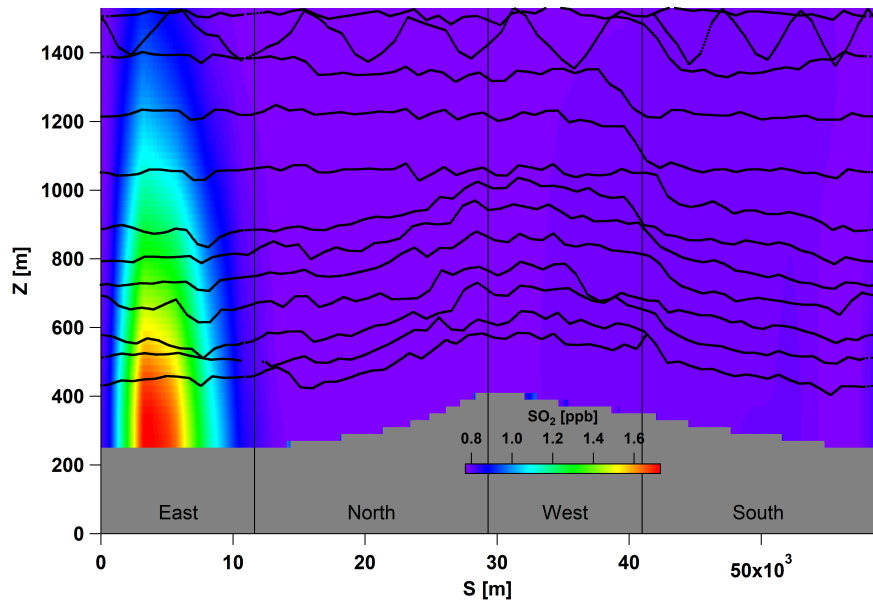


Figure 4.12: The SO_2 screen (east wall only) for flight 8 is shown. SO_2 plume and its perimeter (white contour) during the first 10 min segment of the flight is shown and labeled 1st. Also, the location of the aircraft and the direction of the flight (to the left) during this time is shown with white triangles. The same is shown for the 5th (yellow) and the 10th (green) 10 min segments of flight time. By looking at the consecutive contours (plume perimeters), it can be seen that the SO_2 on the east wall is shifting to the left (south) as it is rising in altitude over time.



(a) SO₂ AFT krigged screen, extrapolated using Constant method



(b) SO₂ Mean VP screen

Figure 4.13: Flight 8 SO₂ mixing ratio AFT krigged screen (a) compared to the mean VP screen (b) for the same flight. Shift in plume location over time results in oversampling and the appearance of a secondary plume on the AFT krigged screen. Note the difference in color scales.

and the wind speed decreases. Shift in wind direction from SW to W can result in a lateral shift in plume position towards south, which agrees with the observed plume shift (Figure 4.12). Further, as can be seen from Figure 4.14 changes in wind speed and direction and temperature over time are not gradual and three major step changes can be observed. These step changes (which correspond to model step changes) lead to discontinuities in generated VP screens and also result in greater uncertainties in AFT estimations. The most substantial step change happens around the 9th 10 min of the box flight time, which as it was discussed before (see Figure 4.9 for the discussion) results in unbalanced advective air fluxes. Also the dependence of the horizontal advective air flux on wind speed can be seen from Figure 4.14. The air flux ($E_{air,H}$) plotted on Figure 4.8 follows a similar trend to that of the wind speed. As was discussed in the previous section, this results in a major step change in estimated emissions and the observed disagreement between the estimates during the first and second hours of the box flight time (Figures 3.21 and 3.22).

In addition to direction, the relative speed of the plume's motion to that of the aircraft can be a factor in over/underestimation. Different possible combinations of relative speed and direction can cause various effects. Mölders et al. [20], in their studies with virtual UAV sampling of air quality related data, showed that sampled distributions were very sensitive to UAV speed and flight patterns. During one of their studied model episodes, sudden changes in wind fields and temperature were observed. They described this observation as a frontal passage. Their results during this frontal passage showed large differences in sampled distributions for different flight patterns and speeds [20]. Airborne measurements during inconsistent wind conditions can increase the uncertainties in estimations and must be avoided. During the 2013 field campaign, GEM-MACH created forecasts were used for directing the airborne measurements [18]. And as Mölders et al., suggest, virtual sampling using the model forecasts can also be employed for planning flight

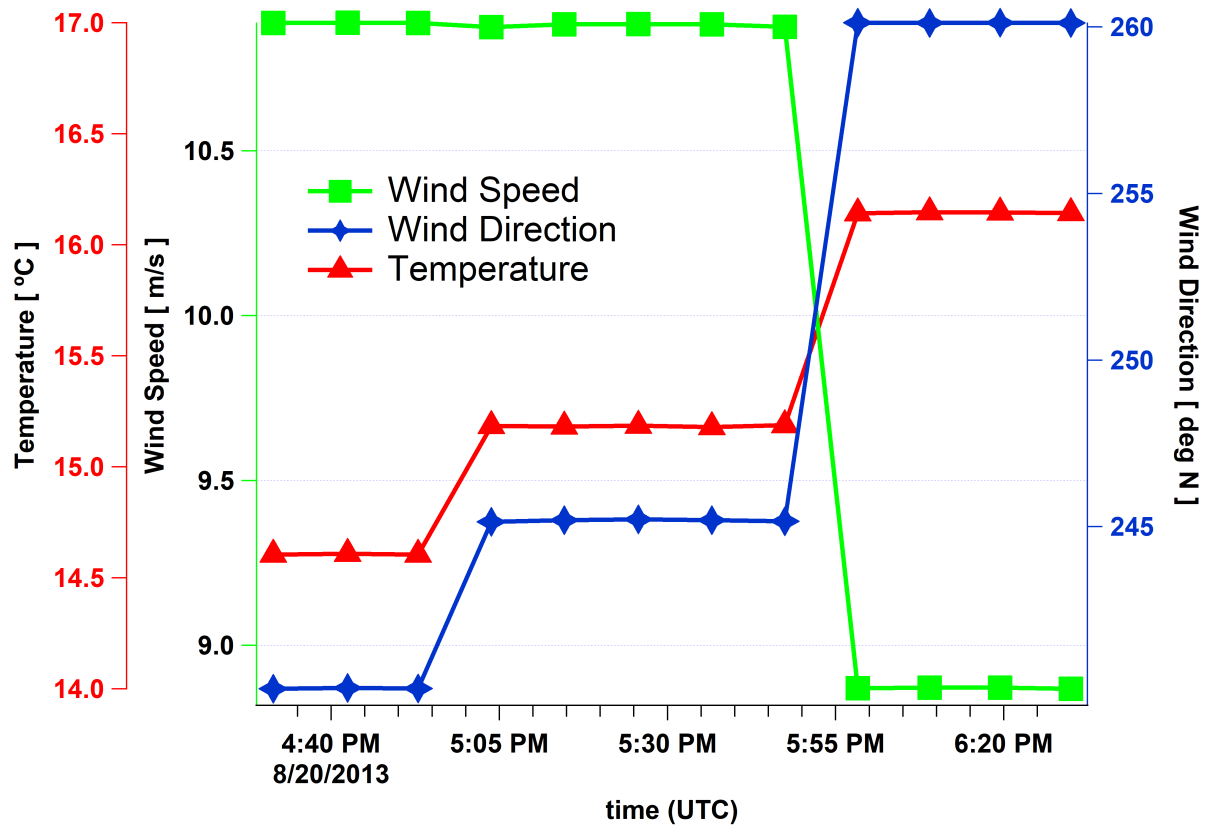


Figure 4.14: Temporal evolution of temperature, wind speed and direction at $s = 5680$ m and $z = 500$ m during flight 8. Temperature increases, wind speed decreases and the wind direction shifts from SW to W.

designs [20].

4.5 VP Method Overestimations

As can be seen from Tables 3.11 and 3.12, average (over flight time) VP estimated emissions are 26% to 41% for flight 8 and 71% to 78% for flight 18 higher than model emissions inventory. For three out of four studied cases (flight 8 SO₄ and CO and flight 18 CO emissions) estimated emissions were initially 1.5 to 2.8 times higher than inventory values and decreased over time (during the box flight) and approached the inventory emission levels. However, flight 18 SO₂ emissions remained 1.7 to 1.9 times higher than model emissions inventory. Three possible sources of error can be addressed for VP method overestimations:

1. Temporal evolution of the system during the 10-15 min segments of box flight time corresponding to each VP screen. This is similar to observed overestimations in AFT method estimates due to temporal changes such as plume movement and oversampling which resulted in up to 21% overestimations relative to VP estimates. Further, temporal variations in wind speed and direction can result in unbalanced advective fluxes and introduce uncertainties in applying the mass balance technique.
2. Interpolating model extracted values (with the temporal and spacial resolutions of 2 min and 2.5 km respectively) in space to match the reported frequency of aircraft-based measurements of 1 Hz, and further projecting and interpolating the extracted data on a grid of 40m × 20m ($\Delta s \times \Delta z$). This can introduce uncertainties in emissions estimates.
3. Model mass conservation can be responsible for higher estimated emissions. Specially for the case of flight 18 SO₂ emissions where there is a relatively large gap between the estimates and model emissions inventory that persists over the box flight time.

Chapter 5

Conclusions

During an actual aircraft-based emissions rate retrieval campaign, data collection is made in AFT approach. Corrections such as SGI can be made to improve screens generated by kriging interpolation. The *Constant* extrapolation method (section 1.2.2), showed the best performance for filling the gap below the lowest flight level for all the studied cases by performing 5-20% better than other extrapolation methods. TERRA assumptions for air density estimations based on meteorological measurements (e.g. temperature, pressure) and also assumptions for surface deposition rate estimations were very close to model values and resulted in less than 3% deviation in estimated emission rates based on model extracted air density and deposition values.

The AFT method samples concentration and meteorological data and treats them as spatial distribution of data points around the area source (box) and ignores the temporal evolution of the system during the box flight time of approximately 2 hours. The VP method does the same for flight time at each circuit around the box (periods of 10-15 min). All the estimated emission rates seem affected by the diurnal cycles, and ignoring the temporal changes in the system during the 2 hours (10-15 min for VP method) time of the flight would be misleading. In fact, the general overestimation of emission rates for all the cases (independent of the method) and non constant estimated emissions (VP method) can be attributed (at least partially) to the temporal development of the system. The VP estimated emissions (cal-

culated based on SO₂ and CO advective fluxes) for all of the studied cases demonstrated temporal variations, following the trends observed in advective air fluxes. Therefore, according to our results, it could be deduced that model emissions have not been constant for time steps subdividing the studied periods of approximately 2 hours of model simulations. The fact that estimated emissions approached model emissions inventory over time (for three out of four cases) supports this statement. For the one case that this explanation does not apply, namely flight 18 SO₂ emissions, the temporal variation was smaller compared to other cases. However, the discrepancy between the estimated emissions and the model emission inventory for this case remained larger than 50%. To correct for this the following approaches are suggested: 1) studying the convection and changes in advective fluxes during the flight time, and normalizing the estimated emissions by factors related to advective air fluxes. 2) extending the sampling time (in both directions to before and after current box flight times) to periods 1.5 to 2 times longer than the current flight times (2 hrs) to obtain better statistical averages. Results for theoretically extending the flight times showed that flying an additional hour (beyond current box flight times) can potentially improve the estimations by 11%, 15% and 72% for three of the studied cases (Table 4.2). This was not true for one of the four studied cases (flight 18 SO₂ estimates) where the projection of emissions forward in time continued to deviate from model inventory values (-5%) and resulted in no improvements in estimations. While flying an aircraft for longer periods might not be logistically feasible, unmanned air vehicles (UAVs) can be flown for up to 20 hr and they are much cheaper to purchase and deploy. In fact employing UAVs by environmental and atmospheric scientists have been gaining more popularity in the recent years [9] [20]. The downside of using UAVs would be the fact that they can carry less load (only small instruments) compared to manned commercial size aircrafts.

Further, estimated emission rates show dependence on flight designs. The

relative motion of a shifting plume to the sampling aircraft could result in under or over estimations. This can be corrected in the following ways: 1) conducting extensive studies of wind vectors and advective fluxes during the flight time and performing forecasts of the motion of the plume and correcting for it afterwards while analyzing the data. 2) updating and optimizing flight patterns in accordance with plume movements on the fly in order to minimize the effects of the plume relative motion.

Non-constant estimated emissions are in contrast with our knowledge of model emissions, which were set to be constant. To account for the effect of temporal evolution of the system in emission rate estimations, model values over the entire area of the screen (along the box walls) must be extracted for each model time step (2 min) so there would be no temporal lag between different regions of the screen. The spatial distribution of the relevant data for each model time step can be used for determining the temporal mean distributions for the box flight time and mass balance calculations can be performed using these mean values. Also, screens for each time step can be analyzed with the mass balance technique to estimate emissions for every 2 min model time and then the average of these estimations (over 2 hrs) can be calculated and compared to model emissions inventory and to the AFT estimations that resemble aircraft-based emissions rate retrieval.

To address the higher than model emissions inventory estimations, model mass conservation during the studied cases must be examined. To achieve this, model mass budget can be determined by performing volume integrations of species (e.g. SO_2 and CO) concentrations over the entire volume of the box (control volume) for every model time step. Results of these calculations can be compared directly to model inventory values to check for mass conservation. Also, chemical transport into and out of the box can be tracked by employing this approach.

Another possible source of error is model data interpolations. Model extracted values were separated by 2.5 km horizontally and were extracted for

every model time step of 2 min. These values were interpolated in time and space to match the 1 Hz frequency of aircraft-based measurements and were finally projected and interpolated on a grid of 40 m \times 20 m resolution. This can be responsible for overestimations in model data distributions. The uncertainties arising from these interpolations must be quantified and accounted for.

Bibliography

- [1] *WRF/Chem Version 3.3 User's Guide*. 96 p. 2011.
- [2] G. Adrian and F. Fiedler. Simulation of unstationary wind and temperature fields over complex terrain and comparison with observations. *Contribution to Atmospheric Physics*, 1991.
- [3] S Alfieri, U Amato, MF Carfora, M Esposito, and V Magliulo. Quantifying trace gas emissions from composite landscapes: a mass-budget approach with aircraft measurements. *Atmospheric Environment*, 44(15):1866–1876, 2010.
- [4] Nester K. Baer, M. Parameterization of trace gas dry deposition velocities for a regional messoscale diffusion model. *Annales Geophysicae*, 1992.
- [5] M. O. L. Cambaliza, P. B. Shepson, D. R. Caulton, B. Stirn, D. Samarov, K. R. Gurney, J. Turnbull, K. J. Davis, A. Possolo, A. Karion, C. Sweeney, B. Moser, A. Hendricks, T. Lauvaux, K. Mays, J. Whetstone, J. Huang, I. Razlivanov, N. L. Miles, and S. J. Richardson. Assessment of uncertainties of an aircraft-based mass balance approach for quantifying urban greenhouse gas emissions. *Atmospheric Chemistry and Physics*, 14(17):9029–9050, 2014.
- [6] CUMULATIVE ENVIRONMENTAL MANAGEMENT ASSOCIATION (CEMA). <https://www.cemaonline.ca>, emission inventory files.
- [7] Jean Ct, Sylvie Gravel, Andr Mthot, Alain Patoine, Michel Roch, and Andrew Staniforth. The operational cmcmrb global environmental multiscale (gem) model. part i: Design considerations and formulation. *Monthly Weather Review*, 126(6):1373–1395, 1998.
- [8] ECCC David Anselmo. A new canadian air quality forecast model: Gem-mach15. In *12th Conference on Atmospheric Chemistry*, 2010.
- [9] Jack Elston, Brian Argrow, Maciej Stachura, Doug Weibel, Dale Lawrence, and David Pope. Overview of small fixed-wing unmanned aircraft for meteorological sampling. *Journal of Atmospheric and Oceanic Technology*, 32(1):97–115, 2015.
- [10] Environment and Climate Change Canada (ECCC). http://climate.weather.gc.ca/historical_data/, historical weather data.
- [11] JR Garratt. The atmospheric boundary layer, cambridge atmospheric and space science series, 1, edited by, 1994.
- [12] M. Gordon, S.-M. Li, R. Staebler, A. Darlington, K. Hayden, J. O'Brien, and M. Wolde. Determining air pollutant emission rates based on mass balance using airborne measurement data over the alberta oil sands operations. *Atmospheric Measurement Techniques*, 8(9):3745–3765, 2015.
- [13] Georg A. Grell, Steven E. Peckham, Rainer Schmitz, Stuart A. McKeen, Gregory Frost, William C. Skamarock, and Brian Eder. Fully coupled online chemistry within the wrf model. *Atmospheric Environment*, 39(37):6957 – 6975, 2005.
- [14] E. H. Isaaks and R. M. Srivastava. *Applied geostatistics*, pages 289–296. Oxford University Press, New York, 1989.

- [15] C. John. *Emissionen von Luftverunreinigungen aus dem Straßenverkehr in hoher räumlicher undzeitlicher Auflösung. Untersuchung von Emissionsszenarien am Beispiel Baden-Württembergs (in German)*. PhD thesis, University of Stuttgart, 1999. Research Report No. 58.
- [16] N. Kalthoff, U. Corsmeier, K. Schmidt, Ch. Kottmeier, F. Fiedler, M. Habram, and F. Slemr. Emissions of the city of augsburg determined using the mass balance method. *Atmospheric Environment*, 36, Supplement 1:19 – 31, 2002. Evaluation of Modeled Emission Inventories of Ozone Precursors. A Case Study for an Urban Area (Augsburg, Germany).
- [17] Anna Karion, Colm Sweeney, Gabrielle Ptron, Gregory Frost, R. Michael Hardesty, Jonathan Kofler, Ben R. Miller, Tim Newberger, Sonja Wolter, Robert Banta, Alan Brewer, Ed Dlugokencky, Patricia Lang, Stephen A. Montzka, Russell Schnell, Pieter Tans, Michael Trainer, Robert Zamora, and Stephen Conley. Methane emissions estimate from airborne measurements over a western united states natural gas field. *Geophysical Research Letters*, 40(16):4393–4397, 2013.
- [18] P. A. Makar, C. Stroud, J. Zhang, M. Moran, A. Akingunola, W. Gong, S. Gravel, B. Pabla, P. Cheung, Q. Zheng, G. Marson, S. M. Li, J. Brook, K. Hayden, J. Liggio, R. Staebler, and A. Darlington. *High Resolution Model Simulations of the Canadian Oil Sands with Comparisons to Field Study Observations*, pages 503–508. Springer International Publishing, Cham, 2016.
- [19] Kelly L Mays, Paul B Shepson, Brian H Stirm, Anna Karion, Colm Sweeney, and Kevin R Gurney. Aircraft-based measurements of the carbon footprint of indianapolis. *Environmental science & technology*, 43(20):7816–7823, 2009.
- [20] N. Mölders, M. Butwin, J. Madden, H. Tran, K. Sassen, and G. Kramm. Theoretical investigations on mapping mean distributions of particulate matter, inert, reactive, and secondary pollutants from wildfires by unmanned air vehicles (uavs). *Open Journal of Air Pollution*, 04(03):149–174, 2015.
- [21] Debasish PaiMazumder and Nicole Mölders. Theoretical assessment of uncertainty in regional averages due to network density and design. *Journal of Applied Meteorology and Climatology*, 48(8):1643–1666, 2009.
- [22] H.-J Panitz, K Nester, and F Fiedler. Mass budget simulation of nox and co for the evaluation of calculated emissions for the city of augsburg (germany). *Atmospheric Environment*, 36, Supplement 1:33 – 51, 2002. Evaluation of Modeled Emission Inventories of Ozone Precursors. A Case Study for an Urban Area (Augsburg, Germany).
- [23] J. Peischl, T. B. Ryerson, J. Brioude, K. C. Aikin, A. E. Andrews, E. Atlas, D. Blake, B. C. Daube, J. A. de Gouw, E. Dlugokencky, G. J. Frost, D. R. Gentner, J. B. Gilman, A. H. Goldstein, R. A. Harley, J. S. Holloway, J. Kofler, W. C. Kuster, P. M. Lang, P. C. Novelli, G. W. Santoni, M. Trainer, S. C. Wofsy, and D. D. Parrish. Quantifying sources of methane using light alkanes in the los angeles basin, california. *Journal of Geophysical Research: Atmospheres*, 118(10):4974–4990, 2013.
- [24] Roland Stull. *Meteorology for Scientists and Engineers*, page 8. 3rd edition.
- [25] D. Talbot, M. D. Moran, V. Bouchet, L. P. Crevier, S. Mnard, and A. Kallaur. Development of a new canadian operational air quality forecast model. *Air Pollution Modeling and Its Application XIX NATO Science for Peace and Security Series*, page 470478, 2008.
- [26] J. C. Turnbull, A. Karion, M. L. Fischer, I. Faloona, T. Guilderson, S. J. Lehman, B. R. Miller, J. B. Miller, S. Montzka, T. Sherwood, S. Saripalli, C. Sweeney, and P. P. Tans. Assessment of fossil fuel carbon dioxide and other anthropogenic trace gas emissions from airborne measurements over sacramento, california in spring 2009. *Atmospheric Chemistry and Physics*, 11(2):705–721, 2011.
- [27] L. Zhang, J. R. Brook, and R. Vet. A revised parameterization for gaseous dry deposition in air-quality models. *Atmospheric Chemistry and Physics*, 3(6):2067–2082, 2003.